

---

Unterschrift Betreuerin



TECHNISCHE  
UNIVERSITÄT  
WIEN  
Vienna University of Technology

## DIPLOMARBEIT

# Impact of beamline-specific particle energy spectra on clinical plans in Carbon ion beam therapy.

ausgeführt am Atominsitut  
der Technischen Universität Wien  
in Kooperation mit MedAustron

unter der Anleitung von  
**Ao.Univ.Prof.Dr. Christina Strel**  
**Ass.Prof. Dipl.-Ing. Dr.techn. Karin Poljanc**  
**Priv.-Doz. DI Markus Stock, PhD**  
**Antonio Carlino, PhD**

durch

**Niklas Lackner**

2752 Wöllersdorf, Anna Steuergasse 27

January 20, 2020

---

Unterschrift Student

MASTERTHESIS 2020

# Impact of beamline-specific particle energy spectra on clinical plans in Carbon ion beam therapy.

NIKLAS LACKNER



Atominstitut  
TECHNISCHE UNIVERSITÄT WIEN  
Wien, Österreich 2020

Impact of beamline-specific particle energy  
spectra on clinical plans in Carbon ion beam therapy.

© NIKLAS LACKNER, 2020.  
Email: lacknerniklas@hotmail.com

Supervisor TU Wien: Ass.Prof. Dipl.-Ing. Dr.techn. Karin Poljanc  
Supervisor TU Wien: Ao.Univ.Prof. Dipl.-Ing. Dr.techn. Christina Strelj  
Supervisor MedAustron: Priv.-Doz. DI Markus Stock, PhD  
Supervisor MedAustron: Antonio Carlino, PhD

Masterthesis 2020  
Atominstitut  
Technische Universität Wien  
Matrikelnummer: 1329057  
Studienkennzahl: 066 453 - BME

Typeset in L<sup>A</sup>T<sub>E</sub>X  
Wien, Österreich 2020

# Impact of beamline-specific particle energy spectra on clinical plans in Carbon ion beam therapy.

NIKLAS LACKNER  
Technische Universität Wien  
MedAustron  
January 20, 2020

## Abstract

**Purpose:** At the MedAustron (MA) Ion Therapy Centre, medical commissioning of Carbon ion beams was performed at the fixed Horizontal Beam Line in Irradiation Room 2 (IR2HBL). Carbon ion beams in the energy range of 120–402.8 MeV/u (corresponding to 29.2–270 mm range in water) and a spot size of at least 6 mm FWHM in air are available. In addition to the advantageous depth-dose profiles (compared to photons) and lateral scattering (compared to protons), Carbon ions offer a larger efficacy for tumor cells killing due to the enhanced biological effect or Relative Biological Effectiveness (RBE). Non-elastic nuclear interactions of the primary Carbon ion projectiles with the target nuclei result in a reduction of primary ions and a build-up of lower-Z fragments with longer ranges, causing the characteristic fragmentation tail beyond the Bragg peak. At MA, the treatment planning system (TPS) RayStation (RS) v8B (RaySearch Laboratories RSL, Sweden) has been commissioned. For RBE-weighted dose computation, the Local Effect Model version 1 (LEM I) is used. In order to compute the biological effect, the LEM I requires the energy spectrum of all particles and the physical absorbed dose as input parameters. RSL have used the FLUKA Monte Carlo (MC) code to compute particle energy spectra kernels of mono-energetic Carbon ion beams as input in the pencil beam dose engine (PBv3.0). Interactions with nozzle elements are handled by offsetting and weighting the spectra kernels, in order to reproduce the energy distribution at the nozzle exit. However, as the MA nozzle is not available in FLUKA, the interactions of the Carbon ion beams with the nozzle elements cannot be considered explicitly. This work aims to study the impact of beamline specific particle energy spectra on the RBE-weighted dose for clinical treatment plans.

**Materials and methods:** At MA a TPS independent MC particle transport code (Gate v8.2 Geant4 v10.3 patch 03) was used to simulate the entire beam line (IR2HBL) with the detailed description of all nozzle components. First, based on data acquired during the commissioning phase, the optics parameters, the energy, and the energy spread were tuned in Gate to reproduce the beam characteristics of IR2HBL. The hadron physics builder was chosen, comparing simulated integrated radial profiles as function of depth (IRPD) with profiles acquired with three different-sized plane-parallel ionization chambers PPIC (diameter of 39.6 mm, 81.6 mm, 147 mm) in water. Following a similar approach as RSL in FLUKA, particle energy spectra were simulated with GATE for single energy beams (ranging from 120 to 402.8 MeV/u in 5 MeV/u steps). Based on the two sets of spectra, two clinical beam models were created in RS: one beam model containing the RSL-FLUKA pre-generated particle spectra and one containing the MA-Gate beamline-specific particle spectra. The impact of the different particle energy spectra (RSL-FLUKA



---

vs. MA-Gate spectra) on the RBE-weighted biological dose was evaluated for differently sized and shaped targets in water and for some clinical plans with and without range shifter.

**Results:** Among the different hadron physics configurations, “Shielding” (containing the Quantum Molecular Dynamics model) agreed within 5% with the measured integrated depth dose profiles in the plateau and the Bragg peak region. Larger local deviations (up to 20%) were found for all the models in the fragmentation tail, but in these regions, less than 4% of the energy is deposited in comparison to the Bragg peak, therefore they are clinically not relevant. As a result, the reference hadron physics builder “Shielding” was selected for the simulation of the particle energy spectra. RSL-FLUKA pre-generated particle spectra were benchmarked against the MA-Gate beamline-specific spectra. The MA-Gate and the RSL-FLUKA fluence agreed well for the main contribution, the primary Carbon ions. However, the fluence at energies below 1 MeV/u was considerably lower in GATE for all secondary particles and mainly for the proton and helium fluence components. The dose contribution of low energy particles in the spread-out Bragg peak (SOBP) is low, but the impact on RBE-weighted dose was quantified as the RBE is non-linearly increasing with decreasing energy. Single energy layer results revealed that the compared RBE-weighted dose generated by the two different beam models, the MA-GATE and RSL-FLUKA models differ about less than 3% in the entrance region till the Bragg peak, whereas during the Bragg peak fall off region the deviation increases up to 5% and in the fragmentation tail differences of up to 15% were found. For the boxes in water three regions were investigated. The deviations found in the plateau region were less than 0.5%, in the target region less than 1% and in the fragmentation tail less than 5%. The results from the fragmentation tails were tolerable because the fragmentation tail is a low dose region, with a small absolute but a high relative dose deviation. In the five clinical cases, we investigated the dose distributions which showed differences of up to 3% restricted to local spots. The target volume dose deviations were found to be up to 2%, the maximum dose difference in the organs at risk in the clinical plans was 5.9%, although this value and other higher deviations were found when the expected (prescribed) dose for organs at risk was found to be far above the observed dose.

**Conclusion:** The correct prediction of particle energy spectra at a certain depth in tissue for Carbon ion beams is essential to assess, within acceptable clinical tolerances, the RBE-weighted dose in the patient. Therefore, it is crucial to evaluate the impact of different MC codes, non-elastic models, and nozzle components on the RBE-weighted dose for Carbon ions. In this study, an independent MC code was used to simulate the full nozzle for the IR2HBL with Carbon ions. A selection of the most suitable hadron physics configuration was made based on depth dose profiles acquired with PPIC at different radii. In total no relevant clinical differences in the RBE-weighted dose comparison in the TPS RS were found neither in the target geometries in water nor in the clinical cases in the delivered dose produced by the beam models ‘RSL-FLUKA’ and ‘MA-GATE’. Consequently, Geant4/GATE may be used to independently validate Carbon ion beams for commissioning of a Carbon ion beam model and the generation of the particle energy spectra required for the LEM I model and further the RBE-weighted dose computation.

---

## Acknowledgements

I want to express my sincere gratitude to my supervisors Christina Streli, Karin Poljanc, Markus Stock and Antonio Carlino. Thank you for your mentorship, scientific advice and support. Beyond science, thank you very much for your patience and understanding!

Special thanks to Christina and Karin for enabling this project and always having a good feeling about when to put regulations and when to give space for the project to evolve and grow.

I also want to thank Markus Stock for the opportunity to start the project at MedAustron and to grow as a research scientist. Also thank you for the trust in me to function as a representative for MedAustron at the ÖGMP 2019, it was a memorable experience.

Thanks to Antonio for his occasional motivation pushes and pressure when it was needed. Also, for showing me outside of work, how rich Sicilian culture is and how tasteful life can be! I am deeply grateful for your supervision of two great projects at MedAustron.

I want to point out my full gratefulness to Andreas for teaching me the ways of smart coding in a more significant scientific project. He made it accessible and fun for me to pick up new concepts. Andreas was like an additional supervisor to me, always spending his precious time with me to discuss on different topics and share his clever ideas.

In addition, I want to thank the Monte Carlo team of MedAustron, who gave me the opportunity to display the progress of my project and help to steer it in the right direction.

Thanks to David Boersma and Loïc Grevillot who always listened to my questions patiently and took their valuable time to answer them with brilliant comments and suggestions.

I would also like to thank RaySearch Laboratories for many fruitful discussions and a smooth, very efficient cooperation.

Last but not least I want to mention, that I had a very pleasant time at MedAustron, especially because of the friendly and enthusiastic environment.

NIKLAS LACKNER, Wiener Neustadt, January 20, 2020

# Contents

<b>1</b>	<b>Introduction</b>	<b>1</b>
1.1	Conventional cancer treatment options	1
1.2	Considerations on light ion beam therapy	2
<b>2</b>	<b>Theory</b>	<b>5</b>
2.1	Physics of ion beam therapy	5
2.1.1	Stopping of charged particles	6
2.1.2	Ranges of particles in matter	8
2.1.3	Multiple Coulomb scattering	11
2.1.4	Nuclear interactions and fragmentation	12
2.1.5	Linear energy transfer (LET) in a mixed radiation field	14
2.1.6	Track structure in a mixed radiation field	14
2.1.7	Fluence and energy fluence	16
2.2	Radibiological aspects of IBT	17
2.2.1	Dose response models for ion beam therapy and the history of biophysical models	19
2.2.2	Local effect model	19
2.3	Monte Carlo particle transport simulations	20
2.3.1	Monte Carlo codes in clinical practice	20
2.3.2	MC techniques for dose calculation	21
2.3.3	The Monte Carlo method	21
2.3.4	Particle Transport	22
2.3.5	Hadronic physics models	25
2.3.6	Electromagnetic physics constructors	28
<b>3</b>	<b>The Austrian ion beam therapy center: MedAustron</b>	<b>30</b>
3.1	Introduction	30
3.2	Accelerators for LIBT	30
3.2.1	Types of accelerators	30
3.2.2	MedAustron Particle Therapy Accelerator (MAPTA)	31
3.2.3	Active scanning beam delivery system at MedAustron	32
3.3	Treatment Planning System (TPS)	34
3.3.1	Carbon pencil beam dose algorithm	34
3.3.2	Calculation of the IRPD and particle energy spectra in water	35
3.3.3	Carbon ion dose calculation input data	35
3.3.4	Usage of GATE at MedAustron	36

<b>4</b>	<b>Beam modeling of the scanned Carbon ion beam line in GATE/Geant4</b>	<b>37</b>
4.1	Introduction	37
4.2	Materials and Methods	38
4.2.1	Measurements	38
4.2.2	Pencil beam characteristics and beam modeling procedure	41
4.2.3	Monte Carlo simulations	42
4.2.4	Physics builder selection	42
4.3	Results	43
4.3.1	Measurements	43
4.3.2	Beam modeling	44
4.3.3	Impact of different physic lists on the IRPDs	46
4.4	Conclusion	48
<b>5</b>	<b>Particle energy spectra in GATE/Geant4</b>	<b>49</b>
5.1	Introduction	49
5.2	Materials and Methods	52
5.2.1	Scoring the energy spectra	52
5.2.2	RSL FLUKA spectra simulation setup	53
5.2.3	MA GATE spectra simulation setup	55
5.3	Results	57
5.3.1	Energy spectra comparison	57
5.3.2	Fragment fluence build up comparison	60
5.3.3	Fluence averaged energy comparison	61
5.3.4	Integrated radial profiles as a function of depth	62
5.4	Conclusion	64
<b>6</b>	<b>RBE-weighted dose evaluation</b>	<b>65</b>
6.1	Introduction	65
6.2	Materials and Methods	66
6.2.1	RBE-weighted dose comparison in water geometry	67
6.2.2	RBE-weighted dose comparison in patient geometry: clinical cases in test environment	68
6.3	Results	70
6.3.1	RBE-weighted dose comparison in water geometries	70
6.3.2	RBE-weighted dose comparison in patient geometry: clinical cases in test environment	73
6.4	Conclusion	78
<b>7</b>	<b>Conclusion</b>	<b>79</b>
	<b>Bibliography</b>	<b>IX</b>

# 1

## Introduction

Section 1.1 and section 1.2 emphasize cancer as rising disease and problem following the introductory chapters of [Elia19] and also present a possible solution to it considering state of the art ion beam therapy [Pompos16].

### 1.1 Conventional cancer treatment options

In the year of 2018, cancer is the second leading cause of death globally, being responsible for about 10 million deaths worldwide.[WHO18] There are 5 prominent behavioral and dietary risks, which lead to a higher risk of evolving cancer: high body mass index, low fruit and vegetable intake, lack of physical activity, tobacco use and alcohol consumption. Smoking tobacco is ranked the highest for the mentioned essential risk factors for cancer and is responsible for approximately 22% of cancer deaths.[GBD15] From an economic point of view, the impact of cancer as a disease is significant and increasing. The financial cost of cancer in 2010 was reported to be at approximately 1.03 trillion Euro.[IARC14]

Every year about 40,000 people develop cancer in Austria. Men are slightly more affected than women. For both sexes, malignant tumor diseases are the second most common cause of death, preceded by cardiovascular diseases.[KSA18]

Three pillars of cancer treatment techniques can be mentioned: surgery, systemic treatment and radiation therapy. The choice upon these three therapies is complex and not always straight forward. It depends, among other things, on where the tumor is located, the stage of disease and the clinical history of the patient. If possible, a complete resection of the tumor is favorable due to having almost no impact on the healthy tissue and also a high probability of rapid recovery. This method can be used in benign tumor cells but is more complex in the case of a malign tumor. The ability of the malignant cells to spread over adjacent sites can lead to infiltration of nearby organs and to metastasize in the bloody and bony tissue. Therefore considering additional treatments like radiotherapy and systematic treatment is necessary to increase the probability of tumor control. Those methods are invasive and can cause harm in healthy tissue. To keep these negative side effects as low as possible further development has to be done. The rise of new techniques and methods against cancer is noticeable and ion therapy is playing a significant role as a valid alternative to conventional radiotherapy for more than 60 years.[Wilson46]

## 1.2 Considerations on light ion beam therapy

When we refer to ion beam therapy, we distinguish between light and heavy ion beam therapy. Light ion beam therapy (LIBT) is dealing with ions with an atomic number of less than ten. The main reason to consider LIBT is the advantage to be able to spare the surrounding healthy tissues in comparison to conventional radiotherapy (photons and electrons). Nowadays, most patients receive treatment with photons. As photons (x-rays) are produced from an external source and due to their physical interaction with matter, most of their energy is deposited before the tumor, in healthy tissue. Energy deposition also occurs beyond the tumor, affecting additional healthy tissue. A significantly lower amount of patients are treated with ion beams, mostly due to limited availability of ion beam therapy facilities. The reason for superior physical properties over photons is that ions carry electric charge and are heavier. These different physical properties result in a different interaction with matter which we describe in detail in Section 2.1. This leads to sparing of healthy tissue compared to conventional radiotherapy. However, there are limitations for ion beam therapy, like lateral scattering and uncertainty in the physical range. [Pompos16] A statistic of 2018 [PTCOG18] shows that more than 220000 patients have been treated with Particle Therapy worldwide. About 190000 of them have been treated with protons, about 28000 with Carbon ions and 3500 with Helium, pions and other ions.

If ions such as Carbon reach the end of their track in the target, their biological effectiveness is massively increased (up to 3-4 times), while they show comparable relative biological effectiveness in normal tissue as photons. A graph showing the biological effectiveness vs. the physical dose distribution advantage of different treatment modalities can be seen in 1.1. This makes heavier ions unique as they can effectively attack radioresistant tumors and overcome the therapeutic problems of hypoxia. [Kamada15] The exact evaluation of the relative biological effectiveness (RBE) of ions along their path is complex and often treatment planning systems are not sophisticated enough and need to bypass the detailed description of the RBE-weighted dose by approximations. This thesis is a small step of many needed for the accurate description of the RBE-weighted dose ion beam therapy.

Since 1994, the National Institute of Radiological Sciences (NIRS) in Chiba, Japan, has treated more than 8000 cases with Carbon. This long term collected clinical experience shows that Carbon ions are effective in treating complex solid tumors, including adenocarcinoma, malignant melanoma, various types of sarcomas and adenoid cystic carcinoma. NIRS played a leading role for Carbon ion beam therapy in Japan and lead to the planning and establishment of five additional centers in Japan. Other particle therapy centers able to treat with carbon available in Europe beside MedAustron (Austria) are HIT in Heidelberg (Germany), MIT in Marburg (Germany) and CNAO in Pavia (Italy). Above 80 ion beam therapy centers are currently operating worldwide and several more centers are under construction. [PTCOG18].

Figure. Biological Effectiveness vs Physical Dose Advantage

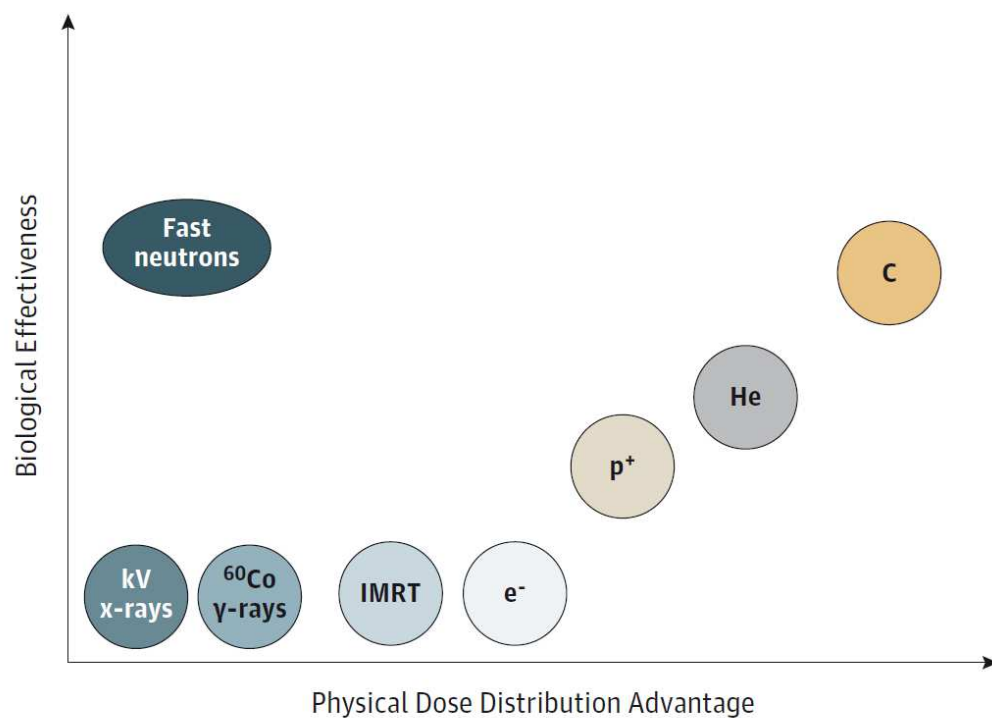


**Figure 1.1:** Biological effectiveness of different treatment modalities. [Pompos16]

The most intimidating obstacle in developing light ion beam therapy centers are the high initial capital costs. The complexity of the system which is needed to accelerate the ions to reach deeply seated tumors elevates the costs of a light ion therapy system compared to conventional photon beam therapy. Right now, accelerator and beam delivery system research should continue to be supported by the government and private industry. This would lead to commercialization of the next-generation accelerator and beam delivery systems that are more accurate and precise and, most importantly, less costly to build and maintain, which furthermore would result in a wider availability for patients in need. [Pompos16] A comparison and status for different treatment modalities from the year of 2016 can be found in Table 1.1.



Parameter	X-rays	Protons	Carbon Ions
Volume of irradiated normal tissue	Large	Small	Smallest
Biological effectiveness			
In normal tissue	Low	Low	Low
In tumor tissue	Low	Low	High
Targeting precision	Low	High	Highest
System cost	Low	High	Highest
Worldwide centers, No.	Thousands	55	10
Worldwide treated patients, estimate	Millions	120 000	15 000

**Table 1.1:** Comparison of X-rays, protons and light ions.  
[Pompos16]

The choice of the optimal projectile is not trivial and is an ongoing discussion in radiotherapy. Studies have shown that neon and Carbon ions are very promising particles and most suitable for the needs of ion beam therapy. [Chu06][Scholz03] However, the topic remains open, the data for a detailed analysis of the physical and biological properties of the ions and a final decision is not yet sufficient.



# 2

## Theory

This chapter aims to provide the contextual background for the master thesis. We describe the physical principles of ion beam therapy (IBT) [Sanchez-Parcerisa12], the role of radiobiology in the patient dose calculation [Chanrion16] and finally Monte Carlo Simulations in radiotherapy [Boehlen12, GEANT4] will be considered.

### 2.1 Physics of ion beam therapy

Ion beam radiotherapy offers a superior dose deposition over conventional radiotherapy comparing the beam to beam dose deposition. Photons as well as electrons deposit the largest amount of their energy in the beginning of their interaction path, while protons and Carbon ions deposit most of their energy in the form of a peak at a deeper point, which is called the Bragg peak. The described behavior of the various particles is shown in Figure 2.1. The Bragg peak can be used to deliver conformal dose to a tumor while sparing surrounding healthy tissues. The peak is determined by the characteristics of electromagnetic and nuclear interactions of the projectiles with the target medium and the depth at which it appears can be controlled by tuning the initial energy of the ions.

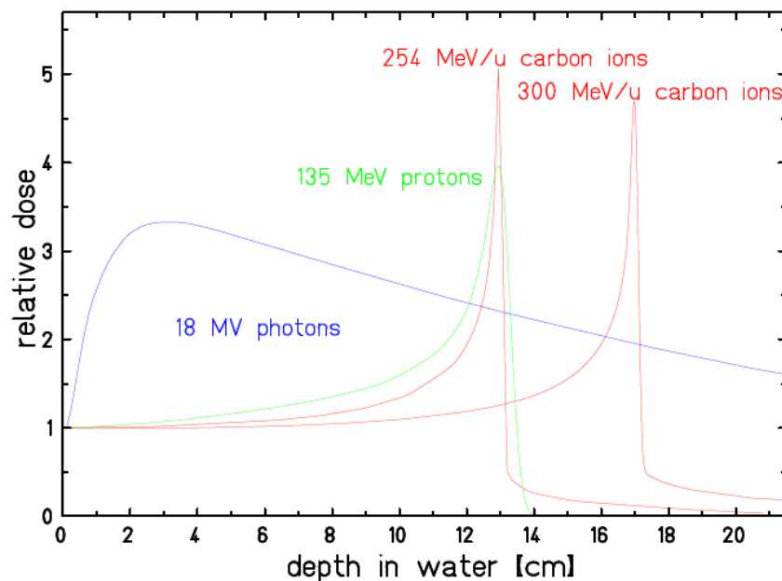
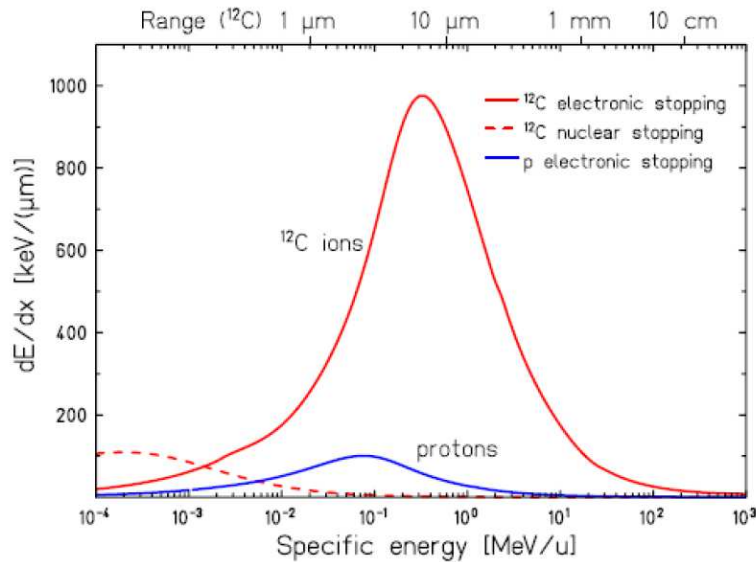


Figure 2.1: Depth dose profiles of photons, protons and Carbon ions. [Haettner06]

### 2.1.1 Stopping of charged particles

For light ions the energy loss is dominated by the electromagnetic interaction with the electrons in the medium with a little fraction of energy loss being attributable to the positive cores (nuclear stopping), as shown in Figure 2.2. Nuclear reactions play a bigger role, if the ions get heavier, while for protons they only play a minor role.



**Figure 2.2:** Stopping power of  $^{12}\text{C}$  ions and protons in water as a fraction of specific energy. On the top axis, the corresponding range in water for Carbon ions. [Schardt10]

The definition of stopping power in a medium, is the average ion energy loss per unit path length [ICRU94] and can be described by the Bethe-Bloch equation [Bethe30, Bloch33]. Since 1933 the initial equation has been modified and a detailed review of the updated equation can be found in [Ziegler99].

Above approximately 1 MeV/u the equation retains validity [ICRU94]. It expresses the mass stopping power of a medium, in terms of the stopping number  $L(\beta^2)$ , as

$$\frac{S}{\rho} = \frac{4\pi r_e^2 m_e c^2}{\beta^2} \frac{1}{u} \frac{Z}{A} L(\beta^2). \quad (2.1)$$

$r_e$  is the classical electron radius,  $m_e c^2$  is the electron rest mass energy,  $\beta$  is the particle velocity as a fraction of the velocity of light in vacuum,  $u$  is the atomic mass unit,  $Z$  is the atomic number of the target medium and  $A$  is the mass number of the target medium.

The stopping number,  $L(\beta^2)$ , is usually expressed as a power series of  $z$ , which represents the atomic number of the projectile, up to second order,  $L(\beta^2) = L_0 + zL_1 + z^2L_2$ . Therefore the stopping number can be written as

$$L(\beta^2) = \left[ \left( \frac{1}{2} \ln \frac{2m_e c^2 \beta^2 \Delta E_{max}}{1 - \beta^2} - \beta^2 \right) - \ln \langle I \rangle - \frac{C}{Z} - \frac{\delta}{2} \right] + zL_1 + z^2 L_2. \quad (2.2)$$

In eq. 2.2,  $f(\beta^2)$  represents the first expression in brackets, which accounts for most of the dependence of the stopping number with the particle velocity.  $\Delta E_{max}$  is the largest energy loss in a single collision possible.  $\Delta E_{max}$  can be approximated to  $\approx \frac{2m_e c^2 \beta^2}{1 - \beta^2}$  [Ziegler1999], which yields a simplified expression for  $f(\beta^2)$ ,

$$f(\beta^2) = \ln \frac{2m_e c^2 \beta^2}{1 - \beta^2} - \beta^2. \quad (2.3)$$

The second term,  $\ln \langle I \rangle$  represents the logarithm of the mean ionization potential of the medium, which encloses most of the dependence on the target material.  $\frac{C}{Z}$ , the shell correction term, accounts for the internal structure of the target atoms, only significant at low energies, in the range of a few MeV/u.  $\delta/2$ , the density correction factor, accounts for polarization effects in solid media and only plays a role for ultrarelativistic energies, above 1 GeV/u.  $zL_1$ , the Barkas first-order correction, models the difference between negatively and positively charged projectiles. This term has decreasing importance with increasing particle energy.  $z^2 L_2$ , the Bloch second-order correction, is only relevant at low energies. To demonstrate the influence of the corrections on the Bethe Bloch equation the contributions of the different terms are shown in Table 2.1 The relevant energies for particle therapy are in the MeV/u range.

Percent contribution towards Stopping Number L						
<i>Proton Energy (MeV)</i>	<i>L<sub>0</sub></i>	<i>f(β)</i>	<i>Shell+ ln&lt;I&gt;</i>	<i>δ<sup>2</sup> Density Corr.</i>	<i>L<sub>1</sub> Barkas Corr.</i>	<i>L<sub>2</sub> Bloch Corr.</i>
1	95.95	309.5	-207	-0.0004	5.239	-1.187
5	98.84	227.7	-126.1	-0.0007	1.308	-0.1479
10	99.25	208.2	-107.3	-0.0016	0.8124	-0.0632
50	99.7	180.5	-80.48	-0.0133	0.3116	-0.0101
100	99.79	173.2	-73.15	-0.0388	0.2141	-0.0049
1,000	99.93	157.8	-56.85	-0.9614	0.0661	-0.001

**Table 2.1:** Percentage contribution to stopping power number L for protons in aluminium, of the different correction terms for the Bethe Bloch (eq. 2.1). [Ziegler99]

In the clinical energy range, the biggest correction appears to be from the  $\ln \langle I \rangle$  term. It is common to adjust I to the experimental data, where it is available and to interpolate it where it is unavailable [Gottschalk04].

As  $L(\beta^2)$  varies with  $\beta^2$ , the term on  $\frac{1}{\beta^2}$  from (eq. 2.1) dominates in the therapeutic energy region. As velocities rise, atoms start to lose their electrons and the projectile

charge is equal to the atomic charge number  $Z$ . At lower energies,  $Z$  in (eq. 2.1) has to be replaced by effective charge  $Z_{eff}$ , given by the empirical (eq. 2.1.1) [Barkas63], due to ionization and recombination processes.

$$Z_{eff} = Z[1 - \exp(-125\beta Z^{-\frac{2}{3}})] \quad (2.4)$$

The Bragg peak position is determined by the maximum energy-loss rate. The maximum energy loss rate for protons is about 25 keV and about 350 keV/u for Carbon ions

A more detailed view on the physical processes of stopping particles in matter can be found in the ICRU Reports 49 and 73. [ICRU94, ICRU05]

## 2.1.2 Ranges of particles in matter

If the stopping power of a charged particle in a medium is given, the pathlength  $P$  of a particle with kinetic energy  $T$  can simply be numerically calculated by [Janni82]

$$P(T) = \int_T^0 \left( \frac{dE}{dx} \right)^{-1} dE. \quad (2.5)$$

This approach is called continuous slowing down approximation (CSDA). In the case of charged particles, it is very similar to its mean range of  $R$ , which is the traversed absorber thickness. The heavier the ions, the less they scatter, which results in their trajectory being an almost straight line. Energy loss happens mostly due to ionization and it is prone to statistical fluctuations. This leads to different paths and penetration depths of particles with identical initial energy. This results in a broadening of the peak in the depth dose distribution, especially for lighter ion beams. This phenomenon is called energy- or range-straggling. [ICRU94, ICRU05, Sigmund09].

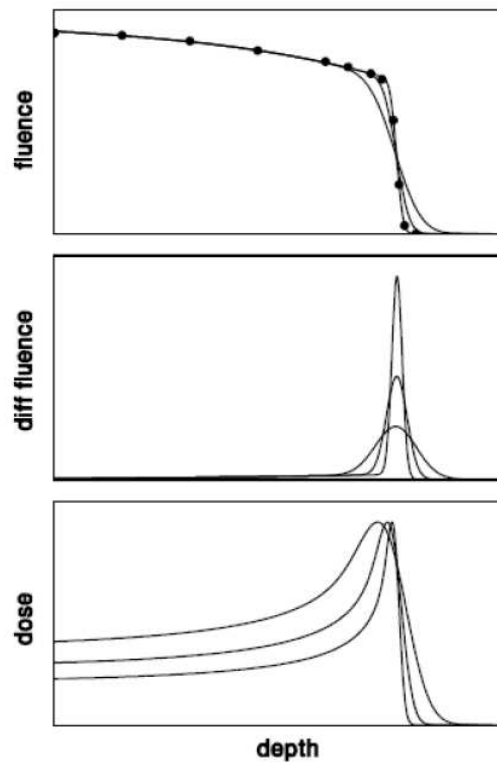


**Figure 2.3:** Illustration of  $R0 = d80$  [Bortfeld97]. Different measurements with three proton beams of the same energy and with different initial energy spreads. Top: fluence, Middle: differential fluence in energy, Bottom: dose distribution [Gottschalk04]

Energy loss caused by the transfer via electromagnetic interaction with the target electrons of the particles follows a Gaussian distribution for a sufficiently thick absorber [Schardt2010]. The variance of the range straggling  $\sigma_R^2$  is correlated to the variance of energy losses  $\sigma_E^2$ . The formula gives the width of the range straggling

$$\sigma_R = \frac{R}{\sqrt{m}} f\left(\frac{E}{mc^2}\right). \quad (2.6)$$

$E$  and  $m$  are the projectile's energy and mass and  $f$  is a slowly varying function which accounts for the medium dependence [Rossi52]. Carbon ions experience less straggling, by a factor of 3.5, compared to protons due to the term  $\frac{1}{\sqrt{m}}$ .

The definition of the range in a beam is the distance at which half of the fundamental particles have stopped [Gottschalk04]. Therefore information about the particle fluence is essential, but it is the dose distribution what is most often measured or characterized. The work of [Bortfeld97] brings these two concepts together. The expression  $R0 = d80$  represents the mean range, which is equal to the distal 80% point of the Bragg peak. Figure 2.3 shows this for different beam energy spreads for proton beams of the same initial energy.

In the work of [Bortfeld97], a power law relation between ranges and initial energies of particles beams has been established in the form of  $R_0 = \alpha * T^\beta$ , which is shown in Figure 2.4 for the clinical energy range.

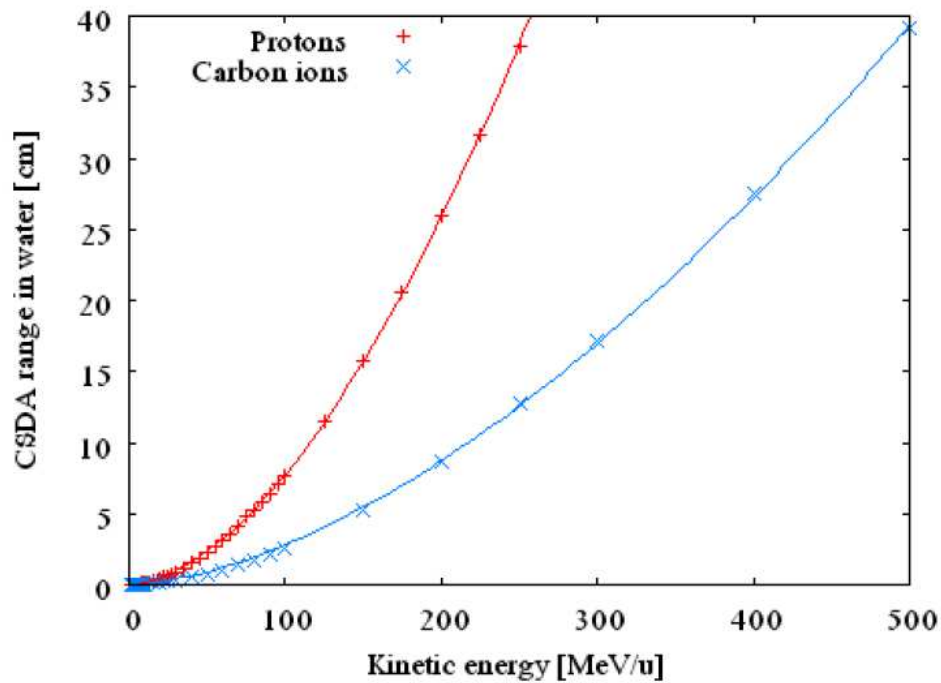


**Figure 2.4:** Relation of range and energy for protons and Carbon ions in water. Data taken from [ICRU94] and [Sigmund09] fit to  $R_0 = \alpha * T^\beta$  with  $\beta=1.65$  for Carbon ions and with  $\beta=1.74$  for protons.

### 2.1.3 Multiple Coulomb scattering

Multiple Coulomb scattering leads to the spread of a beam of charged particles along their path through a medium. Multiple Coulomb scattering is the result of numerous single Coulomb scattering events with the atomic nuclei. From a classical point of view, the ratio of masses between the projectile and the target determines the angle and the energy transfer of the scattering. Therefore, atomic electrons are negligible when we investigate the scattering of ion beams since their mass is roughly about 1836 times lower than that of the incident protons. The heavier an ion is, the less it suffers from scattering and thus heavier ions have a narrow shape of the lateral penumbra which is beneficial for accurate dose deposition in clinical use.

The foundation of the multiple scattering theory was set by Molière, who studied the single scattering in the Coulomb field of a nucleus and then did combined analysis with the statistical effect of several nuclei [Moliere47, Moliere48]. Molière had some assistance of Bethe [Bethe53] and Fano [Fano54] who contributed with some minor corrections to his model. Today the theory is seen as complete and valid [Gottschalk93].

A simple approximation of the multiple scattering theory can be computed by quadratically adding up the results from the single scattering events at each step, making use of the central limit theorem. With this rough estimation, the outcome follows a Gaussian distribution for the scattered angle. This approach is only valid if the single scattering contributions are small enough [Gottschalk93], which is not the case for Rutherford scattering (single scattering in the Coulomb field of a nucleus).

In Molière's theory, the single Gaussian parameter is replaced by a more sophisticated set of parameters, which is also dependent on the target particle and the properties of the projectile. An angular distribution with a three-term power series is the result, the former term of the series is a Gaussian. For the particular condition of small angles, this more sophisticated approach can be approximated by a Gaussian distribution which is not precisely the first term of the series. [Gottschalk04]

Lynch and Dahl [Lynch91] suggested that an approximation, by a Gaussian function, of the scattering angle distribution can be applied

$$f(\theta, \phi)d\theta d\phi = \frac{1}{2\pi\theta_L^2} e^{-\frac{1}{2}\left(\frac{\theta}{\theta_L}\right)^2} d\theta d\phi, \quad (2.7)$$

where the mean scattering angle,  $\theta_L$ , is expressed by the empirical Highland's formula [Highland75]



$$\theta_L = \frac{13.6 \text{ MeV}}{pv} z \sqrt{\frac{L}{L_R}} \left[ 1 + 0.088 \log_{10} \left( \frac{L}{L_R} \right) \right], \quad (2.8)$$

where  $p$ ,  $v$  and  $z$  are the momentum, velocity and charge of the projectile.  $L$  and  $L_R$  are the target thickness and the radiation length respectively.

### 2.1.4 Nuclear interactions and fragmentation

In addition to electromagnetic interactions, ions undergo nuclear interactions, induced by nuclear forces.

We distinguish between two types of nuclear interactions: elastic and non-elastic. [ICRU2000] A scatter process is considered elastic if the total kinetic energy is conserved, so a target nucleus scatters the projectile and they both keep their internal state constant. For nuclear interactions which are non-elastic the kinetic energy is not conserved, which means the target nucleus or the projectile (or both) undergo nuclear fragmentation, or they do change their quantum state. Another interaction occurs if an ion species conserves their identity before and after the collision, and only changing their quantum state.

The most common nuclear interactions for particle therapy are non-elastic. They usually happen as a two-step process, which is shown in Figure 2.5. A more precise description can be found in [Serber47]. Two nuclei overlap and form an excited system, which is later de-excited as fragments leave the system or change their internal quantum state.

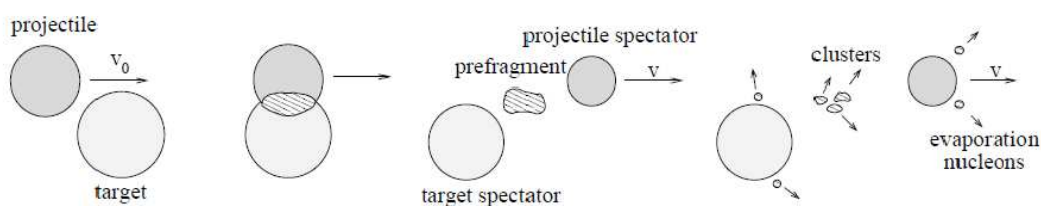


**Figure 2.5:** Nuclear fragmentation as a two step process. [Haettner06]

Nuclear interactions have an impact on the particle fluence. The number of primary particles decreases as the beam travels through matter, which means that the primary particles undergo nuclear non-elastic interactions and lighter fragments and other secondaries will replace the heavier primary particles. Figure 2.6 shows the build-up of different fragments for a typical Carbon ion beam at therapeutic energies.



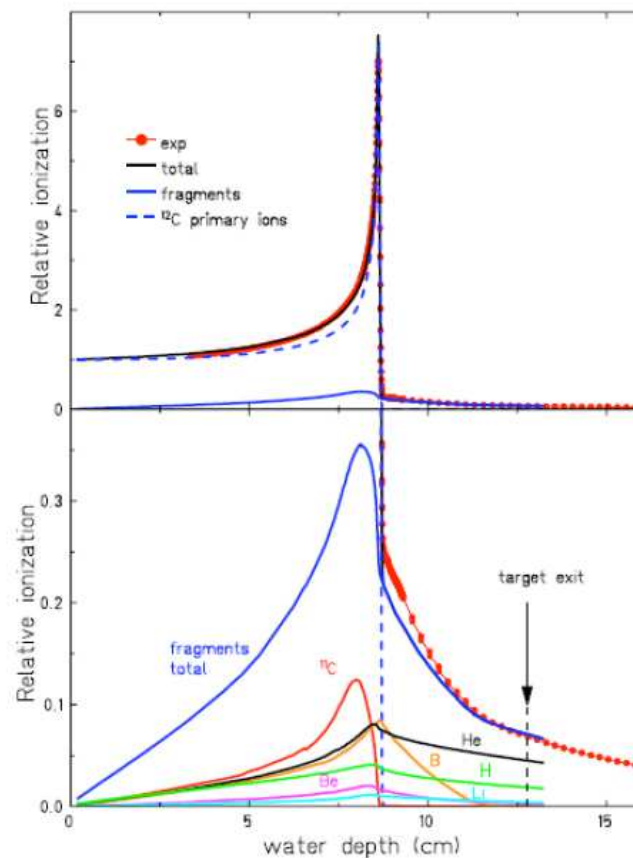


**Figure 2.6:** The image on the top shows a depth dose distribution of a 200 MeV/u Carbon ion beam. The black line represents the total dose, blue dashed and solid lines are primary ions and its fragments. (calculated with MC code PHITS [Nitta06])

The image on the bottom shows the Bragg peak build up and fall off. [GunzertMarx08]

Characteristic for those interactions are the charge-changing and nuclear cross sections. The cross sections for protons are presented in [ICRU2000], while for a selection of heavier ions, cross sections are available in [Boehlen10], but due to a limited amount of data, the cross sections for the latter suffer from a higher amount of uncertainties.

Nuclear effects are barely visible in a depth dose distribution for protons but as the ions get heavier the amount of dose produced by nuclear effects is clearly noticeable in the depth dose distribution. Primary particles heavier than protons show the characteristic dose tail, which is caused by secondary fragments, mainly protons, deuterons and Helium particles. Projectile fragments keep most of the velocity of the primary particle, but due to their lower charge, their electromagnetic interaction with the target is weaker, so they can reach beyond the range of the primaries, forming a tail. To essentially model the effects of charged particles and furthermore the radiobiological effects, a precise knowledge of the fluence of primary and secondary particles is important. Individual particles deposit energy in different ways and thus originate different radiobiological effects.

### 2.1.5 Linear energy transfer (LET) in a mixed radiation field

As already mentioned in the previous Section, the Carbon ions experience inelastic nuclear interactions along their track due to their interaction with matter, which leads to nuclear fragmentation and thus to the production of numerous recoil ions. This secondary charged particles create a mixed radiation field, which has to be considered in the prediction of the dose in the Treatment Planning System (TPS) and plays an important role in the prediction of biological effects. A mixed radiation field is defined via the particle  $T$  and energy  $E$  for each particle  $(T_i, E_i)$  and contributes to the total dose with a fraction  $f_i$  that is voxel dependent.

Each voxel yields a biological effect, related to the dose deposited in it. Therefore the dose-average LET has to be calculated in each voxel. [Kanai97, KraemerScholz06] The definition of the dose average LET follows the [ICRU70] and it is a distribution generally expressed as

$$\overline{LET}_{Dp} = \frac{\int_0^\infty L^2 t(L) dL}{\int_0^\infty L t(L) dL}, \quad (2.9)$$

where  $t(L)dL$  represents the fraction of the total track length  $T$ , describing values of the LET between  $L$  and  $L + dL$ . Each radiation component  $j$ , of any type and energy, is taken into account in order to calculate the dose average LET in a pixel  $p$ . With this consideration, the previous equation can be written as

$$\overline{LET}_{Dp} = \frac{\int_j r_j LET_j dj}{\int_j r_j dj}. \quad (2.10)$$

In (eq. 2.10),  $dj$  describes the dose, while  $r_j$  represents the weighting factor for each radiation component  $j$ . This calculation of the biological response in a mixed radiation field can be time consuming and a complex task.

### 2.1.6 Track structure in a mixed radiation field

To estimate the impact of the charged secondary particles of our fragmented Carbon ion beam, we need to take a look at the track structure in a mixed radiation field. Electrons of the medium are ejected around the ion trajectory for each ion in the beam. This causes a distribution of ionizations and excitations around the ion path, which is referred to as track structure. The track structure of a low energetic Carbon ion beam is shown in Figure 2.7. Delta electrons are ejected in the forward track and delta-electrons are interacting with the medium resulting in a penumbra. To calculate the biological effect, models often use amorphous track structure models to compile and add up the numerous particle tracks, as well as to calculate the energy deposition. Track structures can also be represented by radial dose models, which expects the average dose at a certain point from the center to the ion trajectory. For each track, the radial dose  $D(r)$  is calculated.

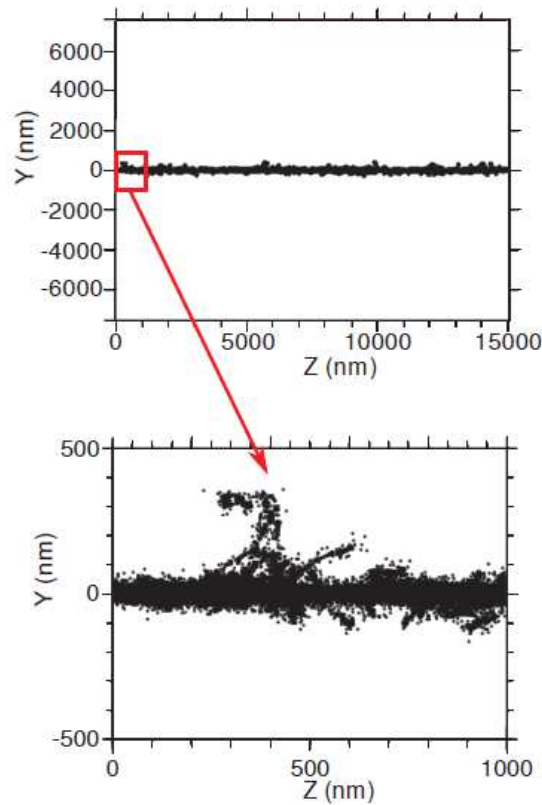


**Figure 2.7:** Track structure of a 24 MeV Carbon ion beam. On the top, the track is recorded along 15000 nm. On the bottom, the first  $\mu\text{m}$  is depicted. (figure adapted from [Colliaux09]).

The first to propose the use of track theory for heavy particle therapy was [KatzSharma74]. [Waligorski86] has used track theory for the calculation of the radial dose in the frame of cell inactivation. [ScholzKraft96] have proposed an advanced model with the use of the normalization factor and  $r$  the radial distance. If we integrate the whole track, the result is the LET and for  $r < r_{min}$  the radial dose distribution is a constant. A detailed description of the advanced radial dose distribution has been given in [ElsaesserScholz07] as follows

$$D(r) = \begin{cases} \frac{\lambda LET}{r_{min}^2} & \text{if } r < r_{min} \\ \frac{\lambda LET}{r^2} & \text{if } r_{min} \leq r \leq r_{max} \\ 0 & \text{if } r > r_{max} \end{cases} \quad (2.11)$$

where  $\lambda$  is a normalization constant and  $r$  the radial distance to the primary ion track. With  $r > r_{max}$  the dose gets negligible. It has been found by [ElsaesserScholz07] that  $r_{min} = 10 \text{ nm}$ . Total dose contribution around the track can be expressed as

$$S_e = \int_0^{r_{max}} 2\pi D(r) r dr = \int_0^{r_{min}} 2\pi a r dr + \int_{r_{min}}^{r_{max}} 2\pi \frac{a r_{min}^2}{r^2} dr. \quad (2.12)$$

An alternative track structure model is the Kiefer-Chatterjee model. Explained by [Kase08] this model combines the Kiefer model [KieferStraaten86] for the

description of the penumbra track structure, while it uses the Chatterje model [ChatterjeSchaefer76] for the core radius description. In this combined model, the core radius  $R_c$ , is expressed with the ion velocity relative to the light velocity

$$R_c = 0.0116 \times \beta_{ion}. \quad (2.13)$$

The description of the penumbra radius  $R_p$  is as follows

$$R_p = 0.0616 \times \left(\frac{E}{A}\right)^{1.7}, \quad (2.14)$$

with the energy  $E$  and  $A$  being the mass number. The penumbra dose  $D_p$  and the core dose  $D_c$ , which is constant are formulated by

$$D_p(r) = 1.25 \times 10^{-4} \left(\frac{z^*}{\beta_{ion}}\right)^2 r^{-2}, \quad (2.15)$$

and

$$D_c(r) = \frac{1}{\pi R_c^2} \left( \frac{LET_\infty}{r} - 2\pi K_p \ln\left(\frac{R_p}{R_c}\right) \right). \quad (2.16)$$

In (eq. 2.15)  $z^*$  describes the effective charge (similar to (eq. 2.1)), while  $\beta_{ion}$  is the ions velocity relative to the velocity of light in vacuum following [Sakama05].

In the track core, the number of events and also the energy transfer is high enough to quantify the radial dose in the core as an average. This is not the case for the penumbra track. Events are very fluctuating in event number and energy transfer. Therefore an average dose for describing the penumbra track would lead to wrong estimations in many cases. Inaccuracies in this model were evaluated by [Beuve09].

### 2.1.7 Fluence and energy fluence

According to ICRU report 85 [ICRU85]  $\Phi$ , the fluence, described as the quotient of  $dN$  by  $da$ , where  $dN$  is the number of particles incident on a sphere of cross-sectional area  $da$ , thus

$$\Phi = \frac{dN}{da}. \quad (\text{Unit: } m^{-2}) \quad (2.17)$$

and  $\Psi$ , the energy fluence, the quotient of  $dR$  by  $da$ , where  $dR$  is the radiant energy incident on a sphere of cross-sectional area  $da$ , thus

$$\Psi = \frac{dR}{da}. \quad (\text{Unit: } Jm^{-2}). \quad (2.18)$$

Using a sphere of cross-sectional area,  $da$  is the most simple way to consider the area  $da$  perpendicular to the direction of each particle. It has been mathematically demonstrated by Papiez and Battista [PapiezBattista94], that the ICRU fluence definition is equivalent to :

$$\Phi = \frac{dl}{dV}, \quad (2.19)$$

where  $dl$  expresses the length of particle trajectories in the observed volume  $dV$ .

## 2.2 Radibiological aspects of IBT

The aim of radiotherapy is the destruction of tumor cells by means of ionizing radiation and this is achieved by damage in the DNA. The destructive potential of a radiation type depends on the type and intensity of the induced lesions. Radiation damage can result in single-strand breaks (SSB) or double strand breaks (DSB). SSB are lesions where only one strand of the DNA double helix breaks and they are compared to DSB easy to repair by the DNA repair mechanisms. DSBs, where one strand breaks twice or both strands are damaged, are more complex to regenerate for the repair mechanisms and most cell killing is induced by clustered DSBs in the DNA.

Direct or indirect damage can be caused to the cell, by the action of radiation. Direct damage results from directly deposited energy into the DNA, whereas indirect damage can be caused by radiation within the molecular environment surrounding the DNA forcing chemical reactions with the molecule. In a cell environment which suffers from hypoxia (decreased oxygen supply), indirect damage is often reduced, because less toxic chemical reactions happen, which results in large radioresistance of the tissue.

To be able to do precise treatment planning, it is mandatory to understand the survival response of the cells to irradiation. A universal and commonly accepted model, with room to improve, shows the relation between the cell survival  $S$  and the absorbed dose  $D$  is the so-called linear-quadratic (LQ) model, which is expressed as

$$S(D) = e^{(-\alpha - \beta D^2)}, \quad (2.20)$$

where  $\alpha$  and  $\beta$  are parameters, that depend on the cellular properties.

The ratio of these two parameters  $\frac{\alpha}{\beta}$  indicates the radiosensitivity of a particular tissue type.

To compare the effect of photon radiotherapy with the effect of charged particle radiotherapy, the concept of relative biological effectiveness (RBE) was introduced, as the ratio of photon dose to the dose with any other particle to produce the same biological effect (see Figure 2.8).

The actual value of the RBE will depend on the endpoint and commonly referred endpoints in cell survival are the  $RBE_{50}$  (survival of 50% of the cells) and the  $RBE_{10}$  (survival of 10% of the cells).

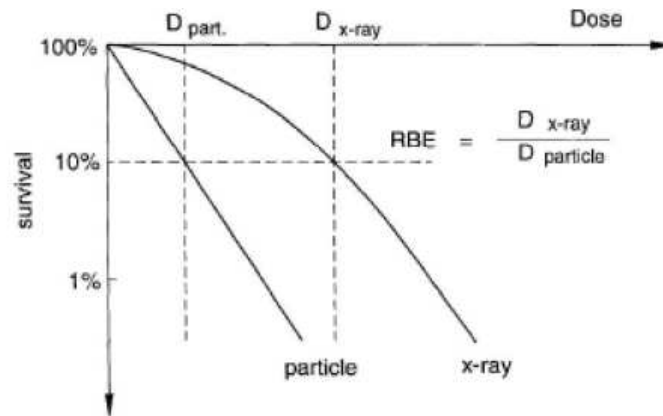


**Figure 2.8:** Definition of the RBE demonstrated via cell survival curves. [Kraft00]

The RBE of charged particles depends on their energy exhibit. To control the total energy deposition in the healthy region and tumor area, a selective increasing RBE in the Bragg peak area over the entrance channel is advantageous.

In clinical proton radiotherapy, the RBE value is approximated to be constant, equal 1.1 and used to weight the dose, which is shown in Figure 2.9. It remains an approximation and studies show a dependency of the RBE on tissue type. [Paganetti16] In Carbon ion therapy, the calculation of RBEs is complex, since it varies along the beam path because of differences in LET and particle spectra seen in Figure 2.9. There are two prominent approaches to calculate the RBE for Carbon ion beams used for patient treatments, namely, the Local Effect Model (LEM) and the Microdosimetric Kinetic Model (MKM).

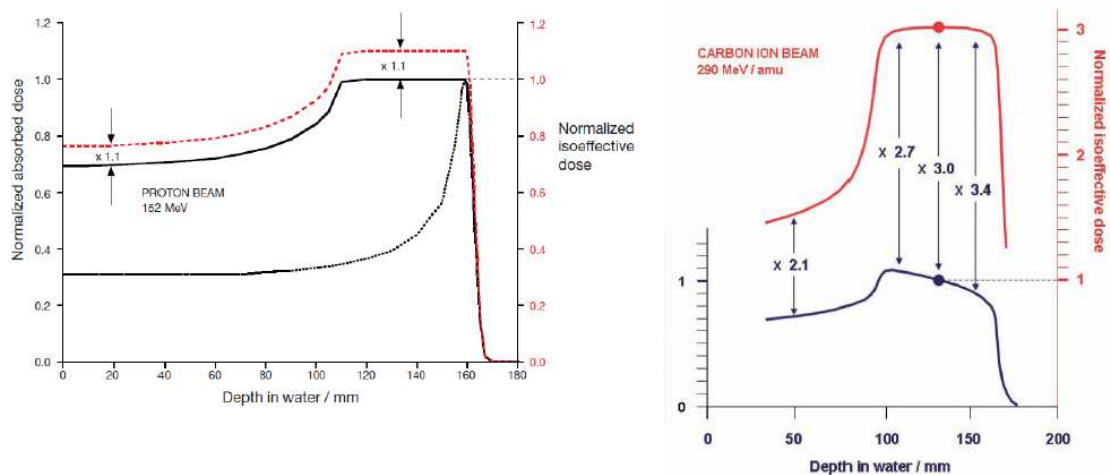


**Figure 2.9:** RBE weighted dose (red) and physical dose (black) distributions are shown for protons (left). [IAEA2008]



### 2.2.1 Dose response models for ion beam therapy and the history of biophysical models

In the past 40 years there were several proposals for high-LET beam dose response models. It is usual to define the biological endpoint with x-ray and in vitro. As already mentioned in the previous Section, the RBE is defined as the dose of ions which is needed for the same level of effect as the dose which is induced by photons. Different biophysical models for different purposes (clinical, mechanistic and microdosimetric) were developed for modeling RBE in various high-LET applications. Neutron therapy was a standard clinical high-LET treatment offered to large cohorts of patients, especially in Asia. [CarabeFernandez07] explains the [KellererRossi72] measured RBE values for a range of biological endpoints and several high-LET particles, with a whole "theory of dual radiation action". To briefly explain the theory, it is based on the assumption that lesions in the DNA are created by pairs of sub-lesions together with microdosimetric considerations paired with quantification of the radial dose. Pairs of sub-lesions which occur at a sensitive site will result in a certain biological effect. In the theory of dual radiation action, the biological effect is highly correlated with energy deposited in the sensitive site. In Japan at NIRS, pioneers of Carbon-ion beam therapy, used an approach based on their yearlong experience of therapeutic neutron beams and a dose-response model which depends on well known in vitro cell lines, that can be found in [Kanai99]. This model later evolved into the microdosimetric kinetic model (MKM) [Inawa10] and more recently into the modified microdosimetric model (MMKM) [Yizheng17]. At Europe in GSI and Heidelberg, the Local Effect Model (LEM) is used in clinical treatment, which also covers the calculation of the lethal damage of ions under several conditions of irradiation. These models are continuously improved and also the fundamentals do change, for instance, by the influence of the probabilistic two-stage model by [Kundr05].

In the following, only the biophysical model implemented in the clinical treatment planning systems (TPS) at MedAustron, which is in use for patient treatments, will be presented.

### 2.2.2 Local effect model

At MA, CNAO, GSI, HIT and MIT, an active beam scanning system is used to allow better dose conformity. The biological effectiveness differs for each spot scan and voxel, therefore an analytical radiobiological model rather than a fixed table of RBE values is preferred. MA, CNAO GSI, HIT and MIT are using the Local Effect Model (LEM). [Scholz97, KraemerScholz00, Kraemer06].

The basic idea of the LEM is that a cell will get inactivated after ion irradiation is determined by evaluating the local spatial dose distribution inside the cells nucleus. The local spatial dose is calculated with a track structure. It is a radial dose model which is considered in a subvolume. Further, more lethal effects are calculated independently of the radiation quality with the linear quadratic model (LQ), which uses parametrized cell response compared to photons. In the end, the biological effects in the subvolumes are calculated and are integrated to estimate the total survival

probability.

1. Assuming that the distribution of lethal events follow a Poisson distribution, the cell survival probability is

$$S(D) = e^{-N_{lethal}(D)}. \quad (2.21)$$

2. Dose-response of a cellular system affected by ion radiation with the particle type  $T$  and the energy  $E$  follows the behavior (LQ model)

$$-\ln(S) = \alpha_z D_z + \beta_z D_z^2, \quad (2.22)$$

and  $D_z$  is the specific energy deposited by a particular ion type  $T$  with energy  $E$  in the cell nucleus.  $\alpha_z$  and  $\beta_z$  are the parametrized radiosensitive values for a single monoenergetic particle.

3. The local dose  $D_z$  is calculated via a track structure radial dose model. With this local dose, calculated in all three dimensions  $x, y, z$ , the number of lethal events calculates as

$$N_{ion} = \int_{V_{nucleus}} dV v_{ion}[d(x, y, z)], \quad (2.23)$$

where  $v_{ion}$  represents the lethal event density.

4. It is assumed that the local dose can be directly connected to the macroscopic dose  $D$ , neglecting the stochastic effects.  $v_{ion}$  can then be directly linked to the lethal event density of the radiation of reference.

$$v_{ion}(d) = v_x(d) = -\frac{\ln(S_x)}{V} \quad (2.24)$$

5. The final consideration that the sensitive sites are distributed homogeneously over the cell nucleus leads to

$$N_{ion} = -\int_{V_{nucleus}} dV \frac{\ln(S_x)}{V}, \quad (2.25)$$

and  $\ln(S_x)$  is taken from the LQ model. To predict  $\ln S_x$  the LQ needs four input parameters,  $\alpha, \beta, D_t$  and  $r_{nucl}$ , while LEM I provides an initial calculation of the initial cell survival for a monoenergetic particle. These four input parameters are listed in look-up tables for each pair of particle type  $T$  and energy  $E$ .

Due to observing some discrepancies with in vitro experience, the LEM received a few updates in the last years [Elsaesser12, Friedrich13, Gruen12, Gillmann14]. There is still room for improvement of recent TPSs, in the context of clinical treatment for the validation of the newer models.

## 2.3 Monte Carlo particle transport simulations

### 2.3.1 Monte Carlo codes in clinical practice

In order to simulate particle transport in medium, MC methods are commonly used as a tool for validation in clinical practice. Built Physical models and a detailed ma-



terial description in the code guide the particles along their path through the patient. The most popular general purpose codes, are FLUKA [Ferrari05, Boehlen14], GEANT4 [Agostinelli03, Allison06], MCNPX [Waters02, Pelowitz11] and PHITS [Iwase02]. There exist more user-friendly macro codes, where complex experimental settings are easy to configure, such as GATE [Sarrut14, Jan11]. Guidelines for setting up independent Monte Carlo dose calculations for ion beam therapy facilities are presented in [Paganetti08] for proton therapy and in [Parodi12] for Carbon ion therapy.

### 2.3.2 MC techniques for dose calculation

The application of MC codes in ion beam therapy started to increase over the last decade. Among others, due to the need for accurate dose calculations in high dose gradients occurring in particle therapy. Currently, several inverse treatment planning systems are based on analytical pencil beam algorithms. Fast computation times, paired with acceptable accuracy, match the expectations for clinical needs in most cases. In some more complex treatments, the approximations in the pencil beam algorithms are an issue. To be highlighted are cases with large heterogeneities in the patient geometry. [Parodi07] In ion beam therapy, high treatment conformity dose distributions are more sensitive to organ movement, density variations and heterogeneity effects compared to conventional radiation therapy. MC codes can help to address one link in this interleaved chain, relevant for the correct and successful treatment delivery, by facilitating an increased accuracy in the dose and fluence computations in the patient. This may allow, for example, to decrease treatment margins for complex geometries, reducing the integral dose received by the patient as discussed by [Paganetti08]. Here we present a short list of the benefits of MC particle transport codes over analytical algorithms [Ferrari02]:

- include heterogeneities in the simulation setup
- are not approximating for the atomic composition of tissue (in comparison to the water-equivalent approach)
- can model the physical interactions with the state of the art physical models
- allow more freedom compared to analytical approaches

### 2.3.3 The Monte Carlo method

Different combinations of composition and rejection Monte Carlo methods are used in the Geant4 toolkit [Allison16] [Apostolakis09] [Agostinelli03]. To give an idea, only the fundamental formalism of these methods is outlined here. For a more detailed description, the interested reader is referred to these publications [Messel70] [Nelson85] [Butcher60]. To sample  $x$  from the distribution  $f(x)$ , in the interval  $[x_1, x_2]$ , the normalised probability density function is given as

$$f(x) = \sum_{i=1}^n N_i f_i(x) g_i(x) \quad (2.26)$$

where we assume  $N_i > 0$ .  $f_i(x)$  are normalised density functions on the interval  $[x_1, x_2]$  and  $0 \leq g_i(x) \leq 1$ .

With this method,  $x$  can be sampled as:

1. selecting a random integer  $i \in 1, 2, 3, \dots, n$  with proportionality to  $N_i$
2. selecting a value  $x_0$  from the distribution  $f_i(x)$
3. calculating  $g_i(x_0)$  and accept  $x = x_0$  with probability  $g_i(x_0)$
4. if  $x_0$  is rejected restart from step 1.

The mean number of tries to accept a value is given by  $\sum_i N_i$ . A good method of sampling from the distribution  $f(x)$  has the following properties:

- sub-distributions  $f_i(x)$  can be sampled easily
- rejection functions  $g_i(x)$  can be evaluated easily and quickly
- mean number of tries is not too large

Thus the different possible decompositions of distributions  $f(x)$  are not equivalent and this can be abused to optimize the decomposition to obtain less computation time.

### 2.3.4 Particle Transport

Condensed history algorithms are used to simulate transport in cumulative effects of multiple collisions approximated in a single "step" of the user defined path length. This step is the distance that each Monte Carlo particle travels between collisions. In Geant4, particle transport is a combination of the Geant4 stepping manager class, the physics processes and the transportation 'process', which identifies the next volume boundary in addition to the geometrical volume that lies behind it, when the track has reached it. The length of interaction is expected to occur determined by summing up all processes applicable at each step. Now the particles are determined and will remain within the current volume, or to cross into a different volume before the potential interaction occurs. The main contribution for the determination of the trajectory of charged particles, including the boundary crossing and effects of fields from the outside, are multiple scattering and the transportation process.

### True step length

Particle transport in Geant4 is performed step by step. The true step length for the next physics interaction is randomly sampled using the mean free path of the interaction or by given step limitations in the Geant4 code. The new true step length is always defined by the smallest step limit. To compute the mean free path length of a particle in media, GEANT4 uses the cross-section of a particular physics process and the density of the involved atoms. The number of atoms is given per volume as:

$$n = \frac{N_A \rho}{A}, \quad (2.27)$$

where  $N_A$  is the number of Avogadro,  $\rho$  describes the density of the medium and  $A$  is defined as the mass of a mole.

If the material is compound, built with different materials, the number of atoms per volume of the  $i^{th}$  element is

$$n_i = \frac{N_A \rho w_i}{A_i}. \quad (2.28)$$

with  $w_i$  being the proportion by mass of the  $i^{\text{th}}$  element and  $A_i$  is defined as the mass of a mole of the  $i^{\text{th}}$  element.

The interaction length  $\lambda$ , also known as the mean free path of a process, can be described in terms of the total cross section  $\Sigma$ :

$$\lambda(E) = \left( \sum_i [n_i \times \sigma(Z_i, E)] \right)^{-1} \quad (2.29)$$

and  $\sigma(Z, E)$  describes the total cross section per atom of the process and  $\sigma_i$  is the index over all elements of the compound material.

Part of the right side of the equation above  $\sum_i [n_i \times \sigma(Z_i, E)]$  is known as macroscopic cross section. To speed up simulations, cross sections per atom and mean free path values may be tabulated during initialization.

The mean free path  $\lambda$  cannot be used directly to sample the probability of interaction in a heterogeneous detector, due to the dependence on the medium. The mean free path of a particle is defined as

$$n_\lambda = \int_{x_1}^{x_2} \frac{d_x}{\lambda(x)}. \quad (2.30)$$

However, this number is not dependent on the material transversed, so we assume  $n_r$  is a random variable denoting the mean free path from a given point to the point of interaction, the distribution function of  $n_r$  is given as

$$P(n_r < n_\lambda) = 1 - e^{-n_\lambda} \quad (2.31)$$

To calculate the total mean free path, the particle travels before reaching the interaction point,  $n_\lambda$ , the equation

$$n'_\lambda = n_\lambda - \frac{\Delta x}{\lambda(x)}, \quad (2.32)$$

is used, which is sampled as  $n_\lambda = -\log(\eta)$  at the beginning of the trajectory.  $\eta$  is a random number uniformly distributed in the ranging from 0 to 1.  $n_\lambda$  is updated after each step  $\Delta$  until the step originating from  $s(x) = n_\lambda \times \lambda(x)$  is the shortest, which triggers the specific process.

## Step Limitations

The brief description of particle transport is known as the differential approach. This method imposes a limit on the step size, due to the energy dependence of different processes and particles. It is also assumed that the step length is chosen small enough so that the cross sections of particles remain approximately constant during one step. The disadvantage of using a small step size is the increase in computation time and also the default model of energy fluctuations will not be accurate for fine steps. Therefore, a good compromise between the required accuracy and computation speed of a detailed simulation is essential. To overcome this problem, the integral approach is used, where the cross sections are corrected for the varying energy.

## Transportation

The process of transportation regulates the geometrical limits of a step. Calculating the step length, a track will cross into another volume. If the track crosses the boundary, the transportation process registers the entrance of the next volume. When there is an electromagnetic field and a charged particle tries to propagate through it, the transportation process is responsible for the particle in this field, dependent on an equation of motion. This equation of motion can be provided for a case of an EM field but also for other sorts of fields. In general, it is described as

$$\frac{d\vec{p}}{ds} = \frac{1}{v}\vec{F} = \frac{q}{v}(\vec{E} + \vec{v} \times \vec{B}). \quad (2.33)$$

Propagation of the polarisation and gravitational field effects in case of slow neutral particles are taken into account by Geant4.

### 2.3.5 Hadronic physics models

Although there are many different multi-purpose MC codes, most of them follow a similar modeling scheme for the description of building the hadronic physics and subsequent reaction processes. The common approach to describe hadronic interactions is referred to as 'microscopic' approach, where a physical basis motivates every single step. Physical models in Geant4 as in FLUKA and other MC codes always aim to be validated, theory-driven and benchmarked with data at the single interaction level. For these predictions, the set of free parameters shall be fixed for all energies and target-projectile combinations. [Ferrari02] In general, the scheme for hadron-nucleus interactions in GEANT4 is described by the following stages which switch from initially dynamical to a statistical treatment:

- Glauber-Grigove cascade ( $>1$  GeV) and intra-nuclear cascade
- Pre-equilibrium stage
- Equilibrium de-excitation stage: evaporation, fission, Fermi break-up
- Radioactive decays

The hadronic physics in Geant4 are defined to cover the user specified reactions which can produce hadrons in its final state. Therefore it covers purely hadronic interactions, lepton- and gamma-induced nuclear reactions and radioactive decay. The Geant4 process starts with the cross sections to determine the interaction occurrence followed by a model describing the final state of the interaction. Cross sections are given in an energy range from sub-eV to TeV, depending on interaction and particle. Multiple models are available in specific energy ranges to provide alternative approaches for different applications. An overview of the given physical model topics is shown at the end of the chapter in table 2.2.

Geant4 is widely used in a variety of application domains, including high energy physics, nuclear physics, astrophysics, space engineering and medical physics. Some of these domains have a strong requirement of nucleus-nucleus interactions in their simulations. Geant4 provides the Binary Light Ion Reaction model and the Wilson Abrasion and Ablation model for those interactions. The Wilson Abrasion model is a simplified macroscopic model based largely on geometric arguments at the cost of accuracy. Nuclear ablation has been developed to provide a better approximation for the final nuclear fragment from an abrasion interaction.

However, the Binary Light Ion Reaction Model has a limitation for applicable nuclei and the prediction power of Wilson Abrasion and Ablation model does not always satisfy user requirements.

The demand for a native Geant4 model which supports all types of nuclei with better prediction power compared to the Binary Light Ion Reaction Model was increased and hence a new Quantum Molecular Dynamics (QMD) model was developed. For the description of the two most used physics lists, we follow [Koi08].

## Binary Light Ion Reaction Model in Geant4

The Binary Light Ion Reaction Model in Geant4 is an extension of the Binary Cascade model used for light ion reactions. Binary Cascade is a mix of the classical cascade code and the QMD description.[Folger04] The basic idea of the model follows a detailed description of a 3D nucleus. All participating particles will be transported into the nucleus, where the particles experience binary interaction with internal nucleons, therefore only two nuclei always interact. Each participating particle is treated as a Gaussian wave packet and the total wave function is assumed to be the direct product of the participants, thus each interaction is treated independently. The resulting equations of motion are then derived from the wave function and appear in the same structure as the classical Hamilton equations. The Hamiltonian is calculated from the simplified time-independent optical potential in the Binary Cascade model. The participating particles of the Binary Cascade are either a primary particle including nuclei in the projectile nucleus or are particles generated or scattered in the cascade and only the participating particles are propagated into the nucleus. This model is not recommended for heavy ion reactions, as interaction between the participants is neglected. The principle of Pauli checks the binary collisions of participating particles with the residual nucleus. Also, decay interactions of particles in resonance are included and the principle of Pauli applies to them as well. The particle participants are tracked until either a reaction, decay, escape or capture of the nucleus occurs. If the cascading calculation is done, the residual nucleus is investigated and passed to the low energy models implemented in Geant4 for additional particle emissions.

## Quantum Molecular Dynamics Model in Geant4

The extension of the classical molecular dynamics model is called quantum molecular dynamics (QMD) model.[Koi06] It is used to analyze a wide range of heavy ion reactions, in particular, many-body processes and the formation of complex

fragments. The major differences between QMD and Binary cascade are

1. in the definition of participating particles.

Nucleons in the target and projectile nucleus are considered as particles participating in the QMD model. Thus each nucleon has its wave function and the resulting total wave function is a direct product of each nucleons wave function.

2. in the potential term in the Hamiltonian.

The potential terms of the Hamiltonian are given as self-generating from the system configuration, they are calculated from the relationship between the particles in the system. This stands in contrast to Binary Cascade where the participant particles are tracked sequentially, while in QMD this happens simultaneously. This results in a dynamically changing potential with the time evolution of the system.

3. in the interactions of the participating particles.

There is no rule denying participating particles to interact with each other in QMD participant-participant scatterings are naturally included.

Thus QMD achieves a more detailed description of the nuclear reactions but with the cost of slower computing.

## Liège Intranuclear Cascade model

Unlike the other two models, INCL++ models the nucleons as a free Fermi gas in a static potential wall. The targets and projectiles which can be modeled by the INCL++ model are limited to a mass number of up to  $A = 18$ .

## Cross Section of Nucleus-Nucleus Interaction

Hadronic cross section interactions are not fundamentally implemented in any model. Although the models need the cross sectional data in order to model Nucleus-Nucleus (NN) interactions properly and decide where they will happen in the geometry of the simulation. There are different validated models which take care about cross sectional formalism in NN collisions [Kox87] [Shen89] [Sihver93] [Tripathi97] and [Tripathi99]. These are models which give empirical and parametrized formulae with theoretical insights and provide the reaction cross sections of a wide variety of projectile-target combinations. These cross sections also are a part of sampling the impact parameter in the QMD model.

### 2.3.6 Electromagnetic physics constructors

Electromagnetic physics constructors were first published in [Apostolakis09], were extended in [Ivanchenko11] and became stable in recent releases of Geant4 [Allison16]. The default electromagnetic physics is built by the G4EmStandardPhysics constructor. Internal tables for energy loss, range and cross sections are built from 100 eV to 100 TeV. These limits are defined based on LHC experiments requirements. Upper limits of applicability of various electromagnetic processes are more significant and are process dependent. For example, muon models are valid up to 1 PeV. To provide particle transport for all use-cases, the operational energy range goes down to zero, but below one keV the accuracy of the default set of models is degraded substantially. The Geant4 toolkit includes many alternative physics models, especially, for electromagnetic physics. There are several well-established configurations recommended for different applications. For electromagnetic interactions, EMZ Opt4 standard physics are recommended for ion beam therapy (ion and proton stopping uses the ICRU73 data and finer step limits). [GateUserGuide] The EM Opt4 physics list uses "standard" Geant4 electromagnetic physics as built by the G4EmStandardPhysics\_option4 constructor.



**Table 2.2: The Physics Reference Manual [GEANT4]** provides detailed explanations of the physics implemented in the Geant4 toolkit.

G4 Physics Reference Manual			
Particle Decay			
	<i>Decay</i>		
<b>Electromagnetic Interactions</b>	<i>Gamma incident</i>	<i>Energy loss of charged particles</i>	<i>Elastic scattering</i>
	<i>Electron and positron incident</i>	<i>Muon incident</i>	<i>Charged hadron incident</i>
		<i>Optical photons</i>	<i>X-Ray production</i>
			<i>Atomic relaxation</i>
			<i>Polarized electron/positron/ gamma incident</i>
<b>Hadronic Physics</b>	<i>Hadronic Cross Sections</i>	<i>Coherent elastic scattering</i>	<i>Hadron-nucleus Elastic Scattering at Medium and High Energy</i>
	<i>Fritiof (FTF) Model</i>	<i>Bertini Intranuclear Cascade Model</i>	<i>Binary Cascade Model</i>
	<i>Precompound model</i>	<i>Evaporation Model</i>	<i>Fission model</i>
	<i>Fermi Break-up Model</i>	<i>ABLA++ evaporation/ fission model</i>	<i>Quantum Molecular Dynamics for Heavy Ions</i>
	<i>Electromagnetic Dissociation Model</i>	<i>Interactions of Stopping Particles</i>	<i>Low Energy Neutron Interactions</i>
		<i>Low Energy Nuclear Data (LEND) Package</i>	<i>Radioactive Decay</i>
			<i>LowEnergyChargedParticles</i>
<b>Gamma- and Lepto-Nuclear Interactions</b>	<i>Cross sections in photonuclear and electronuclear reactions</i>	<i>Gamma-nuclear interactions</i>	<i>Electro-nuclear interactions</i>
			<i>Muon-nuclear interactions</i>
<b>Solid State Physics</b>		<i>Crystal channeling physics</i>	<i>Phonon-Lattice interactions</i>

# 3

## The Austrian ion beam therapy center: MedAustron

### 3.1 Introduction

The MedAustron (MA) Ion Beam Therapy Center, built in Wiener Neustadt (Austria), started to treat patients with protons in December 2016. The purpose of this facility is to treat cancer and to perform research in the field of particle therapy. It is a dual-particle therapy facility, where protons and Carbon ions are available for patient treatment. The first beam line with Carbon ions is operational since July 2019. Besides MedAustron, other treating dual-particle facilities in Europe are HIT in Heidelberg (Germany), MIT in Marburg (Germany) and CNAO in Pavia (Italy). The aim of this chapter is to give a technical overview on selected facility specific topics following two Ph.D. theses previously performed at MedAustron. [Carlino17] [Elia19]

### 3.2 Accelerators for LIBT

#### 3.2.1 Types of accelerators

The most common types of accelerators, which are needed to achieve the energy required in particle therapy, are synchrotrons or cyclotrons.

A cyclotron is a relatively cheap and compact alternative accelerator, compared to a synchrotron. It delivers a continuous beam with the characteristic of constant extraction energy paired with high intensity. Proton cyclotrons for therapy are available from industry, while no Carbon ion cyclotrons providing the required extraction energy have been constructed yet, mostly due to magnet size constraints. Because cyclotrons deliver a beam with fixed energy, passive systems need to slow down particles according to the tumor depth. With a cyclotron, you can always only deliver one type of particle while a synchrotron can accelerate different species of ions. Synchrotrons are more expensive, but also more sophisticated and have a wider range of possibilities. Synchrotron systems are also much larger than the cyclotron systems. In a synchrotron it is possible to actively change the energy of the particles without any additional passive elements.

The principle of a synchrotron is injecting the beam at relatively low energy and afterward accelerated it in the synchrotron ring to the extraction energy.

### 3.2.2 MedAustron Particle Therapy Accelerator (MAPTA)

The integrated medical system of the entire facility supplies a total of four irradiation rooms. One irradiation room (IR1) is devoted to non-clinical research where protons with an energy up to 800 MeV can be delivered while the other three rooms are dedicated to patient treatments (IR2-IR4). The layout of the MA ion therapy center can be seen in Figure 3.1. The goal is to deliver both particle types, proton and Carbon ions, in the irradiation rooms, except for IR4, as it is equipped with a unique gantry system, only suitable for proton treatment. In IR2 there is a vertical beam line as well as a horizontal beam line available while the IR3 is only supplied with a horizontal beam line.

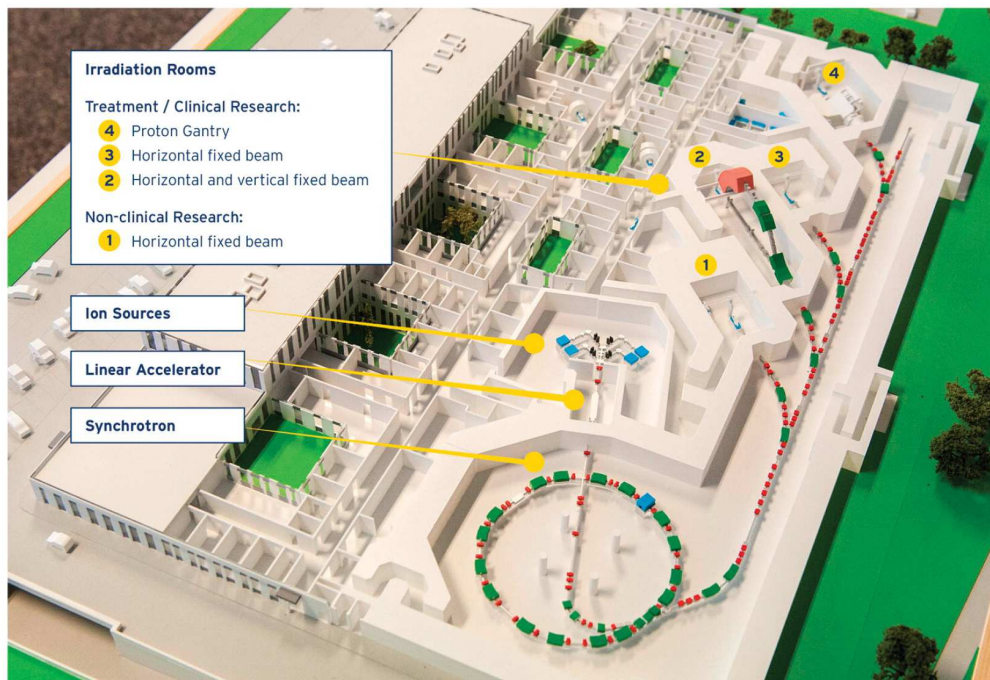


**Figure 3.1:** Layout of the MedAustron Ion Therapy center.

MedAustron, which was planned as multi-ion beam therapy center, has a synchrotron accelerator with the possibility to accelerate ions from protons up to neon ions. The clinical range of the facility for protons is in an energy range of 62.4 to 252.7 MeV (range in water from 3 to 38 cm) and for Carbon ions in a range of 120 to 402.8 MeV/u (range in water from 3 to 27 cm). The accelerator design is based on the machine installed at CNAO, following the PIMMS project from CERN. [PIMMS]

If we break it down to the basics, the beam transport line is a vacuum pipe system with a total length of around 400 m from the ion sources to the irradiation room. To maintain a pressure down to  $5 \times 10^{-9}$  mbar, more than 130 pumps are needed and to steer the beam, roughly about 300 magnets are installed. To characterize the beam (e.g., mean kinetic energy, energy spread, beam divergence and emittance), 153 monitors of 16 different species are used in the accelerator.

The beam is produced by one of the three sources and transported by the low energy

beam transport line (LEBT) to the LINAC. The radiofrequency quadrupole (RFQ) and an Interdigital-H(IH)-mode drift-tube are the main parts of the LINAC.

The quadrupole accelerates the particles to energies up to 400 keV/u and at the end of the LINAC, the injection energy into the synchrotron is about 7 MeV/u. Right after the LINAC, the particles  $C^{+4}$  or  $H_3^+$  are filtered by a thin Carbon foil and guided to the synchrotron by the medium energy beam transfer line (MEBT).

A degrader might be inserted to reduce the number of particles transported. Four different degrader settings are available, 100%, 50%, 20% and 10% transmission. In the synchrotron, particles are accelerated via oscillating high-frequent electromagnetic fields and accumulated coming from the LINAC. This process is performed in several cycles. The particles are captured and accelerated utilizing a radiofrequency (RF) cavity to the final energy required and after that, the particles are extracted from the synchrotron. They are guided to the high energy beam transport (HEBT), using a so-called slow extraction method, where the particle beams have a spill length from 1 to 10 s. For proton beams, we have a maximum extraction number of particles of  $2 * 10^{10}$  and for Carbon ions, this number is about  $4 * 10^8$ .

### 3.2.3 Active scanning beam delivery system at MedAustron

At MedAustron, an active scanning beam delivery system is used. In active beam scanning, the target volume is divided into layers with equal beam energy, where each layer is covered with a grid of spots. The purpose of the scanning beam system is to deliver the dose sequentially to each spot in an energy layer. This is achieved by deflecting the particles with a magnetic field. To reach the different layer depths, the particle energy is varied through the accelerator, resulting in a deeper or shallower Bragg peak of the particles. Active beam scanning is advantageous because no passive scattering techniques are needed as in cyclotron facilities, which decreases also the production of unwanted secondary particles. The main disadvantage is the complexity in relation to passive scattering techniques and the requirement on the stability and reproducibility of the beam position. Three different techniques are established worldwide:

- discrete scanning technique
- quasi-discrete scanning technique (installed at MedAustron)
- continuous scanning also known as raster scanning [ICRU78]

The first spot scanning system was developed at NIRS in Japan. [Kanai83] The first spot scanning gantry system was built at PSI in Switzerland. [Pedroni95] Spot scanning is used as a step-and-shoot technique. During discrete spot scanning, the beam is turned off between the spots, which avoids unwanted dose. First use of quasi discrete scanning was at the Gesellschaft für Schwerionenforschung (GSI, Germany) [Haberer93] and later adopted in Heidelberg (Germany) at HIT, Pavia (Italy) at CNAO and Wiener Neustadt (Austria) at MA. As already mentioned MA is using a synchrotron accelerator which allows dynamic variation of the ion beam energy. After the desired particle fluence is reached in one voxel, the beam is moved to the next voxel without turning the beam off.

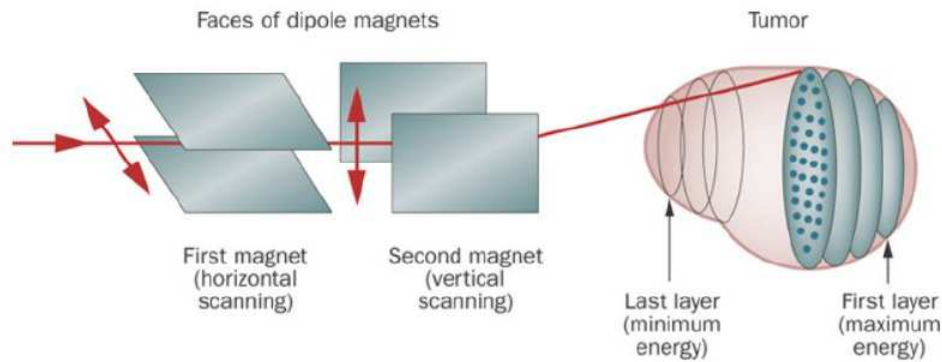


**Figure 3.2:** Illustration of the active beam scanning techniques.[Durante10]

Figure 3.2 illustrates the active scanning techniques, where the beam is moved in horizontal and vertical direction along an energy layer by fast scanning magnets. Raster scanning is a method where a beam of particles is scanned continuously across the cross-section of the beam in a raster pattern. The intensity is varied in this technique as a function of beam position by continuous control of the particle-beam intensity and/or the scanning speed. During the switch from one iso-energetic layer to another, the beam is turned off. The nozzle, which is part of the Beam Delivery System (BDS), serves as an online-treatment beam diagnosis tool to ensure patient safety. All four beam lines are equipped with two different independent dose-monitoring units, the Independent Termination System (ITS) and the Dose Delivery System (DDS). Latter is responsible for the beam monitoring and is observing different beam parameters such as beam spot size, beam position and the intensity. [Giordanengo15] The layout of the MedAustron treatment head is shown in Figure 3.3. The DDS is once again divided into two independent parts, Box1 and Box2. In case of an error, the magnetic chopper is activated and the beam is stopped. [Giordanengo13] We distinguish between two different passive elements at MedAustron, the Ripple Filter (RiFi), which is mostly polymethyl methacrylate (PMMA) with 2 mm thick triangular section slats and the Range Shifter (RaShi). The RiFi is used in exceptional proton treatment cases, but in general, it is more common to use two orthogonal RiFis for Carbon ions to increase the Bragg peak width, which speeds up the irradiation process. The other passive element, the RaShi, helps to pull back the Bragg Peak to the surface for superficial targets. The RaShi acts as an absorber as the minimum energy from the synchrotron would be still too deep for some superficial tumors.



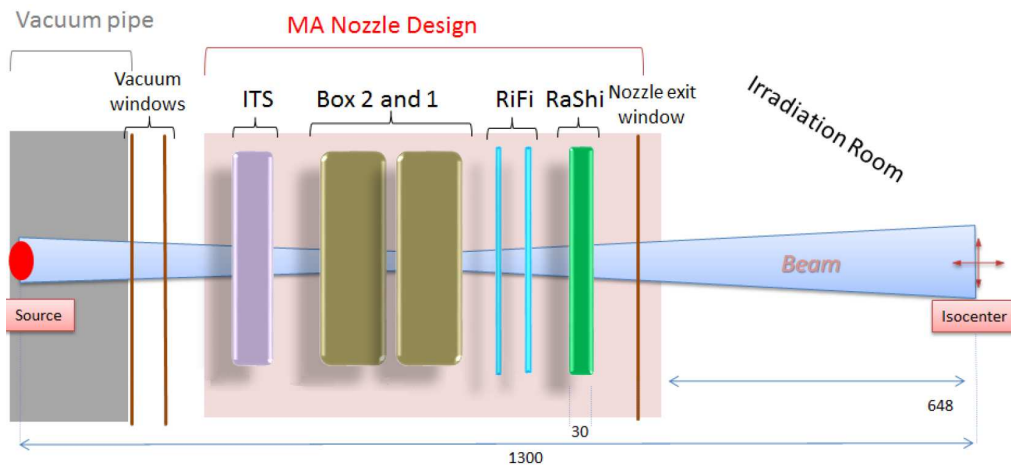


**Figure 3.3:** Layout of the MedAustron treatment head.  
Adapted from [Carlino17].

### 3.3 Treatment Planning System (TPS)

Treatment planning is a process to design a patient specific treatment, where we aim to optimize the relation of maximal coverage of dose to the target and sparing the surrounding normal tissues.

The TPS RayStation (RS v8.1), developed by RaySearch Laboratories (Stockholm, Sweden), is installed at MA. The software allows optimizing spot weights and the scanning pattern for the quasi-discrete active scanning implemented at MedAustron. For dose calculation, two algorithms are used, pencil beam and Monte Carlo engine. The MC dose engine system is not available for Carbon ions in the current version of RS. Ions heavier than protons are mainly different in the higher variability of the RBE, which demands the use of appropriate biophysical models. In this thesis we focus on the description of Carbon ions dose calculation. In the current version of RS, the pencil beam algorithm is responsible for the physical dose computation for Carbon ions which we describe in the next two sections following the manual of RayStation [RSMAN]. Multiple biological models are available in RS but currently only LEM I (Section 2.2.2) is in clinical use.

#### 3.3.1 Carbon pencil beam dose algorithm

The basis of the Carbon dose and RBE-weighted dose calculation is the so called pencil beam dose algorithm. The algorithm associates each pencil beam with a physical pencil beam (also referred to as scanning spot), delivered by the pencil beam scanning (PBS) system. Each of these pencil beams contributes to the final dose, where each contribution is calculated by performing a factorization of the dose to longitudinal, integrated radial profiles as function of depth  $IRPD$  and the lateral, dose profile  $\Phi$  components:

$$dose(z, r) = \Phi(z, r)IRPD(z) \quad (3.1)$$

where  $r$  is the radial distance from the dose voxel and  $z$  is the radiological depth of the dose voxel computed by ray tracing from the beam source point to the pencil beam center line in the Carbon pencil beam dose computation.

This factorization only remains valid within the so-called infinite slab approximation, which assumes that each pencil beam experiences the patient geometry as number of semi-infinite layers, extended transversely to the central beam axes. Due to this approximation the pencil beam shapes have radial symmetry. The phase space parameters of each pencil beam are transported along the central axis through the patient during dose computation. The algorithm computes the physical dose in terms of absorbed dose to water. The pencil beam algorithm has been used in the past for several dose algorithms [Parodi12] [InaniwaKanematsu15].

The scaling of the integrated radial profiles as a function of depth captures the effect of longitudinal heterogeneities encountered in one dimensional ray tracing through the patient, although lateral heterogeneities also have to be taken into account in the dose calculation. Carbon ions experience less scattering, therefore only a single pencil beam per spot is used in the RayStation Carbon dose calculation. In order to still take the lateral heterogeneities into account, the radiological depth of each voxel is used whenever a quantity is depending on the radiological depth, such as the IRPD.

### 3.3.2 Calculation of the IRPD and particle energy spectra in water

To calculate the IRPD or the particle energy spectra in water, input data pre-generated by RaySearch or input data provided by the clinic is used. If we use the pre-generated input data, the data from RaySearch is weighted with the effective energy spectrum  $\frac{dN(E_i)}{dE}$  of the beam model, while clinical data is directly used without weighting. In the case of using the pre-generated data by RaySearch, the integrated radial profile as a function of depth is determined from the effective energy spectra  $\frac{dN(E_i)}{dE}|_{E_N}$ , by superposition of pre-calculated mono-energetic IRPDs following

$$IRPD^w(z, E_N) = \sum_i \frac{dN(E_i)}{dE}|_{E_N} irpd_i(z) \Delta E_i \quad (3.2)$$

where  $\Delta E_i$  is width of a bin and  $irpd_i$  is the pre-calculated integrated radial profile as a function of depth in water for the primary energy  $E_i$ , in units of  $\frac{\text{cGy cm}^2}{\text{ion}}$ .

### 3.3.3 Carbon ion dose calculation input data

To perform Carbon ion dose calculation the following ingredients are needed:

- integrated radial profiles as a function of depth
- differential particle energy spectra of primary Carbon ions and fragments (see also Chapter 5)
- nuclear halo model parameters

For more details about the Carbon ion dose calculation in RayStation we refer to [RSMAN].



### 3.3.4 Usage of GATE at MedAustron

Geant4 Application for Emission Tomography (GATE) is a software tool which offers a set of scripted commands eases the access to the powerful Geant4. The international OpenGate collaboration provides and develops this completely open source software project. GATE is a potential candidate for an independent dose calculation tool, as presented in a previous Ph.D. project [Grevillot11] and offers a large number of application possibilities [Sarrut14].

Specific characterization of the physical properties of a pencil beam model and full geometrical implementation of the treatment head are advantageous inclusions in the simulation setup for accurate dose calculation. These aspects are a crucial part of the presented works context and will be discussed in detail in Chapter 4. The aim of every facility should be a well benchmarked independent MC system to reduce the number of measurements acquired for commissioning.

# 4

## Beam modeling of the scanned Carbon ion beam line in GATE/Geant4

### 4.1 Introduction

In GATE a physic list builder mechanism is used to select a set of physics lists. Physics lists are the underlying basis of GATE for the description of physical interactions and processes (electromagnetic, hadronic, ...) using the Geant4 toolkit. The physics list sets are provided for typical use cases in a range of applications by the Geant4 community. Due to this wide range, it was essential to find a reliable set of physics lists for this project which allows accurate modeling of the nuclear fragments for clinical ion beams, which was needed for the simulation of the particle energy spectra. In literature, there is no clear guidance, which physics lists should be applied for Carbon ion simulations in radiotherapy. Therefore, to investigate the accuracy of three different nuclear fragmentation models in GATE/Geant4, we have benchmarked the physics builders *QGSP\_BIC\_HP* (BIC), *Shielding* (QMD) and *QGSP\_INCLXX* (Intra-Nuclear Cascade Liege). The nuclear model QMD is recommended by [Boehlen10, Bolst17] for Geant4 version 9.3 for applications with ions heavier than alpha particles, so-called 'generic ions'.

There are different methods for pencil beam modeling proposed, depending on the type of beam line and characteristics of the used MC code. At MA, an active scanning system is used and to accurately simulate the pencil beam, the pencil beam optics need to be characterized. In order to compare the physics builder, a preliminary Carbon beam model of the MedAustron Horizontal Beam Line (HBL), based on experimental data from the fixed Carbon beam line of the irradiation room 2 and a nominal spot size coming from the accelerator, was created.

The correlation between Carbon position and angular spread cannot be neglected, therefore we included a full model of the nozzle in our simulations.

We call the characterization of the required beam parameters, such as spot size, beam energy and energy distribution, beam modeling. To characterize the energy, integrated radial profiles as a function of depth were measured, as well as lateral beam profiles in air at different positions, to characterize beam spread. Simulation without the nozzle geometry allows empirical modeling of the pencil beam with a reward in computational time [Grevillot11, Grassberger14, Fracchiolla15]. Although, this approach requires additional corrections [Soukup05, Schwaab11] to

account for large-angle single scattered primary and secondary particles produced in the nozzle components [Pedroni05, Sawakuchi10, Grassberger14]. A dose comparison at the nozzle entrance and the nozzle exit to predict the dose generated from the secondaries can be found in Figure 4.1. [Elia19] In the graph, modeling at different positions is shown. At the nozzle entrance, the nozzle exit and the phantom surface. Starting to model after the nozzle exit leads to a Gaussian behavior for the lateral dose distribution, while modeling the source from the nozzle entrance results in a distortion in the Gaussian dose distribution, coming mostly from the large single scattering events while transmitting the nozzle, characterizing the outer envelope of the core, the so-called nuclear halo.

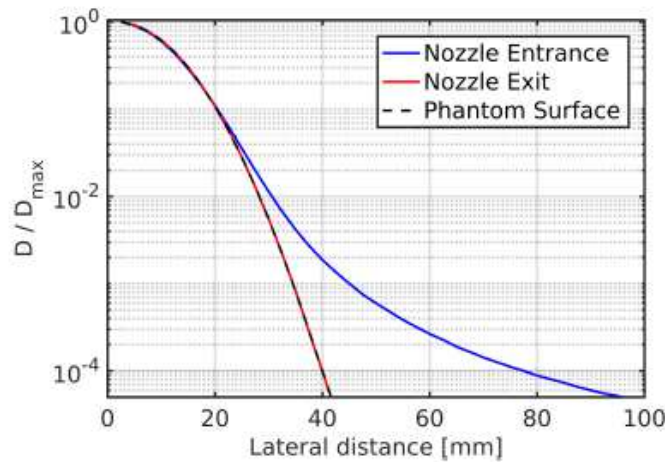


**Figure 4.1:** The lateral dose distribution of a 62.4 MeV proton beam with the source being at three different positions. Phantom surface, nozzle exit and nozzle entrance were investigated. The comparison between nozzle entrance and nozzle exit allows the prediction of the dose produced by secondaries due to the nuclear inelastic scattering which the primary ions experience along their path in the nozzle. The graph was adopted from [Elia19].

## 4.2 Materials and Methods

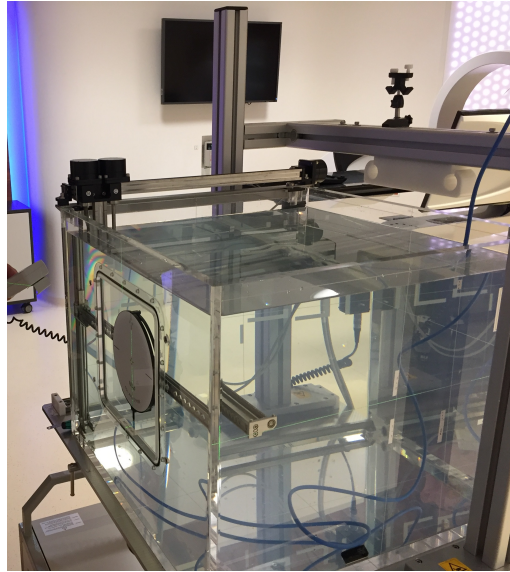
### 4.2.1 Measurements

#### Measuring devices

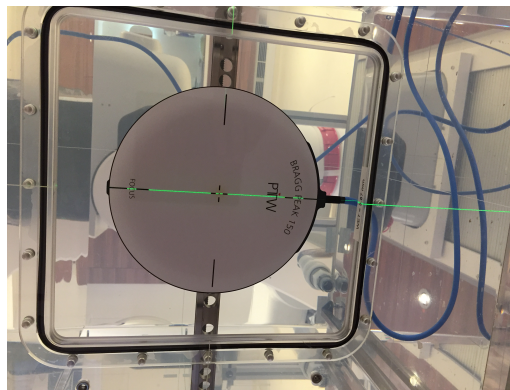
MP3-P (L) is the standard 3D computerized water scanning system from PTW for particle therapy and measuring transverse and depth-dose profiles in water with a resolution of as little as 0.1 mm.

The plane-parallel ionization chambers used at MA are the Bragg Peak (BP) and Roos-type (PPIC) for relative and reference dosimetry purposes. For acquiring depth-dose profiles, the BP chamber type 34070 ( $\varnothing$  81.6 mm sensitive diameter, 2 mm of measuring air gap and a 4 mm PMMA entrance window to prevent deformation in water) is a waterproof ionization chamber used for measuring IDD profiles in

the MP3 water phantom systems in combination with a BP type 34080 as a monitor chamber, with similar diameter but thinner entrance window. An alternative is the BP type 34073 ( $\varnothing$  39.6 mm sensitive diameter and 2 mm plate separation), but its diameter is reduced and therefore less suitable to measure laterally-integrated depth-dose profiles. Nevertheless, such a detector has interesting features complementary to the BP type 34080, for instance, in the validation of nuclear models by comparing integrated radial profiles as function of depth measured with different chamber diameters. [Grevillot18]



(a) Measurement setup



(b) BPC in the beam's eye view

**Figure 4.2:** Experimental setup for the integrated radial profiles as a function of depth. (a) full setup for measurements with the biggest BPC chamber (radius = 73.5 mm) and the 3D water tank and (b) direct shot of the PTW BP 150 the setup for measurements with the Bragg peak chamber Bragg Peak 150. Adapted from [Carlino17].

## Measurement procedure

The measurements presented in this work were carried out at the Horizontal Beam Line in Irradiation Room 2 (IR2HBL). Measurements of integrated radial profiles as a function of depth were carried out at four energies (121 MeV/u, 262 MeV/u, 327 MeV/u and 400 MeV/u) in order to cover the whole clinical energy range. The entrance surface of the water phantom was placed at ISD0 ("ISD" defines the distance between the isocenter and the phantom/patient surface. It is defined as surfaces upstream of the isocenter count as positive values and surfaces downstream of the isocenter as negative values. We do speak of isocentric treatment when the patient surface is aligned at the room isocenter (ISD = 0 cm)). Using the commercially available plane parallel ionization chambers for the measurements of the integrated radial profile as a function of depth is afflicted by the need for correction of the systematic offset due to their finite size. The dose components for a Carbon ion pencil beam in water is divided in three parts. The core, the halo and the aura, described in detail in [Gottschalk15]. Due to the limited radius of the chambers, some dose of the halo and aura (low-dose envelope) may not be accounted for. [Sawakuchi10a, Sawakuchi10b] In practice, MC simulations are used to evaluate the dose which is not captured by the detectors. The simulations serve to calculate the so-called correction factors, applied to the measured IRPDs of the BPCs of the different sizes. Three types of Bragg peak chambers (PTW Freiburg) have been used, the chamber radial sizes were 73.5 mm, 40.8 mm and 19.8 mm as partially shown in Figure 4.4. An overview of the experimental setup can be found in Figure 4.2 and a visualization of the beam diameter, as well as the different chambers, can be seen in Figure 4.3.

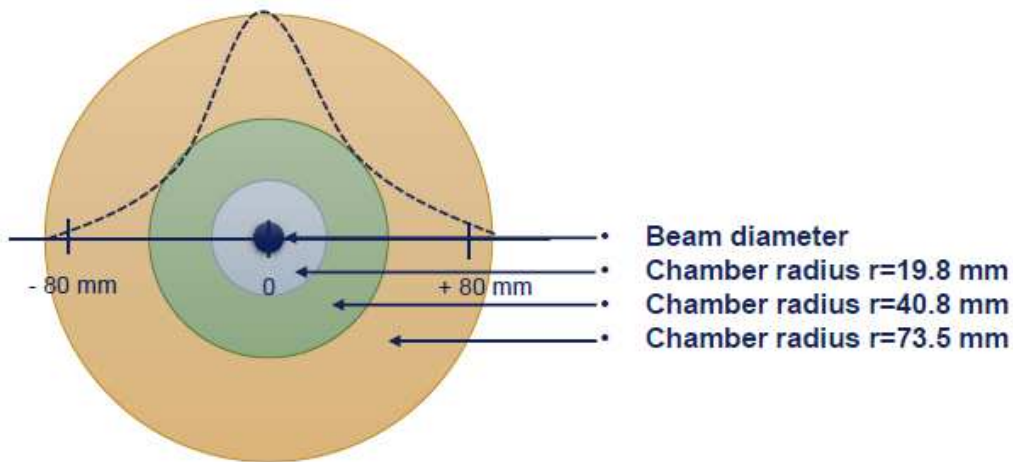


**Figure 4.3:** Visualization of the beam diameter and the different Bragg peak chambers used. ( $r=73.5, 40.8, 19.8$  mm) [Grevillot18]



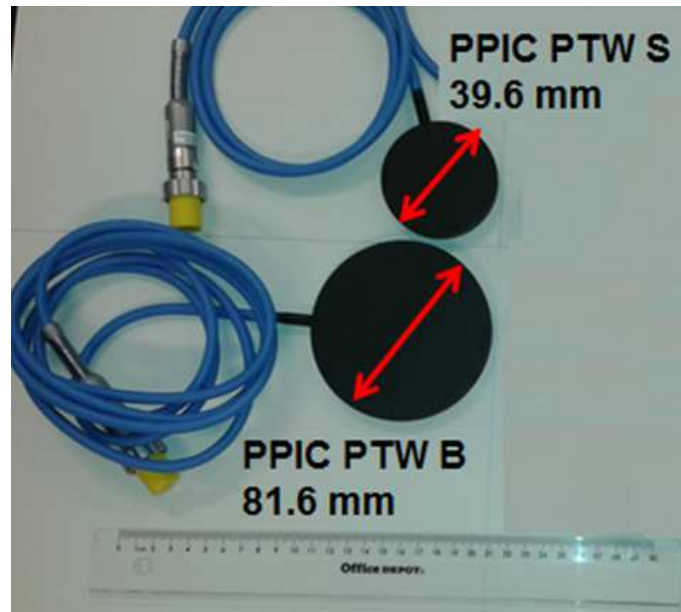


**Figure 4.4:** Two of the three different Bragg peak chambers used ( $r=40.8$ ,  $19.8$  mm). [Carlino17]

#### 4.2.2 Pencil beam characteristics and beam modeling procedure

The energy and optical properties characterize a pencil beams transversal and longitudinal profiles. The energy spectrum is considered Gaussian, with a mean energy  $E_0$  and energy spread  $\sigma_E$  (standard deviation). Optical properties are independent of energy properties. The following three parameters describe optical properties in the x and y directions (+z being the default direction of the beam): [Grevillot11]

- spatial beam spread distribution (beam or spot size)  $\sigma_x$  in x and  $\sigma_y$  in y
- angular spread distribution (beam divergence)  $\sigma_\theta$  in x and  $\sigma_\phi$  in y
- beam emittance (beam size and divergence phase space area)  $\epsilon_{x,\theta}$  in x and  $\epsilon_{y,\phi}$  in y.

To simulate the beam, specified MedAustron beam optic parameters were inserted in the GATE code as an initial guess provided by the therapy accelerator team. These parameters were the expected ones at the source position SAD=1300 mm upstream to isocenter to reproduce 2 mm of spot size in terms of FWHM at isocenter in vacuum. However, these optical parameters needed to be tuned to match the measured values in air at the isocenter and at different air gaps. For energy tuning, two parameters must be adjusted: the mean energy and the energy spread. The nominal particle energy has a direct correlation to the particles range in water. The energy spread has a direct correlation to the Bragg peak width and peak-to-plateau ratio of the particles dose deposition behavior. The tuning of these two parameters is an iterative process, where the user must determine the mean energy and energy spread which best reproduce the measured depth-dose profiles in water for this beamline. We have performed the tuning in the following order: [BeamLineModeling17]

1. adjust the mean energy until the range difference between simulation and measurement is within user tolerance. We evaluated the physical range determined

at the 80% dose level.

2. adjust the energy spread until the Bragg peak width and peak-to-plateau ratio differences between simulation and measurement are within user tolerances.

Energy tuning to match range and Bragg peak width has been conducted for one physics list QMD. Additionally, two other physics-builders have been compared but not tuned, as described in the later Section 4.2.4. (BIC and INCL++) The main influences of shape and characteristics of the pencil beam are influenced by the transport system and accelerator. To described properties of the pencil beam, a phase space diagram is used. An ellipse describes the momentum and position distributions of the beam particles. The spatial and angular beam spread distributions are Gaussian and correlated. Three different parameters characterize the ellipse in the phase space: divergence, beam width and emittance.

### 4.2.3 Monte Carlo simulations

The MC simulations were performed with GATE v8.1 [Jan11], built with Geant4 10.03.p03 [Grevillot11], using the electromagnetic package 'EMZ Opt4', combined with the pre-compound model for non-elastic hadronic interactions and the physics list *Shielding* (QMD). The production cut was set to 1 mm, as we did not produce secondaries with a range of less than 1 mm, so we decided not to track them once their residual range was lower than 1 mm. The main water box we simulated with a surface of  $50 \times 50 \text{ cm}^2$  and 40 cm in depth consisting of *G4\_WATER*, was positioned at the center of the simulation environment 'world' made of air. For the comparison of the different physics builder we did change the used physics lists to '*QGSP\_BIC\_HP* (BIC) and *QGSP\_INCLXX* (INCL++)'. The IRPDs were scored using the dose actor attached to different sub-cylinder geometries with the same dimensions as the actual Bragg peak chambers used in the measurements ( $r=73.5, 40.8$  and  $19.8 \text{ mm}$ ). The total number of primaries used in these simulations was set to  $10^4$ . As recommended by different authors for  $^{12}\text{C}$  [Luehr12, Boehlen12, Resch19], the ionization potential of water was set to 78 eV. Given the flexibility of GATE/Geant4, the components of the MedAustron specific treatment head were included using the blueprints.

### 4.2.4 Physics builder selection

A sensitivity study was performed with three different nuclear models. The Binary Intranuclear Cascade (BIC), the Quantum Molecular Dynamics (QMD) and the Liège Intranuclear Cascade (INCL++).



## 4.3 Results

### 4.3.1 Measurements

Measurements were performed at MedAustron, the IRPDs of the different ionization chambers of varying radius can be found in Figure 4.5. We saw the larger sized Bragg peak chamber captured more dose than the smaller chamber, as expected. In the dose entrance region, we saw about 14% more dose in the bigger chamber than in the smaller and this difference raised up to a deviation of about 34% in the Bragg peak.

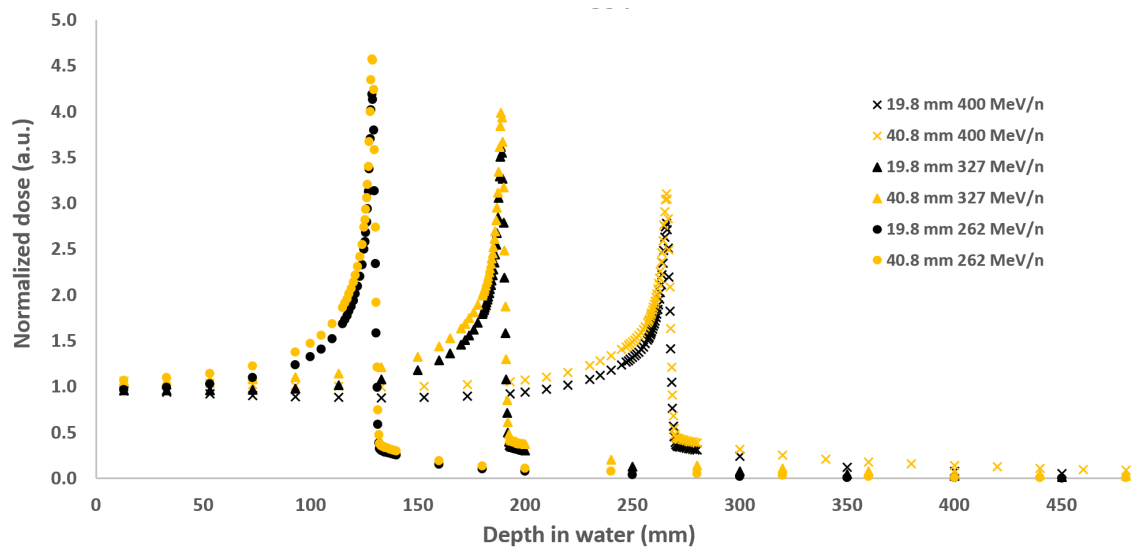


**Figure 4.5:** Integrated radial profiles as a function of depth normalized to the entrance. Measured for the different chambers at three different energies (400, 327 and 262 MeV/n). The different chamber sizes are displayed as the yellow line which corresponds to the medium-sized chamber ( $r = 40.8$  mm) and the black line which corresponds to the small chamber ( $r = 19.8$  mm).

### 4.3.2 Beam modeling

Beam modeling for a preliminary Carbon beam line in GATE was performed for 4 different pristine Bragg peaks. The settings of the beam tuning are shown in Table 4.1. An example of the tuned beams is presented in the Figures 4.6 and 4.7. The results for the beam tuning for one Bragg peak chamber of the four different energies can be found in Table 4.2. Overall, the beam tuning results showed less than 7 % deviation in the Bragg peak width for the highest energies and differ less than 0.2 % of the R80.

**Table 4.1:** Beam tuning settings.

Nominal Energy [MeV/u]	Tuned Energy [MeV/u]	Tuned Energy Spread [MeV/u]
121.0	120.0	0.9
262.0	259.5	0.4
327.0	324.0	0.6
400.0	397.5	0.9

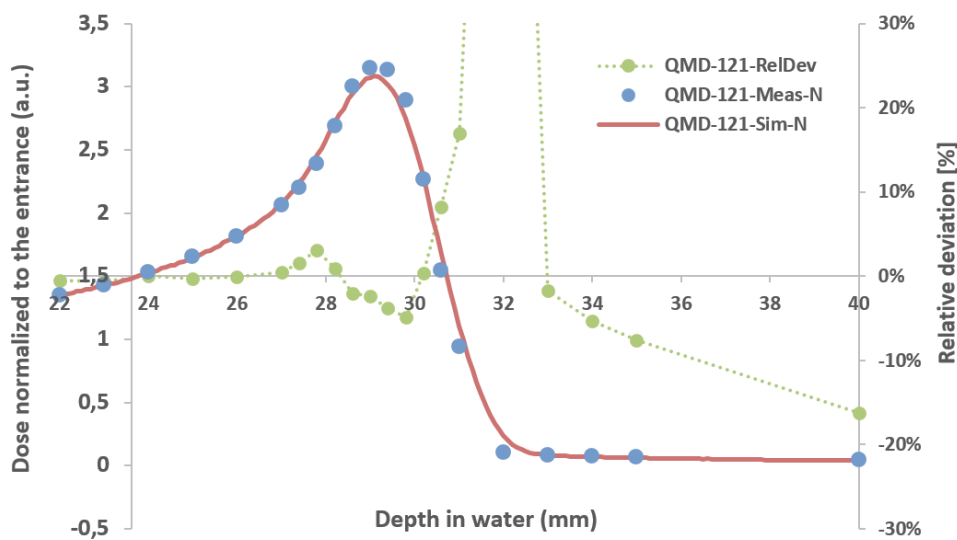


**Figure 4.6:** Bragg peak width and R80 comparison for the medium-sized Bragg peak chamber with the integrated radial profile as a function of depth at an energy of 121 MeV/u. The dashed-dotted green line shows the relative deviation of the blue dotted measured IRPD and the solid red simulated IRPD.

#### 4. Beam modeling of the scanned Carbon ion beam line in GATE/Geant4

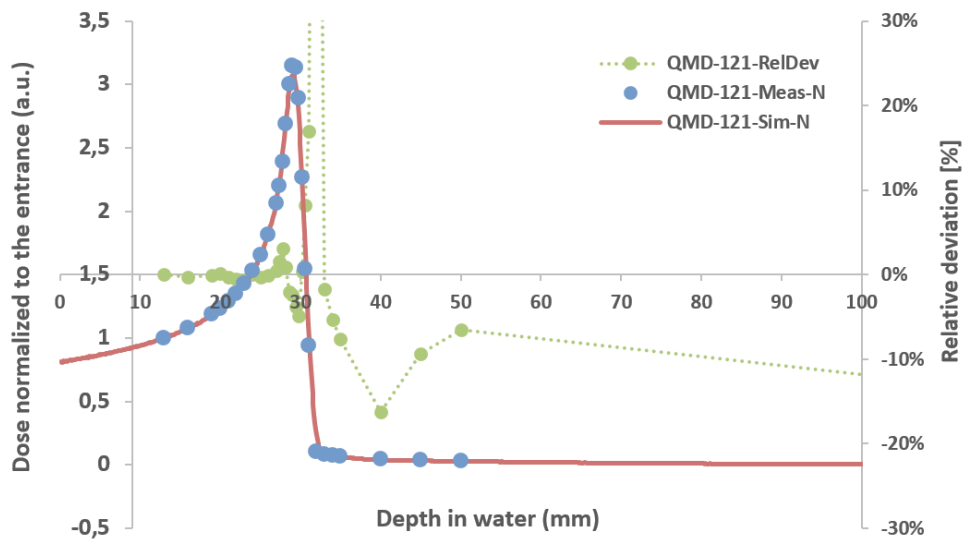


**Figure 4.7:** Plateau and tail tuning for the medium-sized Bragg peak chamber with the integrated radial profile as a function of depth at an energy of 121 MeV/u. The dashed-dotted green line shows the relative deviation of the blue dotted measured IRPD and the solid red simulated IRPD.

**Table 4.2:** Beam tuning results summary.

(a) Range 80 and Bragg peak widths of simulated data. Values of the medium sized Bragg peak chamber with  $r=40.8$  mm of four different energies are presented. 121 MeV/u beam in red.

R4-S	Dose80 (a.u)	Range80 (mm)	Range80L (mm)	BPW80M (mm)
400 MeV/u	2.34	267.0	263.6	3.4
327 MeV/u	3.02	190.0	187.3	2.7
262 MeV/u	3.48	129.8	127.4	2.3
121 MeV/u	2.47	30.1	27.9	2.2

(b) Range 80 and Bragg peak widths of measured data. Values of the medium sized Bragg peak chamber with  $r=40.8$  mm of four different energies are presented. 121 MeV/u beam in red.

R4-M	Dose80 (a.u)	Range80 (mm)	Range80L (mm)	BPW80M (mm)
400 MeV/u	2.35	267.0	263.8	3.2
327 MeV/u	3.01	190.0	187.4	2.6
262 MeV/u	3.44	129.7	127.4	2.3
121 MeV/u	2.53	30.0	27.9	2.1

(c) Relative deviations of Bragg peak width and Range 80 of measured data vs simulated in absolute and percentage values. 121 MeV/u beam in red.

Relative Dev.	BPWdelta_abs (mm)	BPWdelta_rel	R80delta_abs (mm)	R80delta_rel
400 MeV/u	-0.20	-6.1%	0.00	0.0%
327 MeV/u	-0.10	-3.7%	0.00	0.0%
262 MeV/u	-0.05	-2.3%	0.10	0.1%
121 MeV/u	-0.05	-2.4%	0.05	0.2%

### 4.3.3 Impact of different physic lists on the IRPDs

The simulated IRPDs for all the physics builders were in a good agreement with the measured data shown in the Figures 4.8 and 4.9. For a Carbon ion beam at 400 MeV/u at a range in water of 173 mm corresponding to a position in the entrance region QMD overestimated the dose by 0.86%, INCL++ did so by 1.44% and BIC overestimated by 3.57% compared to the measurements. At the position 266.2 mm in water, which corresponds to a position within the Bragg peak width 80, BIC overestimated the dose by 0.14%, QMD underestimated the dose by  $-1.18\%$  and INCL++ underestimated the dose by  $-2.89\%$ . In the fragmentation tail at a depth in water of 277 mm, INCL++ showed a dose underestimation of  $-6.83\%$ , BIC showed a dose overestimation of 7.35% and QMD showed a dose underestimation of  $-7.71\%$ . The IRPDs created by the nuclear model BIC have shown slightly better agreement with measurements than QMD whereas QMD did match to a small degree better than INCL++. Overall the three physic builders were found in agreement close to the Bragg peak with less than 5% deviation from the measurements and a deviation of less than 10% in the plateau region and up to 20% deviation in the fragmentation tail. Similar behavior was found for the other chambers and energies as well (not presented here). Our final choice of physics list was the *Shielding\_EMZ* (QMD) physics builder because the agreement with the measured data was very similar for the nuclear models BIC and QMD in our results and although BIC won the race in terms of computation speed we decided against it. The reason for this decision was because we found non-physical behavior for the results produced by the BIC nuclear model. At high energies, a bump occurred, visible in Figure 4.9 at the solid red line before the Bragg peak, which is likely connected to an error in C11 production and transport, according to the Geant4 community. Also, important to take into account when selecting a physics builder are the different computation times, as computation power is often limited. A comparison of the different computation times can be seen in Table 4.3.

**Table 4.3:** Computation times on one core.  $10^4$  particles were simulated comparing the different physics builder. INCL++ was the fastest and QMD the slowest. Absolute time differences and relative differences compared to QMD are displayed.

Computation times for					
$10^5$ particles	121 MeV/u	185 MeV/u	262 MeV/u	327 MeV/u	400 MeV/u
QMD	03:54 h	03:04 h	03:10 h	04:03 h	04:32 h
BIC	02:58 h	02:33 h	02:22 h	02:45 h	03:24 h
abs diff (QMD std)	00:55 h	00:31 h	00:47 h	01:17 h	01:08 h
rel diff (QMD std)	24%	17%	25%	32%	25%
INCL++	03:38 h	02:56 h	03:22 h	03:51 h	05:20 h
abs diff (QMD std)	00:15 h	00:07 h	00:12 h	00:11 h	00:47 h
rel diff (QMD std)	7%	4%	6%	5%	17%

#### 4. Beam modeling of the scanned Carbon ion beam line in GATE/Geant4

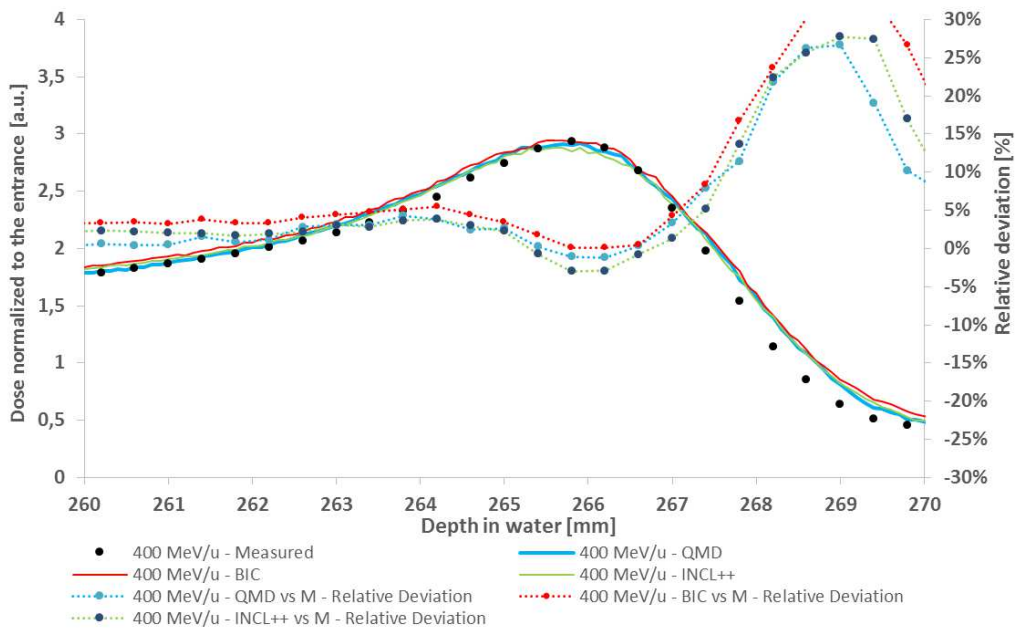


**Figure 4.8:** Comparison of the integrated radial profiles as a function of depth using different nuclear models in GATE/Geant4. The solid red line shows the result from the nuclear model BIC, the solid green shows the result from the INCL++ model, the solid blue line shows the result of the QMD model and black dots is the measured dose. The dashed lines represent the relative deviation of the different respective nuclear models compared to the measured data.

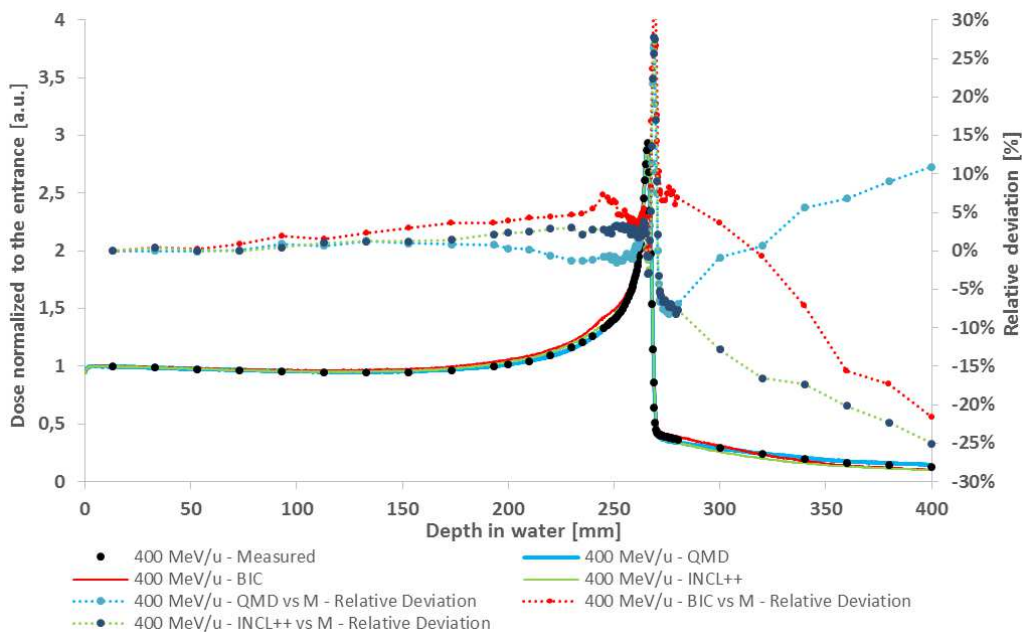


**Figure 4.9:** Comparison of the integrated radial profiles as a function of depth using different nuclear models in GATE/Geant4. Plot lines have the same properties as in Figure 4.8. The plot shows the full range of the IRPD.

## 4.4 Conclusion

When creating reliable fragment particle energy spectra to calculate the RBE-weighted dose, it is crucial to find an MC physics builder which is trustworthy.

For the process of finding the right candidate, it was necessary to perform preliminary beam modeling for the beam model at the fixed Carbon beam line in irradiation room 2 at the therapeutic energy range (120 MeV/u to 402.8 MeV/u). For this purpose measurements have been carried out at MA in the IR2 at four different energies with three different sized Bragg peak chambers ( $r=19.8$  mm, 40.8 mm and 73.5 mm) in a 3D computerized water scanner ('MP3-PL').

These measurements served as a foundation for the beam tuning, which was done with the physics builder '*Shielding\_EMZ*' (QMD). Optical properties of the beam model were given by the therapy accelerator team and were set constant to reproduce a spot size of 2 mm in terms of FWHM at isocenter in vacuum during the process of beam modeling. In the tuning, we achieved a maximum deviation of less than 7% at the highest energy in the Bragg peak width and a difference in the Range80 at the lowest energy of less than 0.5% for the medium-sized Bragg peak chamber.

We have used the beam model, tuned at four different energies, for a comparison of the selected different physics builder *QGSP\_BIC\_HP* (BIC), *Shielding* (QMD) and *QGSP\_INCLXX* (INCL++). The results show that the nuclear model BIC had the best overall match with the measurements, INCL++ was the fastest and QMD was the slowest but also the most reliable which is desirable in the clinical environment. The agreement of the nuclear models BIC and QMD was similar but we found unphysical behavior in the IRPD using the BIC nuclear model so we decided for the builder '*Shielding\_EMZ*' (QMD).

The results of this physics builder sensitivity study are in accordance with previous studies. [Luehr12] [Boehlen10] Based on our results and the agreement with selected literature we use '*Shielding\_EMZ*' (QMD) as the physics builder of our choice for the simulations in the following Chapter 5, which is the creation of the particle energy spectra.

# 5

## Particle energy spectra in GATE/Geant4

### 5.1 Introduction

Nuclear fragmentation affects the dose distribution, especially noticeable in the fragmentation tail. Thus, it is important to accurately model the particles in the mixed radiation field. The RBE plays an important role for particles in the mixed radiation field. It depends among others on the charge of an ion, its energy and the dose. [Luehr12]

In contrast to proton beams, accurate modeling of the production and transport of secondaries in Carbon ion beam therapy plays a bigger role, as Carbon ions experience a larger amount of fragmentation along their stopping path with the result of differently charged fragments, which contribute to the fluences and the delivered dose. In the target volume the dose from these fragments is in the order of some tens of percent [Matsufuji03] and in the tail, after the target the total dose is produced by the secondary particles. Besides effortful measurements, we rely on MC simulations for accurate predictions of these fragment fluences.

The term particle energy spectra refers to the distribution of primary ions and produced fragments differential in energy. Particle energy spectra are used to characterize the mixed radiation field at a certain depth in a Carbon ion beam and are essential in the RBE-weighted dose computation.

In this chapter, we do present the creation of the particle energy spectra in GATE/Geant4 using the physics builder *Shielding\_EMZ(QMD)*. A more sophisticated beam model has been created at MA. [Fuchs19] This beam model was in comparison to the preliminary beam model, which we created in the previous chapter, also optically tuned. Consequently, with the mature beam model paired with a reliable physics builder, we could start simulating the energy spectra needed for the beam model in the TPS. In Figure 5.1 the workflow of the "MA-GATE"-TPS beam modeling procedure is shown, starting from acquiring basic beam data till the final beam model in the treatment planning system.



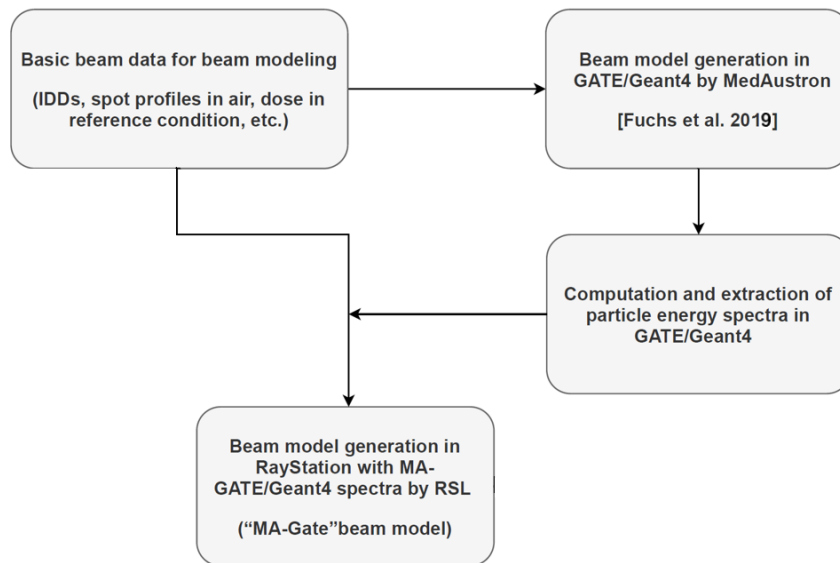


**Figure 5.1:** Workflow of the TPS beam modeling procedure.

The most influential parameters on the particle energy spectra appear to be the physical models and numerical settings in the different MC codes, the different modeling of charge changing cross sections and beamline specific modeling (e.g., inclusion of the nozzle). [Boehlen10]

To compare the different physics models, implemented at MedAustron using GATE/Geant4 and at RaySearch Laboratories (RSL, Stockholm-Sweden) using FLUKA to simulate particle energy spectra, the same simulation settings were pursued. All evaluations are using identical beam conditions, geometries (where it was possible) and material properties. The simulation settings used for the two different MC codes are described in Section 5.2.3 and 5.2.2.

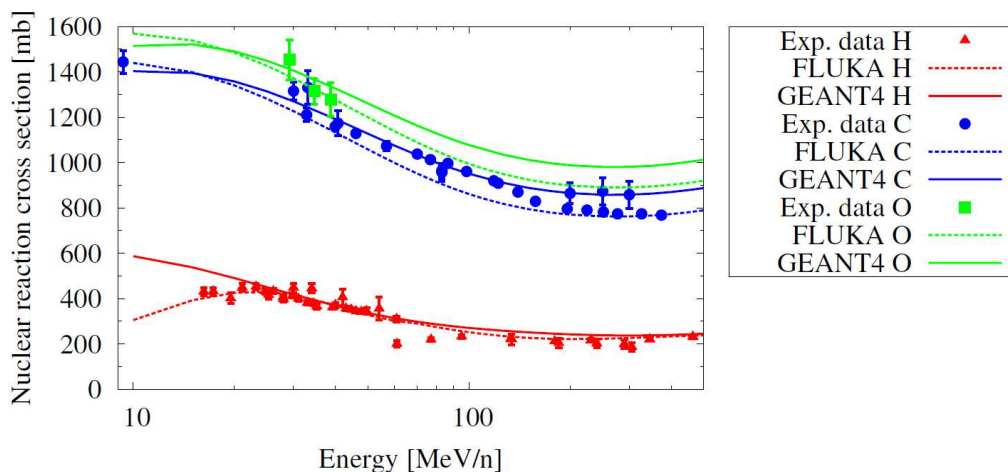


**Figure 5.2:** Different total nuclear cross sections for Carbon ion beams interacting with  $H$ ,  $C$  and  $O$  shown as predicted by FLUKA version 2008.3 and Geant4 version 9.3 compared with experimental data from [Kox84, Kox87, Sihver93, Fang2000, Zhang02, Takechi09]. Graph adapted from [Boehlen10].

Figure 5.2 shows total nuclear reaction cross sections used for the benchmark of the MC codes Geant4 and FLUKA in [Boehlen10]. The charge-changing cross sections of projectile-like fragments were compared between experimental data and simulation data. Differences of the MC codes as for Carbon and oxygen targets, Geant4 predicts cross sections which are about 10% larger for higher energies, than the ones predicted by FLUKA. The codes also differ significantly in the energy range below 20 MeV/n.

Omitting the nozzle geometry in the simulations leads to an additional reward in computational time, although it has an impact on the production of secondaries due to non-elastic nuclear scattering. Therefore it is a beneficial inclusion for accurate modeling of the particle energy spectra, with the disadvantage of longer computational time. [Elia19]

## 5.2 Materials and Methods

### 5.2.1 Scoring the energy spectra

To correctly score the energy spectra in GATE/Geant4, a scoring option was implemented into the source code of the energy spectrum actor. Actors are tools which allow interacting with the simulation. [GateUserGuide] There are two commonly applied concepts when it comes to scoring the fluence in MC simulations.

The surface crossing estimation assumes a surface having an infinitesimal thickness  $dt$ , a particle incident with an angle  $\theta$  with respect to the normal of the surface  $S$  will travel a segment  $\frac{dt}{\cos(\theta)}$ . Therefore the average surface fluence can be calculated by adding up  $\frac{dt}{\cos(\theta)}$  for each particle crossing the surface and dividing by the volume  $S dt$ . The surface crossing (plane spectra) concept is shown in Figure 5.3(a).

$$\Phi = \lim_{dt \rightarrow 0} \frac{\sum_i \frac{dt}{\cos(\theta_i)}}{S dt} \quad (5.1)$$

In eq. 5.1 incident particles with a large angle  $\theta$  will receive high weighting and a large contribution to the fluence, therefore will cause artifacts.

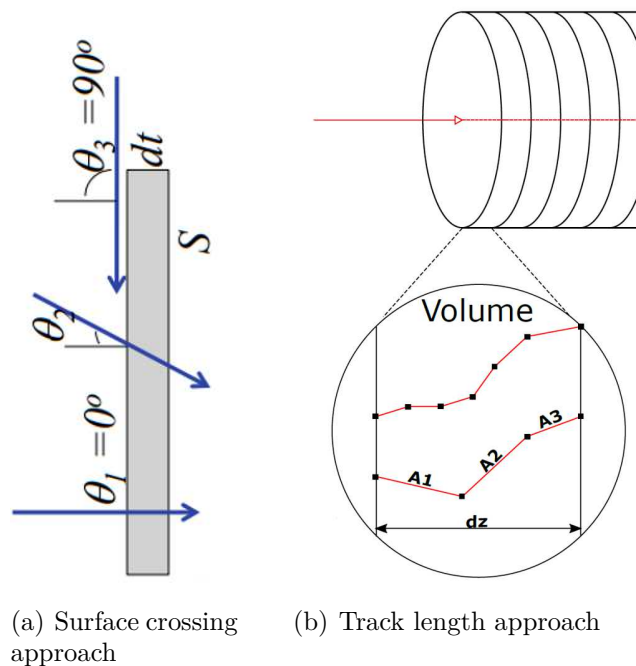


**Figure 5.3:** Illustration of the two different approach to score fluence. [Niessen19]

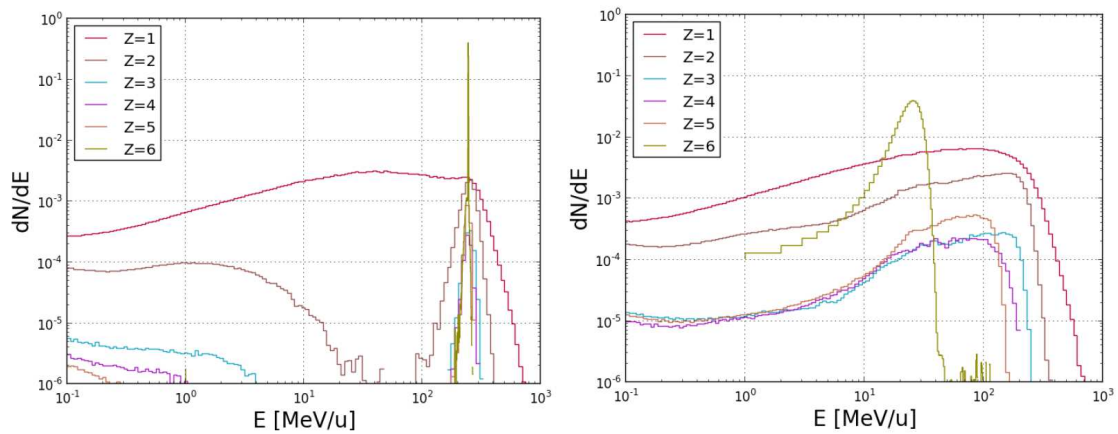
The more reliable way to score the energy spectra is the so-called track length estimation which is mathematically derived in [PapiezBattista94]. The track length approach (volume spectra) concept is shown in Figure 5.3(b). We chose the track length approach for the scoring of the energy spectra in our simulations.

### 5.2.2 RSL FLUKA spectra simulation setup

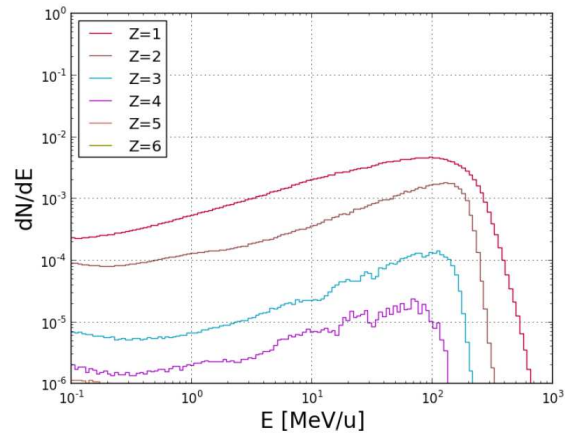
As mentioned earlier, the particle energy spectra are used to characterize the mixed radiation field at a certain depth in a Carbon ion beam and it is used in the computation of the RBE-weighted dose [RSMAN]. The differential spectra  $\frac{(E_k, T; x)}{dE_k}$  describe the distribution of primary ions and secondary charged particles with kinetic energy  $E_k$  and particle type  $T$  characterized by charge  $Z$ . RS used FLUKA for generating the spectra [[Ferrari05],[Boehlen14]]. Simulations were run for mono-energetic Carbon ions with energies at every 5 MeV/u between 50 - 450 MeV/u, resulting in a library containing spectra for 81 initial Carbon ion energies. According to RSL the number of primary particles was set to produce adequate counting statistics. The FLUKA built-in scoring algorithm USRTRACK was used to score the track lengths within each cylindrical volume. Scoring filters were set to only score particles with  $Z \leq 6$  and no isotopic discrimination was enforced. Fragments with charge,  $Z > 6$  were neglected for consistency with earlier work [Parodi12]. The differential spectra are stored in uniform depth bins with size 1 mm. The spectra of primary Carbon ions (i.e.,  $Z=6$ , since no isotopic discrimination) are stored using linear energy binning with bin edges ranging from 0 - 550 MeV/u and bin size 1 MeV/u. The spectra of fragments ( $Z < 6$ ) are stored using logarithmic energy binning with bin edges ranging from 0.1 - 999 MeV/u spread over 133 bins.

Examples taken from the [RSMAN] of the resulting particle energy spectra at different depths are shown in Figure 5.4. The Subfigures (a), (b), (c) show the energy spectra from a shallow position 5 cm deep in the water phantom in (a), where the primary particles nearly have their initial energy 300 MeV/u, while in (b) the energy spectra is shown for the position 17 cm deep in the water phantom, which is close to the Bragg Peak and the primary particles decrease their energy. In (c) a position of 25 cm deep in the water phantom is shown which is related to a position after the Bragg peak and primaries are completely absent. The Figure 5.5 shows an example of the variation of the total fragment yield with depth.

The spectra simulated with two different MC codes were compared at four different energies over the clinical range. (120 MeV/u, 322 MeV/u, 327 MeV/u and 400 MeV/u)



(a) 300 MeV/u Carbon ion beam at depth 5 cm (b) 300 MeV/u Carbon ion beam at depth 17 cm



(c) 300 MeV/u Carbon ion beam at depth 25 cm

**Figure 5.4:** Particle energy spectra simulated with FLUKA (per primary particle and MeV/u) for a 300 MeV/u Carbon ion beam at depth a)5 cm b)17 cm (Bragg peak adjacent) c)25 cm. [RSMAN]

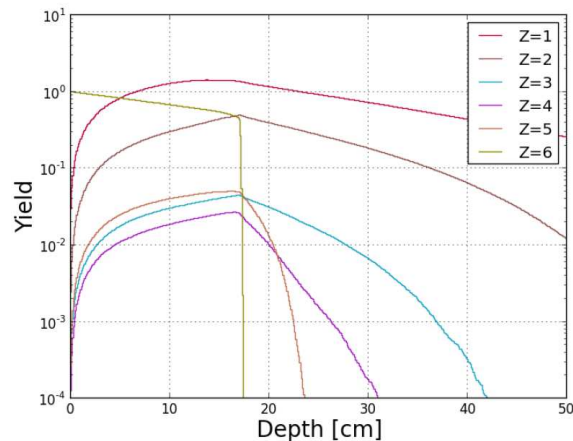


**Figure 5.5:** Fragment build-up (total number of particles per primary particle) simulated with FLUKA for a 300 MeV/u Carbon ion beam. [RSMAN]

### 5.2.3 MA GATE spectra simulation setup

The MC simulations were carried out using GATE version 8.2 in combination with Geant4 10.03.p03. The maximum step size was limited to 0.1 mm in the water phantom and 1 mm in air as these settings have proven a good compromise of computation time and accuracy. The simulations were carried out in water ignoring the polymethyl methacrylat entrance window of the water tank, as no effect, on the medium energy range nuclear interactions, is expected. [Resch19] Like in FLUKA, fragments with charge,  $Z > 6$  were neglected. The binning for the primary and secondary particles was chosen in the same way as for the spectra simulations in FLUKA by RSL. In GATE/Geant4 we simulated the full therapeutic energy range used at MedAustron which is from 120 MeV/u up to 402.8 MeV/u in 5 MeV/u steps, which results in a total number of 58 energies. Particle energy spectra were simulated and extracted for mono-energetic Carbon ions in a 50 cm deep water phantom. The schematic representation of the simulation setup can be found in Figure 5.6. Energy spectrum actors were attached to the full depth of the water phantom, each attached to a cylindrical volume with a thickness of 1 mm and a radius of 5 cm. Each ion type, distinguished by charge, had to be scored by a dedicated energy spectrum actor, resulting in a total number of 3000 energy spectrum actors per simulation per energy. Taking into account that we simulated 58 energies for the clinical energy range, this sums up to about 174000 energy spectrum actors. Each of this energy spectrum actors produced an output stored in a root file. These root files were postprocessed and converted into txt files using Bash and C++. The 174000 txt files were written into one single binary file. The binary file structure, which was used for this conversion, can be seen in Table 5.1. This binary file was used by RSL, to create a second beam model 'MA-GATE' for the TPS.

--Tag--	--Type--	--Unit--	--Size--	--Example--
version	double	-	1	0.1
treatmentModality	string*10	-	1	'CARBON'
scoringRadius	double	cm	1	-
nrOfNominalEnergies	int32	-	1	-
nominalEnergies	[double]	MeV	nrOfNominalEnergies	-
nrOfDepthBins	int32	-	1	-
depthBinEdges	[double]	cm	nrOfDepthBins+1	-
primaryZ	int32	-	1	6
nrOfPrimaryEnergyBins	int32	-	1	-
primaryEnergyBinEdges	[double]	MeV/u	nrOfPrimaryEnergyBins+1	-
primarySpectraVector	[[[double]]]	$((\text{cm}^2)(\text{MeV/u})^{-1})$	$\text{nrOfNominalEnergies} * \text{nrDepthBins} * \text{nrOfPrimaryEnergyBins}$	Fragments/Primary/Energy/Area
nrOfFragments	int32	-	1	5
fragmentZ	[int32]	-	nrOfFragments	[1,2,3,4,5]
nrOfFragmentEnergyBins	int32	-	1	-
fragmentEnergyBinEdges	[double]	MeV/u	nrOfFragmentEnergyBins+1	-
fragmentSpectraVector	[[[double]]]	$((\text{cm}^2)(\text{MeV/u})^{-1})$	$\text{nrOfNominalEnergies} * \text{nrDepthBins} * \text{nrFragments} * \text{nrOfFragmentEnergyBins}$	Fragments/Primary/Energy/Area

Table 5.1: Binary file structure of the fragment spectra file.

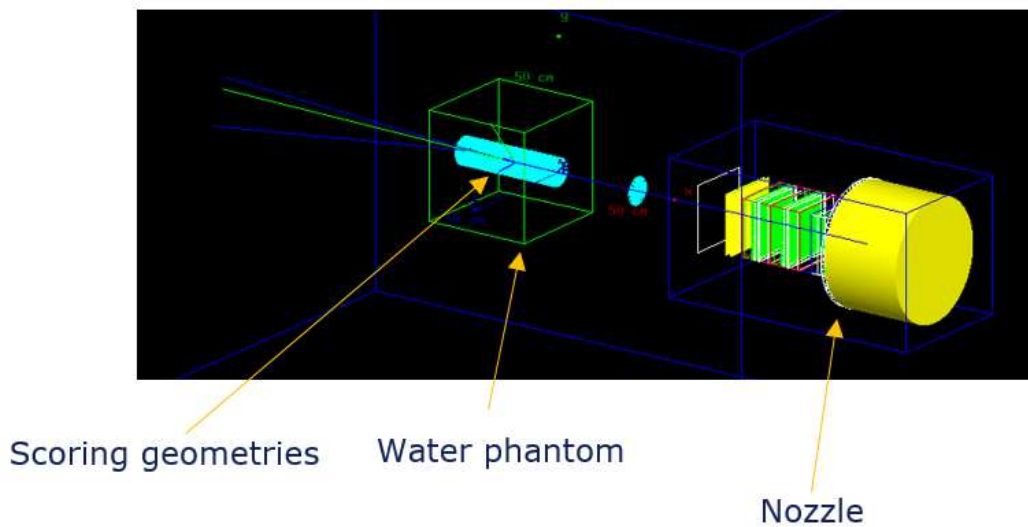


Figure 5.6: GATE/Geant4 simulation setup for the scoring of the energy particle spectra. Visible are two blue geometries, the smaller one is the frame around the MA nozzle which is described in detail by different boxes and cylinders, the bigger one is the 'World' in air which restricts the simulation volume. The green cubic is a water phantom with the dimension of  $50 \times 50 \times 50 \text{ cm}^3$ . The cyan circles within the water phantom are our scoring geometries with a radius of 5 cm and a thickness of 1 mm, where the energy spectra were scored.

A comparison of the particle energy spectra, pre-generated by RSL and the spectra generated with Gate/Geant4, was performed. Further postprocessing of both spectra to compare key features was done. At first direct spectra comparisons were carried out, followed by a comparison of the fluence of light fragments of the different spectra. As a third step similarities or dissimilarities between the two fluence averaged energies were investigated and finally a consistency check of our MC simulation procedure was performed using the fragment spectra to recompute the IRPDs via stopping powers.



## 5.3 Results

### 5.3.1 Energy spectra comparison

The MA-Gate and the RSL-FLUKA fluence agreed well for the primary Carbon ions. A comparison for a 400 MeV/u beam is shown in Figures 5.7 and 5.8 and for a 120 MeV/u beam in Figures 5.9 and 5.10. The Figures 5.7 and 5.9 show similar spectra, as both are close to the Bragg peak position but at different energies. The proton and Helium ion component have the highest amount of particles in the full energy range. The highest deviations between the RSL Fluka spectra and the MA GATE spectra were at the low energies below 1 MeV/u. At the high energies we observed that in GATE particles didn't reach energies as high as in FLUKA for all the particles. Boron ion spectra are matching well for the full energy range, while Lithium and Berillyium ions are off by about a factor 3. The Figures 5.8 and 5.10 also showed similarities in the spectra. These figures represent the particle energy spectra at the entrance of the water phantom. At the entrance of the water phantom a distinct build up of protons and Helium ions is observable. We saw the same deviations as in the position near the Bragg peak position. The MA-GATE spectra showed less particles below 1 MeV/u by a factor of 8 and the secondary particles reached a lower maximum energy compared to the RSL Fluka spectra. At the entrance of the water phantom the other secondary ions than proton and Helium ions are negligible, as their build up was not as pronounced. The particle energy spectra are shown normalized to the initial number of primary Carbon ions.

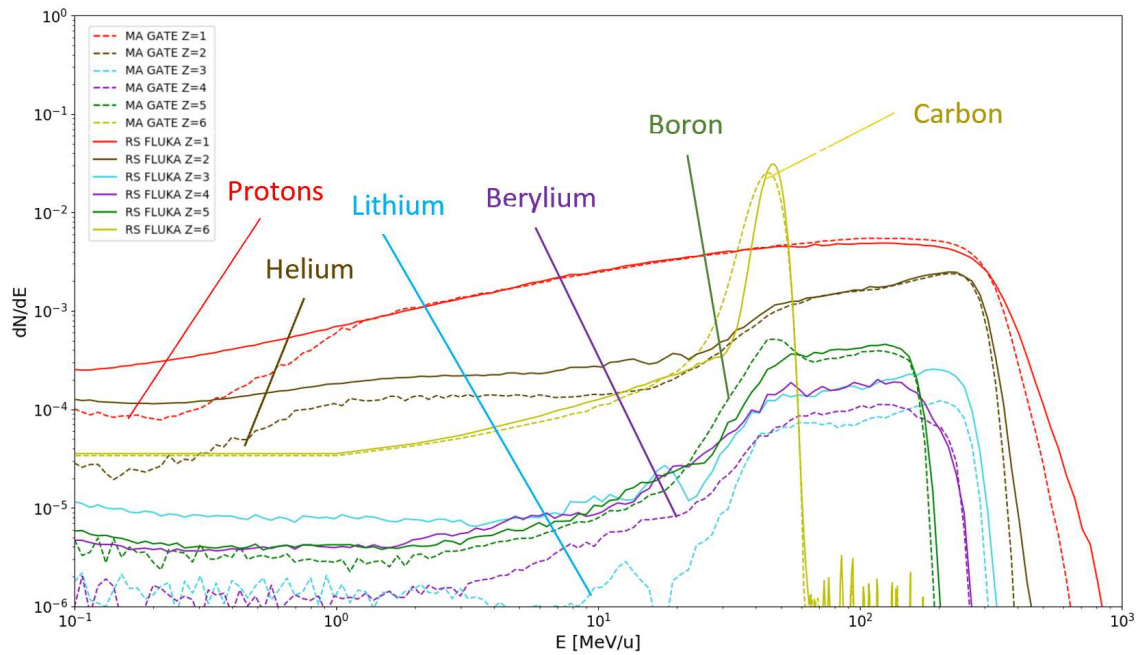


**Figure 5.7:** Particle energy spectra (per primary particle) for a 400 MeV/u Carbon ion beam 26 cm deep in the water phantom. Solid lines are computed with FLUKA (RSL) and dashed lines are computed with GATE/Geant4 (MA).

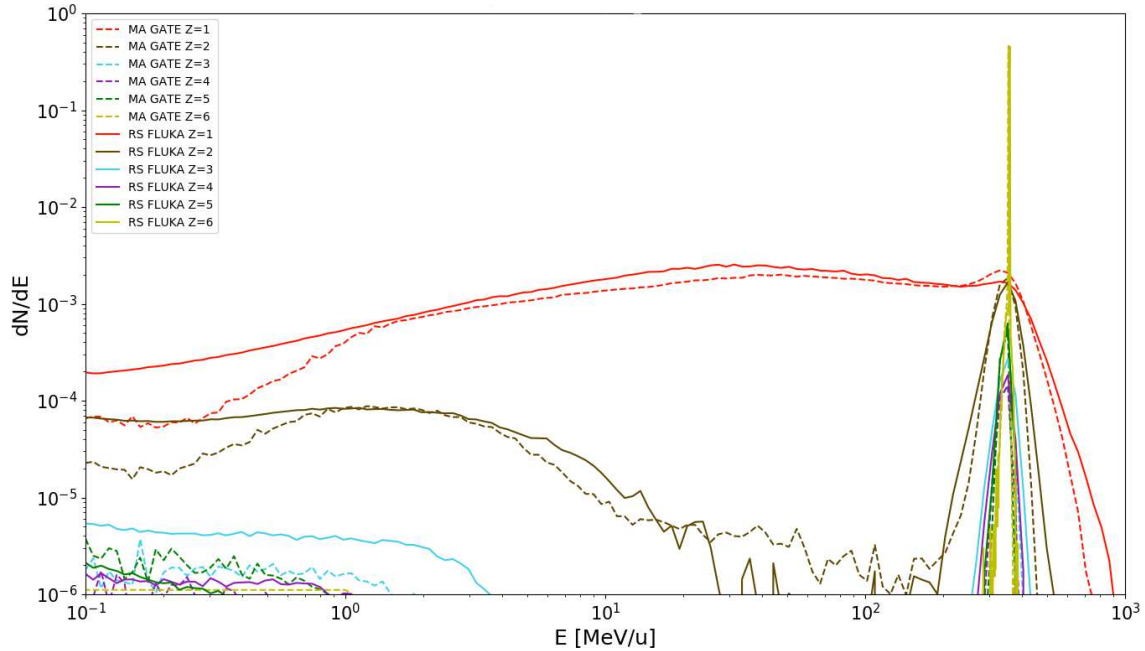


**Figure 5.8:** Particle energy spectra for a 400 MeV/u Carbon ion beam at 4 cm depth in the water phantom. Line and axis properties as above.

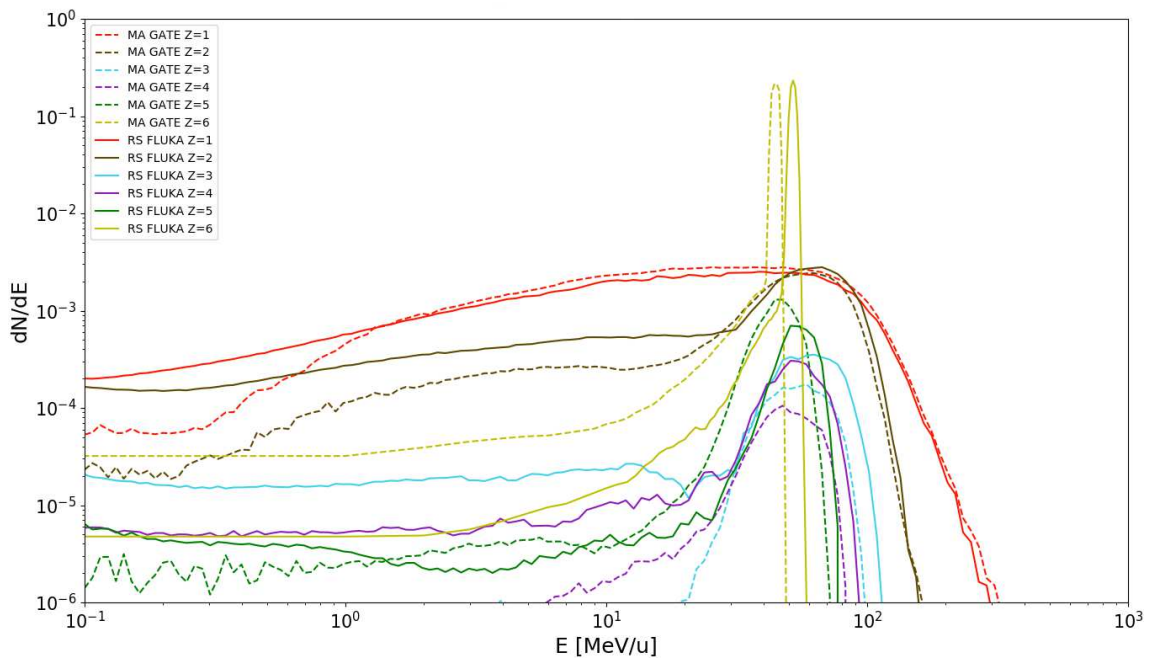


**Figure 5.9:** Particle energy spectra (per primary particle) for a 120 MeV/u Carbon ion beam (3 cm range in water) at 2 cm depth in the water phantom close to the Bragg peak region. Solid lines are computed with FLUKA (RSL) and dashed lines are computed with GATE/Geant4 (MA).

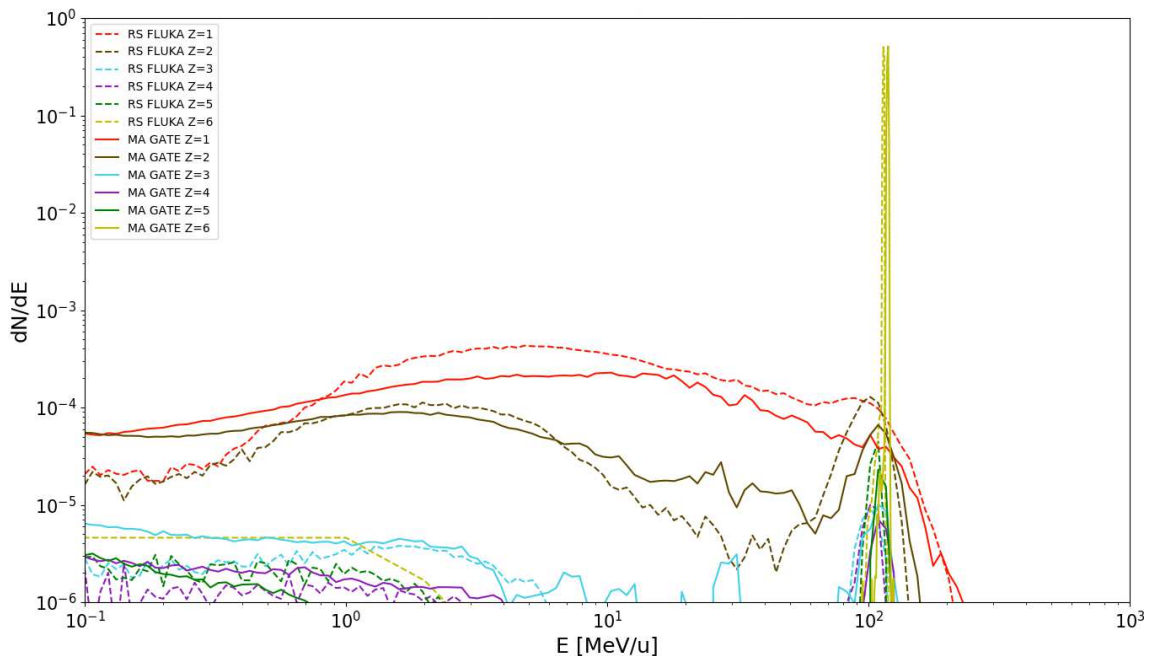


**Figure 5.10:** Particle energy spectra for a 120 MeV/u Carbon ion beam at 0 cm depth in water at the entrance of the water phantom. Line and axis properties as above.

### 5.3.2 Fragment fluence build up comparison

The fluence of light fragments increased steeply at first centimeters in water. While we see a build up of protons of about one third of the number of primary particles in the lower energetic Carbon beam of 120 MeV/u (shown in Figure 5.11). We observe a lot more fragmentation of the higher energetic Carbon ion beam of 320 MeV/u, which resulted in a large build up of secondaries (shown in Figure 5.12). The main contributors for the secondary particles, the protons from the MA-GATE spectra overweigh the RS-FLUKA spectra for most of the range and the Helium ions fluence showed the behavior of RS-FLUKA spectra having more than the MA-GATE spectra.

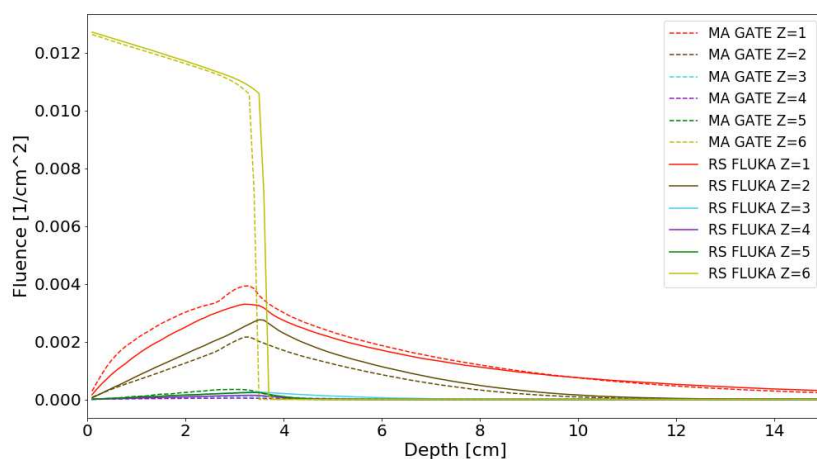


**Figure 5.11:** Fragment fluence build up over depth for a 120 MeV/u Carbon ion beam. The dashed lines show the fragment build up connected to the MA GATE simulated spectra, while the solid lines represent the RS FLUKA simulated fragment fluence build up.

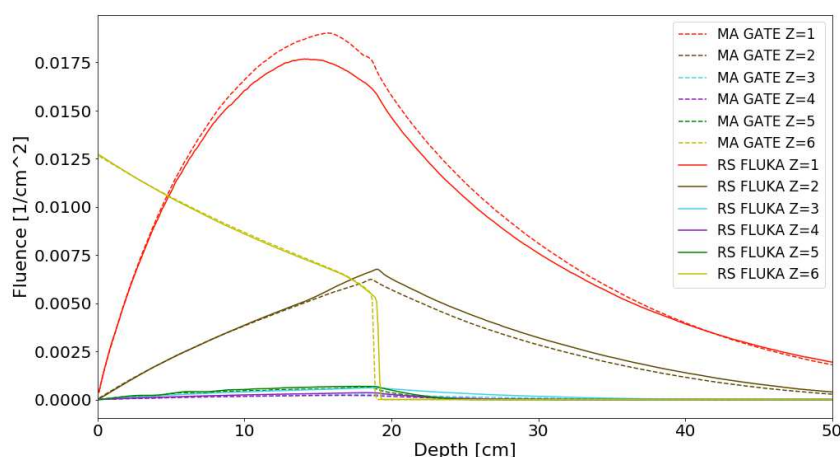


**Figure 5.12:** Fragment fluence build-up over depth for a 320 MeV/u Carbon ion beam. The dashed lines show the fragment build up connected to the MA GATE simulated spectra, while the solid lines represent the RS FLUKA simulated fragment fluence build up.

### 5.3.3 Fluence averaged energy comparison

The fluence averaged energies over depth and fragment were similar for the RS FLUKA spectra and the MA GATE spectra. Figure 5.13 showed the mean fragment energies for a 120 MeV/u Carbon ion beam and Figure 5.14 showed the mean fragment energies for a 320 MeV/u Carbon ion beam. We observed, the heavier the particles, the higher the mean energies were before the Bragg peak and also the heavier the particles, the higher was the decrease of energy after the Bragg peak.

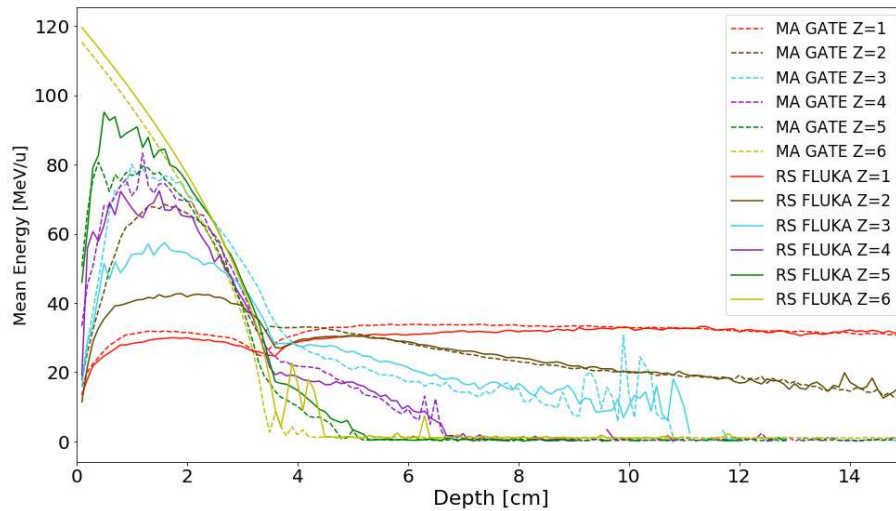


**Figure 5.13:** The fluence averaged energies for the different specific ions. Solid lines show the RS FLUKA mean energies, while dashed lines represent the MA GATE simulated mean energies. Simulations were made for a 120 MeV/u Carbon ion beam.

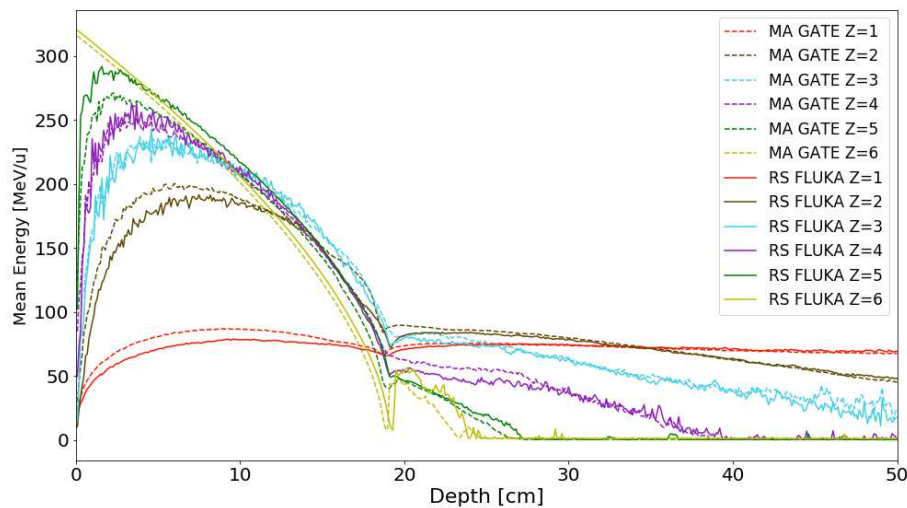


**Figure 5.14:** The fluence averaged energies for the different specific ions. Solid lines show the RS FLUKA mean energies, while dashed lines represent the MA GATE simulated mean energies. Simulations were made for a 320 MeV/u Carbon ion beam.



### 5.3.4 Integrated radial profiles as a function of depth

A recalculation of the integrated radial profiles as a function of depth for the spectra, by weighting the differential fluence with corresponding stopping power over 1mm steps was done. Stopping powers were taken from [ICRU90] and linear interpolated for the needed energies. Figures 5.15 and 5.16 show the comparisons of the 120 MeV/u and 400 MeV/u Carbon beams. This served the purpose of a consistency check, for our fluence spectra MC simulations, where we compare between the recomputed IRPDs and the simulated IRPDs (scored by a dose actor) with the same simulation conditions. The recomputation of the IRPDs with the stopping power was only done for Carbon ions, but the approach remains valid as a consistency check, because Carbon ions have the most impact on the range. Results as the summed up spectra weighted by stopping power resembled the expected Carbon Bragg peak shape and the range difference is negligible and within the uncertainties of the MC simulations. The recomputed IRPD differs an absolute value of 0.01 cm which results in 0.3% relative deviation for the 120 MeV/u Carbon ion beam and the 400 MeV/u Carbon ion beam differs an absolute value of 0.02 cm and in terms of relative deviation about 0.01%.

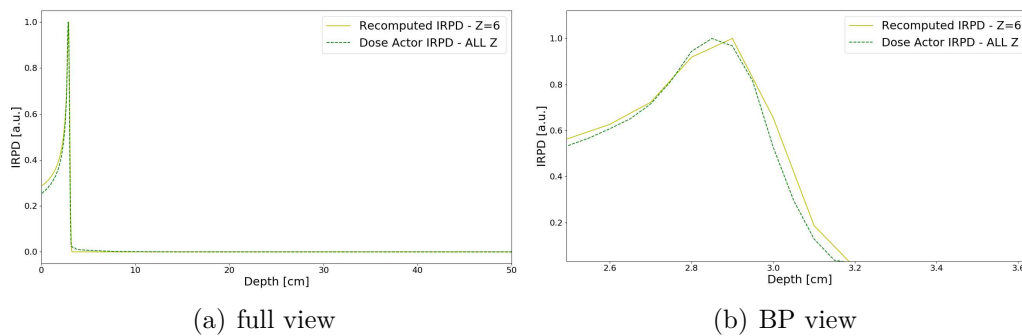


**Figure 5.15:** Integrated radial profiles as a function of depth for a 120 MeV/u Carbon ion beam. The yellow solid line shows the recomputed IRPDs. The green line shows the IRPDs simulated with the dose actor.

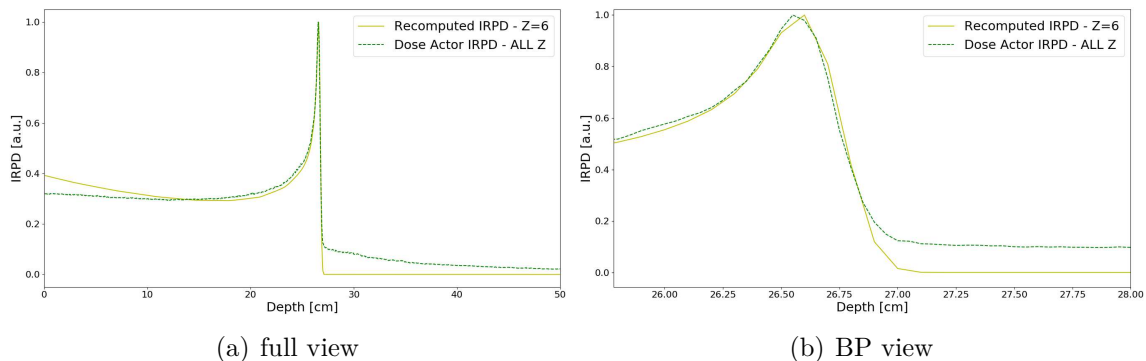


**Figure 5.16:** IRPDs for a 400 MeV/u Carbon ion beam. The solid yellow line shows the recomputed IRPD. The green line shows the IRPD simulated with the dose actor.

Figure 5.17 displays the importance of consistency in the simulation setup. In this figure the two different approaches the 'dose actor scoring' and the 'energy spectra recomputation' were done using different materials for the water phantom. ("G4\_WATER" and "WATER": G4\_WATER is constructed via Geant4 internal database allowing to use internal data on density effect parameterisation and [ICRU73] on stopping powers. Thus, absolute ranges and Bragg peak position are more precise with Geant4 and G4\_WATER. In the case of hand-made material, like WATER, it is not possible to access these data and stopping powers/ranges are using general algorithms which is less precise.).

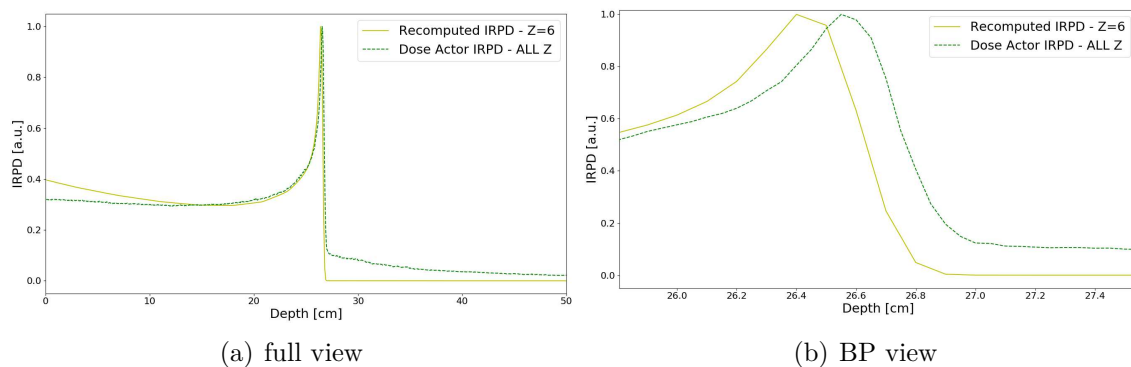


**Figure 5.17:** IRPDs for a 400 MeV/u Carbon ion beam. The yellow solid line shows the recomputed IRPD. The green line shows the IRPD simulated with the dose actor.

Results as the summed up spectra weighted by stopping power show a clear shift in the Bragg peaks and therefore an offset in range. The usage of different water materials showed an absolute difference of 0.138 cm and in terms of relative deviation about 0,5%, which does not seem large, but working with the wrong material would lead to a crucial non tolerable difference in the RBE-weighted dose in the treatment plans in the TPS RS.



## 5.4 Conclusion

For the purpose of reliably scoring the fluence and therefore the energy spectra, an energy spectrum actor was developed in GATE/Geant4, based on the track length approach. Particle energy spectra were simulated at MA, using GATE version 8.2 in combination with Geant4 10.03.p03 and a dedicated beam model including a full geometrical description of the nozzle elements. 58 energies were simulated covering the full therapeutical energy range available for Carbon ion beams at MA. The spectra were simulated and later extracted in a 50 cm deep water phantom with a resolution of 1mm, storing the data in a binary file with a specific file structure. Different methods to compare the particle energy spectra generated from different MC codes, FLUKA and GATE/Geant4, have been applied.

Fragment build up evaluation revealed, that the build up curves were similar and showed the predicted behavior, a steep build up of secondaries in the first centimeters in water. The amount of protons was predicted higher in the MA-GATE spectra with a maximum difference of up to 10 %, while the secondary production of Helium ions was predicted lower in the MA-GATE spectra by about 8 %, close to the Bragg peak position in water.

The fluence averaged energies calculated for both spectra confirm heavier particles show higher fluence-average energies than lighter particles before the Bragg peak, followed by a steep decrease of energy after the Bragg peak for the heavier particles. For the 320 MeV/u Carbon ion beam, proton and Helium ion energies, were predicted about 10-15% higher for the MA-GATE spectra, whereas Boron ion energies were 10-15 % higher for the RS-FLUKA spectra before the Bragg peak depth in water. Lithium and Beryllium are matching within 5% differences before the Bragg peak. After the Bragg peak the fluence averaged energies fit within total differences of 5% with local disagreements.

The comparison of the IRPD for the recomputation with the spectra and the IRPD scored with the dose actor has shown that our simulation methods were consistent within an absolute difference of 0.01 cm and a relative deviation of 0.3% for a 120 MeV/u Carbon ion beam and with an absolute difference of 0.02 cm and a relative deviation of 0.01% for a 400 MeV/u Carbon ion beam. Within a direct comparison of the MA-Gate and the RSL-FLUKA spectra, the fluence agreed well for the main contribution, the primary Carbon ions. However, the fluence at low energies below 1 MeV/u was considerably lower in GATE for all secondary particles and mainly for the proton and Helium fluence components.

The impact on the RBE weighted dose, by the differences in fluence, fluence averaged energies and range observed, is expected to be low but needs to be quantified. Therefore an evaluation was carried out which can be found in the next Chapter 6.

# 6

## RBE-weighted dose evaluation

### 6.1 Introduction

In the previous chapters, we have laid the foundation of this chapter by collecting the pieces needed for the creation of the beam models used for the comparison in the treatment planning system RayStation at MedAustron.

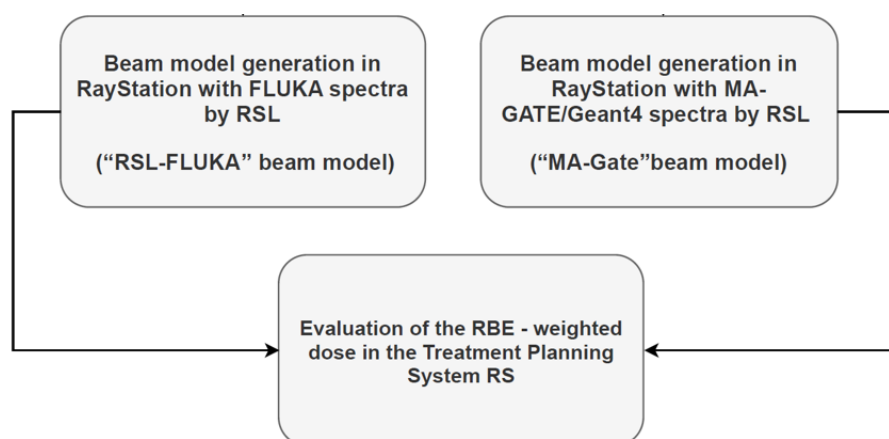


**Figure 6.1:** Workflow chart of the RBE-weighted dose evaluation in RS.

In this chapter, we present the comparison of different treatment cases, where two different beam models were applied. As visible in Figure 6.1 the beam model "MA-GATE" uses energy spectra created in GATE/Geant4, while the beam model "RSL-FLUKA" uses energy spectra simulated in FLUKA. Both beam models use the basic Carbon beam measurements from MA.

## 6.2 Materials and Methods

Following the MA treatment guideline for Carbon ion radiotherapy for mucosal melanoma in the head and neck, we present the shortened version of the standard procedure used for planning. [KohlenstoffTherapiekonzeptMA19]

Each patient undergoes the following steps:

- immobilization (headrest, moldcare)
- simulation imaging (CT, MRI)
- structure contouring
- dose prescription
- beam angle selection
- optimization and final dose calculation

### Target volumes

For each patient, a GTV, a larger CTV1 and a smaller CTV2 was contoured. The GTV was contoured considering the post contrast enhanced T1 weighted MR, the T2 weighted MR and the DWI MR. GTV was adapted on the CT scan to account for potential mismatch in image fusion. The CTV1 accounts for areas with risk of microscopic infiltration. The GTV was expanded geometrically by 15-20 mm. All partially involved compartment are entirely included in CTV1. The CTV2 is a 10-15 mm geometric expansion of the GTV without expansion for clinically negative lymph nodes or mucosa. CTV2 is adapted for anatomy analogously to CTV1. CTV2 is not extend outside CTV1.

PTV1 and PTV2 were obtained expanding CTV1 and CTV2 3 mm isotropically.

### Dose prescription

A shrinking field approach is employed. Nine fractions are prescribed to PTV1 and seven fractions are subsequently prescribed to PTV2. Dose per fractions is either 4.1 Gy or 4.3 Gy based on expected toxicity.

PTV1: 38.7 Gy in 9 fractions of 4.3 Gy at four fractions per week.

PTV2: 30.1 Gy in 7 fractions of 4.3 Gy at four fractions per week.

Total dose to PTV2: 68.7 Gy in 16 fractions of 4.3 Gy at four fractions per week.

Prescription and optimization is done in terms of RBE-weighted dose. RBE is calculated by the TPS from Raysearch using the Local Effect Model (LEM) version I, with the following parameters ( $\alpha$  0.1 Gy<sup>1</sup>,  $\beta$  0.05 Gy<sup>2</sup>,  $D_t$  30 Gy, nuclear radius five  $\mu$ m).

### 6.2.1 RBE-weighted dose comparison in water geometry

A comparison of the RBE-weighted dose computed with the "RSL-FLUKA" beam model and the one computed with the "MA-GATE" beam model was performed first in water. We investigated the RBE-weighted dose differences for the two different beam models for different regular shaped fields box-like targets and mono-energetic square fields in water. The boxes which were investigated have the following dimensions:

- box  $6 \times 6 \times 6 \text{ cm}^3$  - centered at 6 cm depth in water (called box6)
- box  $8 \times 8 \times 8 \text{ cm}^3$  - centered at 13 cm depth in water (called box8)
- box  $10 \times 10 \times 10 \text{ cm}^3$  - centered at 21.8 cm depth in water (called box10)

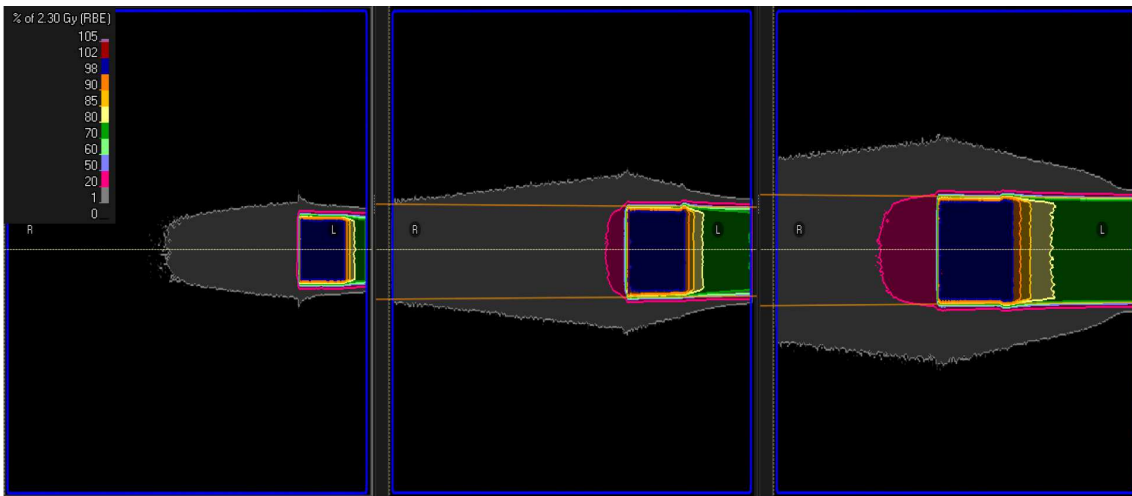


**Figure 6.2:** Dose distributions of the three box-like targets. From the left to the right the box6, box8 and box10. (For visualization purposes, the actual image was scaled, therefore boxes don't appear quadratic)

RBE-weighted dose distributions were computed for regular shaped fields (boxes) in water in RS v8B. The biological model that has been used to calculate the RBE was LEM I. Three treatment plans were optimized having box6 centered at a depth of 6 cm at ISD0 (see also 4.2.1), box8 at ISD0 centered at a depth of 13 cm and a box of box10 centered at a depth of 21.8 cm as a target at ISD0. (shown in Figure 6.2) In addition we planned a superficial target with RaShi (box of  $6 \times 6 \times 6 \text{ cm}^3$  centered at 5 cm at ISD50). We use a Range Shifter (RaShi) with a water equivalence of 3.5 cm to pull back the Bragg peak. A RBE-weighted dose of 2.3 Gy (RBE) was planned for each box.

Additionally different energy layers were investigated and each energy layer geometry covered one mono-energetic Carbon ion beam. The following energy layers were investigated:

- energy layer for a Carbon ion beam of 120 MeV/u
- energy layer for a Carbon ion beam of 284.7 MeV/u
- energy layer for a Carbon ion beam of 402.8 MeV/u

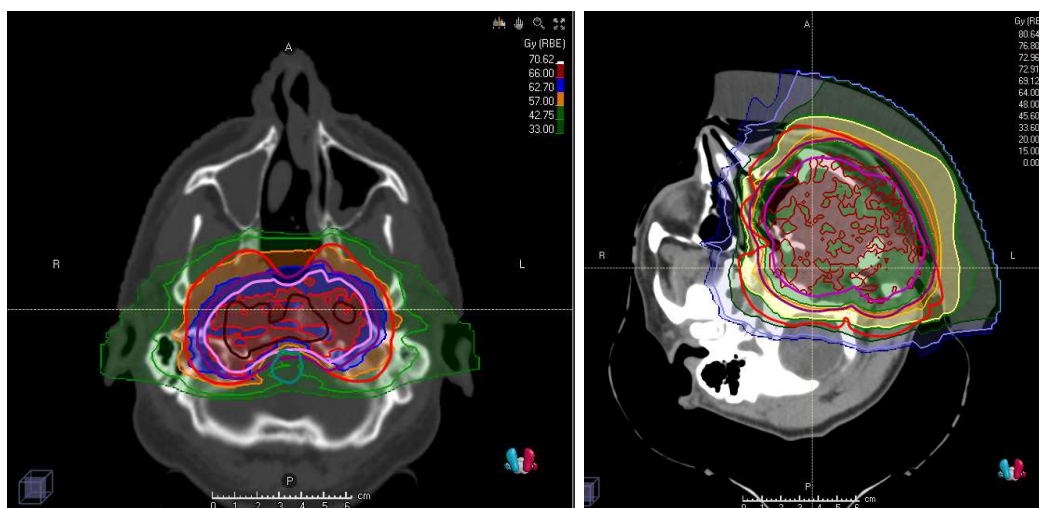
Also the layers were planned and optimized with a total RBE-weighted dose of 2.3 Gy (RBE) for each geometry.

### 6.2.2 RBE-weighted dose comparison in patient geometry: clinical cases in test environment

As a second step five different clinical plans were investigated with the following characteristics:

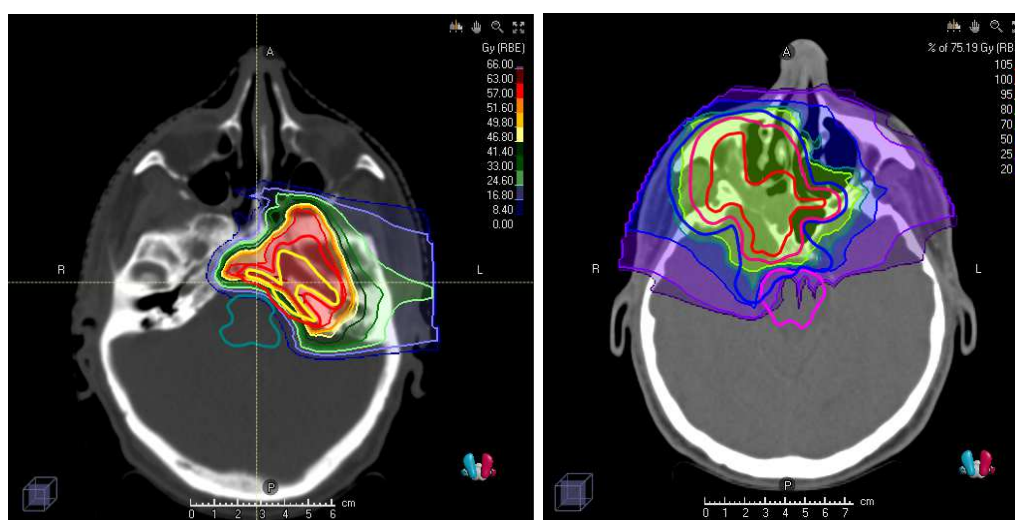
- patient 1 - head and neck tumour (clinical indication: Skullbase chordoma)
- patient 2 - head and neck tumour with bolus (clinical indication: HN sarcoma)
- patient 3 - head and neck tumour with hypofractionation (clinical indication: HN RT)
- patient 4 - head and neck tumour with hypofractionation (clinical indication: ReRT)
- patient 5 - head and neck tumour with hypofractionation (clinical indication: HN ACC)

An overview of the different patient anatomies and dose distributions is given in Figure 6.3.



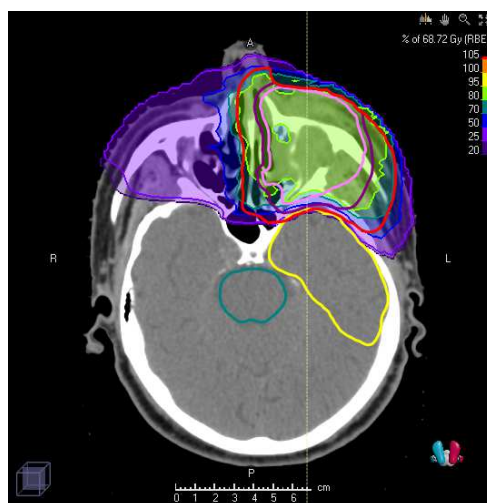
(a) Plan 1 - dose distribution overview

(b) Plan 2 - dose distribution overview



(c) Plan 3 - dose distribution overview

(d) Plan 4 - dose distribution overview



(e) Plan 5 - dose distribution overview

**Figure 6.3:** Overview of the clinical plans showing a slice of the patients anatomy and dose distribution in the transversal plane.



## 6.3 Results

### 6.3.1 RBE-weighted dose comparison in water geometries

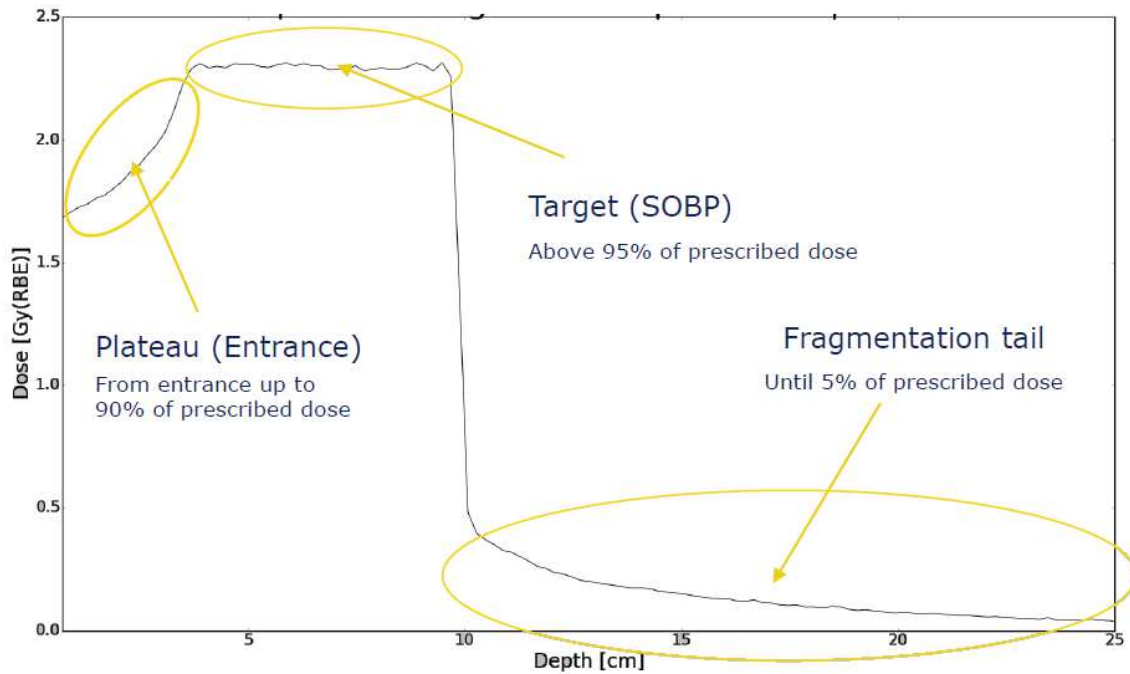


**Figure 6.4:** RBE-weighted integrated radial profile as a function of depth to visualize the different regions investigated.

Figure 6.4 is used to explain the results of the smallest box with the nearest position referred to the beam. Three different regions were analyzed:

- the plateau (entrance) region - up to 90 % prescribed dose
- the target (SOBP) region - above 95% of prescribed dose
- the fragmentation tail - ranging from 5 % to 0.1 % of the prescribed dose

The relative deviations of the RBE-weighted doses were computed as:

$$\text{Relative Deviation} = \frac{\text{RS-FLUKA dose} - \text{MA-GATE dose}}{\text{RS-FLUKA dose} \times 100}. \quad (6.1)$$



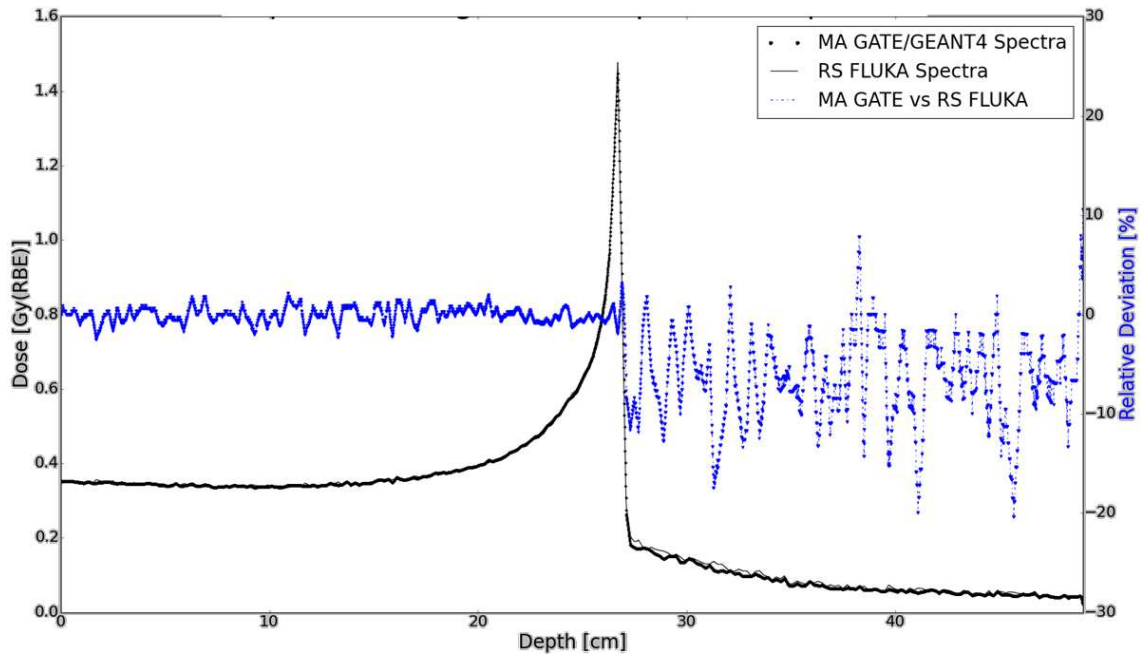


**Figure 6.5:** RBE-weighted integrated radial profile as a function of depth for the mono-energetic layer at 1440 MeV.

In Figure 6.5 the RBE-IRPD of the pristine BP layer target is shown. We see less than 3% deviation in the entrance region till the Bragg peak, while at the Bragg peak fall off region, which starts after the peak and ends at the beginning of the fragmentation tail, we see an increase of deviation of dose up to 5%. This might be due to a small energy shift of the different beam models as the BP is very sensitive to the range. In the fragmentation tail we observe deviations of up to  $\pm 15\%$  difference and the reason for this might be, that we have a low dose region with fluctuation, where the absolute deviation is small.

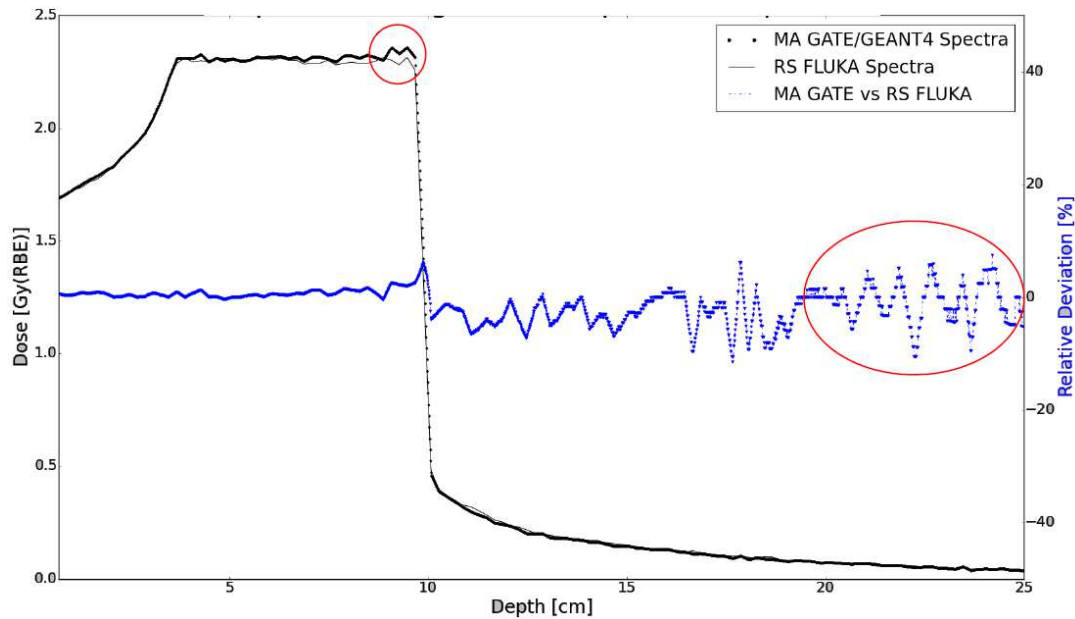


**Figure 6.6:** This Figure shows the RBE-weighted SOBPs for the different beam models. The dose from the MA GATE/Geant4 Spectra beam model is visible as the darker (dotted) line and the dose calculated with the RS FLUKA spectra beam model is displayed as the thin solid line. Relative deviation in % is shown as the blue dashed-dotted line.

A comparison was made of the RBE-weighted SOBPs from the different beam models. Figure 6.6 shows one of the SOBPs for the box6 target. We see the highest relevant deviations in the distal part of the target, marked by the small red circle in the graph. The bigger elliptical structure shows a higher deviation in the deeper fragmentation tail, but there we also see a low dose as already mentioned in the case for the layer target.

**Table 6.1:** Summary of the different results obtained in the target boxes in water.

Box Result Summary	Box 6	Box 8	Box 10	Box 6 w/ RaShi
Plateau	$0.4 \% \pm 0.3 \%$	$0.2 \% \pm 0.2 \%$	$0.1 \% \pm 0.2 \%$	$0.3 \% \pm 0.1 \%$
Target	$0.7 \% \pm 0.7 \%$	$0.3 \% \pm 0.3 \%$	$0.1 \% \pm 0.2 \%$	$0.6 \% \pm 0.4 \%$
Tail	$-3.0 \% \pm 2.2 \%$	$-3.3 \% \pm 2.6 \%$	$-4.6 \% \pm 1.5 \%$	$-4.1 \% \pm 2.1 \%$

In Table 6.1, the three results from different boxes are summarized. If we take a look at the fragmentation tail, we can assume for deeper and bigger boxes, we expect dose underestimation in the fragmentation tail by the RBE-weighted dose created by the MA-GATE beam model compared to the RS-FLUKA beam model.

### 6.3.2 RBE-weighted dose comparison in patient geometry: clinical cases in test environment

We show patient plan number five out of the five clinical plans investigated in detail and give a summary of the results of the different plans in this section. The clinical case presented is an HN tumor. For the PTV1 a Dose of 45 Gy (RBE) was prescribed in a fractionation scheme of 15x3 Gy RBE. The PTV2, which is sequential to the PTV1, has a prescribed dose of 15 Gy (RBE) delivered in 5 fractions. The dose of the PTV1 and PTV2 is achieved by six different beams as can be seen in Figure 6.7.

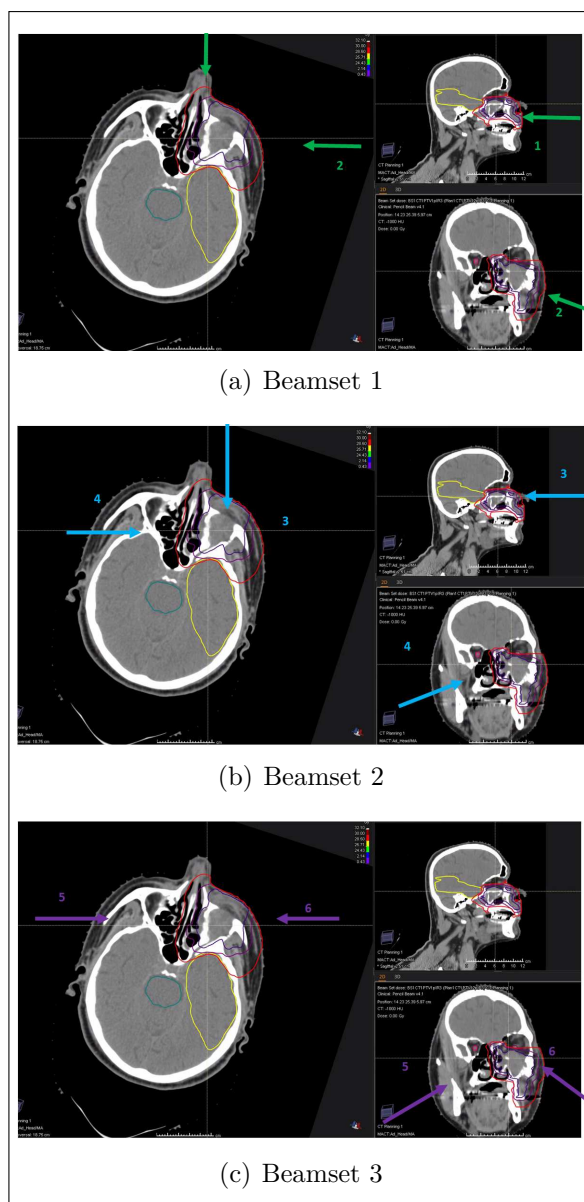


**Figure 6.7:** Three different beamsets applied to the patient in order to guarantee the dose distribution needed for PTV1 and PTV2.

### Dose distribution overview and dose difference

Figure 6.8 shows an overview of the dose distribution and also the dose differences induced by the different beam models 'MA-GATE' vs 'RSL-FLUKA'. We see differences of up to 3% in minor local parts of the plan, which corresponds to differences of up to 2 Gy (RBE), but as these differences only appear in local spots, they are acceptable.

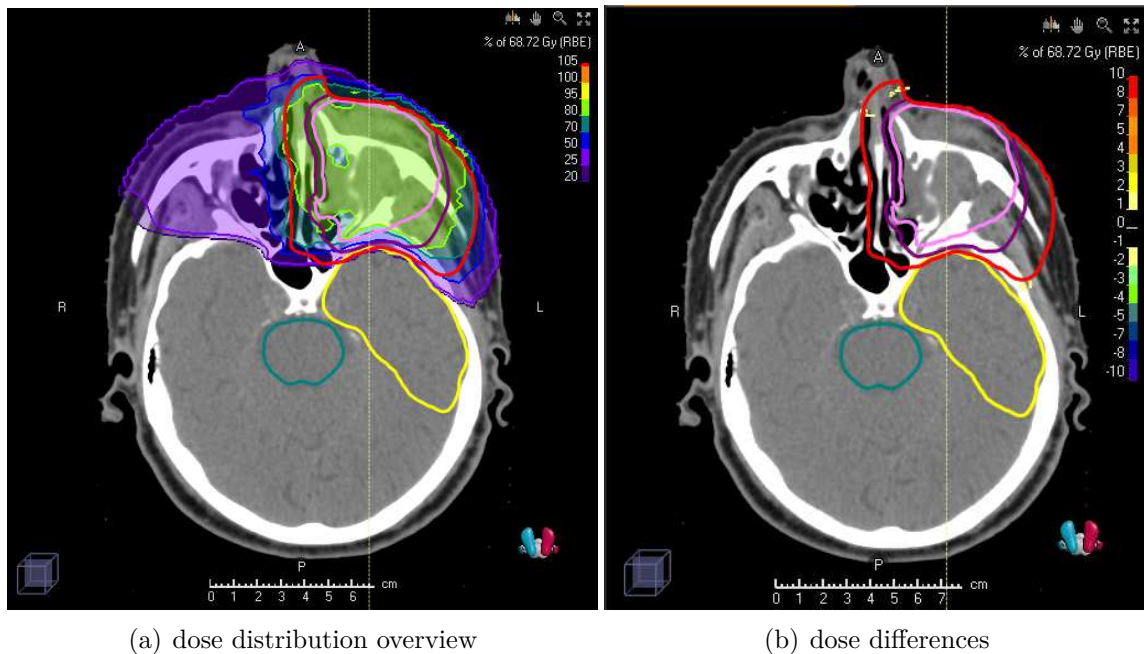


**Figure 6.8:** Left: Overview of the clinical patient plan number five, planned with the RSL-FLUKA clinical beam model and recomputed with the MA-GATE beam model; Right: Dose differences due to the different beam models "MA-GATE" vs RSL-FLUKA in the RBE-weighted dose distribution. In the right picture small differences are visible in the nose region of up to 3%.

### Organs at risk and target results

The plan for patient 5 was created with the focus on meeting the constraints given for the organs at risk and target volumes, which are summarized in the patient plan 5 results summary in Table 6.3 and Table 6.2.

In Figure 6.9 the dose volume histograms for the two different RBE-weighted dose distributions at the organs at risk are shown. The different DVH for the target volumes are displayed in Figure 6.10. There are no relevant clinical differences comparing the DVHs computed with the "RSL-FLUKA" model and with the "MA-GATE" model for all OARs and PTVs.

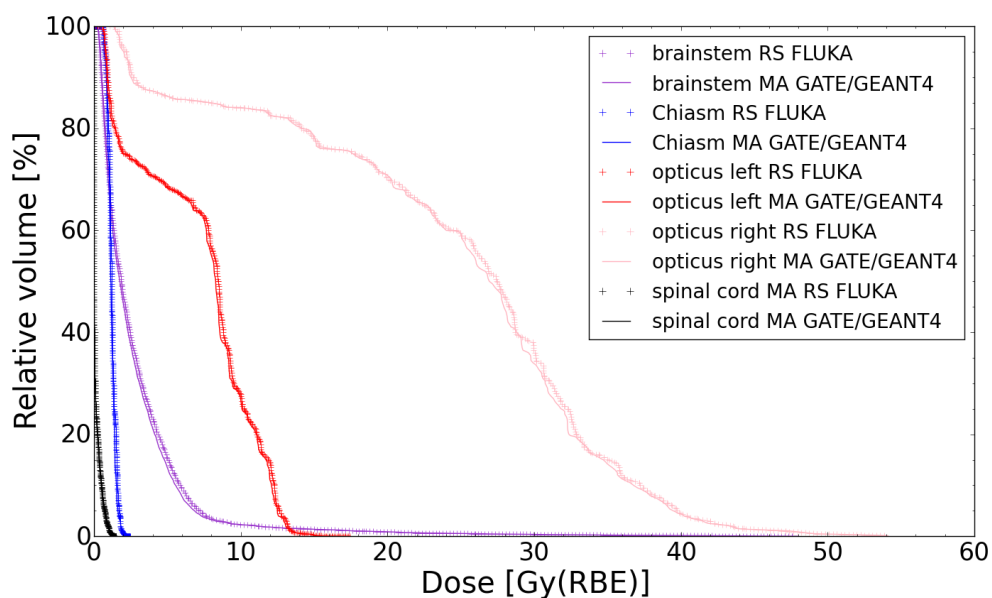


**Figure 6.9:** Displayed are dose volume histograms of the OARs extracted from patient plan 5. In purple the brainstem, in blue the chiasm, in black the spinal cord, in red the opticus left and in flesh tone the opticus right is viewed. Doses from the MA-GATE beam model are viewed in a solid line while the RS-FLUKA beam model doses are displayed in crosses.

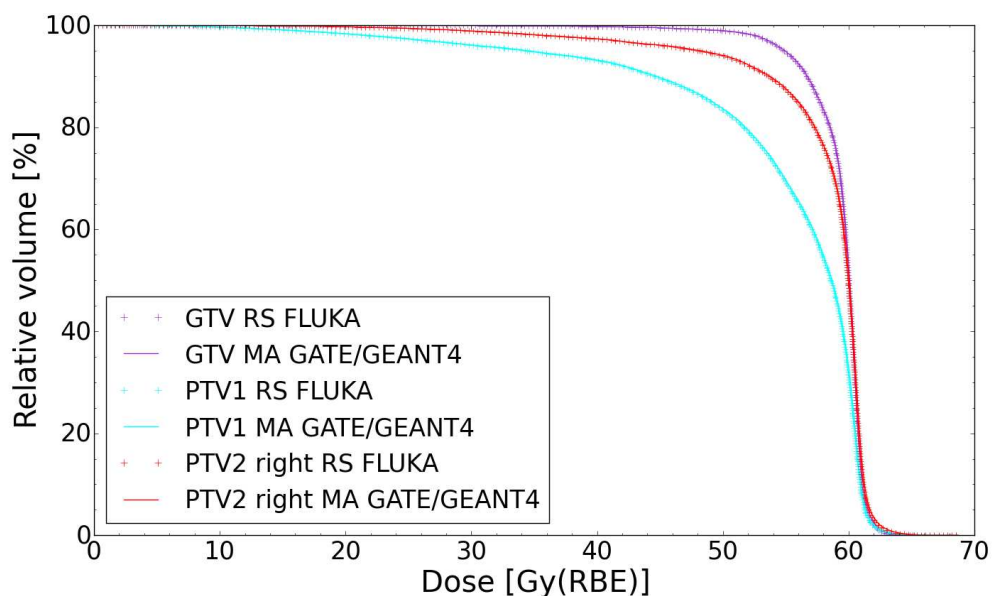


**Figure 6.10:** Displayed are dose volume histograms of the target volumes extracted from patient plan 5. In purple the GTV is viewed, cyan is the PTV1 and red is the PTV2. Doses from the MA-GATE beam model are viewed in a solid line while the RS-FLUKA beam model doses are displayed in crosses.

In Table 6.2 and Table 6.3 we list a brief summary of the dose differences in the critical volumes and targets of the different clinical plans. The maximum deviation for the target volumes was less than 2% with the highest deviation in Plan 3 for the minimum dose DRBE,99 of 1.9%. The organs at risk showed a maximum deviation of up to 5.9% in the spinalcord in plan number 5. We observed higher deviations if the nominal (observed) doses were far below the expected (prescribed) dose maximum. We also made a comparison of single beamsets with and without RaShi and similar results were found. No clinical relevant differences were found between the doses computed with the different beam models 'RSL-FLUKA' and 'MA-GATE' for the clinical plans.

**Table 6.2:** Summary of the clinical plan results for organs at risk. Each table shows the following: The minimum dose DRBE,99%, the median dose DRBE,50% and DRBE,1% for different targets PTV1, PTV2, PTV3, CTV1, CTV2, GTV. The relative deviations of the RBE-weighted doses were computed as ('RS-FLUKA dose')-( 'MA-GATE dose')/('RS-FLUKA dose') $\times$ 100. (eq. 6.1)

(a) Plan 1 results for target volumes.

Target Volumes	PTV1	PTV2	PTV3
minimum dose DRBE,99%	0.5%	0.3%	0.8%
median dose DRBE,50%	0.5%	0.4%	0.4%
maximum dose DRBE,1%	0.5%	0.5%	0.6%

(b) Plan 2 results for target volumes.

Target Volumes	PTV1	PTV2	PTV3
minimum dose DRBE,99%	0.8%	0.9%	0.6%
median dose DRBE,50%	0.5%	-1.1%	0.5%
maximum dose DRBE,1%	0.7%	0.7%	0.7%

(c) Plan 3 results for target volumes.

Target Volumes	PTV1	CTV1	GTV1
minimum dose DRBE,99%	1.9%	1.4%	1.4%
median dose DRBE,50%	0.6%	0.6%	0.6%
maximum dose DRBE,1%	0.5%	0.4%	0.4%

(d) Plan 4 results for target volumes.

Target Volumes	PTV1	PTV2	GTV
minimum dose DRBE,99%	1.7%	1.0%	1.2%
median dose DRBE,50%	0.5%	0.8%	0.5%
maximum dose DRBE,1%	0.8%	0.8%	0.8%

(e) Plan 5 results for target volumes.

Target Volumes	PTV1	PTV2	CTV2
minimum dose DRBE,99%	0.1%	0.1%	0.3%
median dose DRBE,50%	0.2%	0.2%	0.2%
maximum dose DRBE,1%	0.1%	0.3%	0.3%



**Table 6.3:** Summary of the clinical plan results for organs at risk. Each table shows the following: The expected (prescribed) maximum dose, the nominal (observed) dose and the relative deviation of different organs: brainstem, spinal cord, chiasm, opticus left, opticus right, cochlea left, cochlea right, templobe left and the macula left. The relative deviations of the RBE-weighted doses were computed as  $(\text{'RS-FLUKA dose'}) - (\text{'MA-GATE dose'}) / (\text{'RS-FLUKA dose'}) \times 100$ . (eq. 6.1)

(a) Plan 1 results for organs at risk.

Organs at risk	brainstem	spinalcord	chiasm	opticusLeft	opticusRight
Relative deviation:	0.4%	0.5%	0.2%	0.1%	1.0%
Dmax(expected)	54 Gy(RBE)	54 Gy(RBE)	50 Gy(RBE)	50 Gy(RBE)	50 Gy(RBE)
Dmax(nominal)	53.83 Gy(RBE)	53.75 Gy(RBE)	45.33 Gy(RBE)	43.84 Gy(RBE)	46 Gy(RBE)

(b) Plan 2 results for organs at risk.

Organs at risk	brain	brainstem	chiasm	cochleaRIGHT	templobeLEFT
Relative deviation:	0.9%	1.0%	1.5%	-0.3%	0.6%
Dmax(expected)	69 Gy(RBE)	46 Gy(RBE)	45 Gy(RBE)	43 Gy(RBE)	69 Gy(RBE)
Dmax(nominal)	74.59 Gy(RBE)	56.39 Gy(RBE)	59.94 Gy(RBE)	11.18 Gy(RBE)	63.07 Gy(RBE)

(c) Plan 3 results for organs at risk.

Organs at risk	brainstem	spinalcord	chiasm	opticusLeft	opticusRight
Relative deviation:	-2.9%	4.7%	-0.1%	0.1%	-4.6%
Dmax(expected)	40 Gy(RBE)	35 Gy(RBE)	40 Gy(RBE)	22 Gy(RBE)	34 Gy(RBE)
Dmax(nominal)	27.25 Gy(RBE)	6.43 Gy(RBE)	40.47 Gy(RBE)	23.2 Gy(RBE)	1.75 Gy(RBE)

(d) Plan 4 for organs at risk.

Organs at risk	brainstem	chiasm	templobeLEFT	maculaLEFT	cocleaLEFT
Relative deviation:	1.0%	1.5%	0.7%	-1.5%	-0.1%
Dmax(expected)	46 Gy(RBE)	45 Gy(RBE)	54 Gy(RBE)	40 Gy(RBE)	30 Gy(RBE)
Dmax(nominal)	53.83 Gy(RBE)	39.63 Gy(RBE)	66.93 Gy(RBE)	7.14 Gy(RBE)	18.82 Gy(RBE)

(e) Plan 5 for organs at risk.

Organs at risk	brainstem	spinalcord	chiasm	opticusRIGHT	opticusLEFT
Relative deviation:	-1.6%	5.9%	-1.6%	-0.8%	-0.9%
Dmax(expected)	20 Gy(RBE)	20 Gy(RBE)	0.4 Gy(RBE)	0.4 Gy(RBE)	15 Gy(RBE)
Dmax(nominal)	4.25 Gy(RBE)	0.36 Gy(RBE)	0.63 Gy(RBE)	14.32 Gy(RBE)	13.19 Gy(RBE)



## 6.4 Conclusion

In the last Chapter 5 it was found that the MA-GATE and the RSL-FLUKA fluence agreed well for the main contribution, the primary Carbon ions. However, the fluence at low energies was considerably lower in GATE for all secondary particles and mainly for the proton and helium fluence components. The dose contribution of low energy particles in the spread-out Bragg peak (SOBP) is low, but the impact on RBE-weighted dose needs to be quantified as the RBE is non-linearly increasing with decreasing energy.

To conclude this chapter, a comparison was made on different target geometries, boxes and layers in water evaluating the RBE-weighted dose. In addition different clinical head and neck cases were investigated.

Single energy layer results revealed that the compared RBE-weighted dose generated by the two different beam models the MA-GATE and RSL-FLUKA models differ about less than 3% in the entrance region till the Bragg peak, whereas during the Bragg peak fall off region the deviation increases up to 5% and in the fragmentation tail differences of up to 15% were found.

For the boxes in water three regions were investigated. The deviations found in the plateau region were less than 0.5%, in the target region less than 1% and in the fragmentation tail less than 5%. The results from the fragmentation tails are tolerable because the fragmentation tail is a low dose region, with a small absolute but a high relative dose deviation.

In the five clinical cases we investigated the dose distributions showed differences of up to 3% restricted to local spots. The target volume dose deviations were found to be up to 2%, the maximum dose difference found in the organs at risk in the clinical plans was 5.9%, although this value and other higher deviations were found when the expected (prescribed) dose for organs at risk was far above the nominal (observed) dose. In total no relevant clinical differences were found neither in the target geometries in water nor in the clinical cases in the delivered dose produced by the beam models 'RSL-FLUKA' and 'MA-GATE'.

# 7

## Conclusion

In this project, where we focused on creating reliable fragment particle energy spectra to calculate the RBE-weighted dose, it was crucial to find a trustworthy MC physics builder.

For the process of finding the right candidate it was necessary to perform preliminary beam modeling for the beam model at the fixed Carbon beam line in irradiation room 2 at the therapeutic energy range (120 MeV/u to 402.8 MeV/u). For this purpose measurements have been carried out at MA, in the IR2 at four different energies with three different sized Bragg peak chambers ( $r=19.8$  mm, 40.8 mm and 73.5 mm) in a 3D computerized water scanner ('MP3-PL').

These measurements served as a foundation for the beam tuning which was done with the physics builder '*Shielding\_EMZ*' (QMD). Optical properties of the beam model were given by the therapy accelerator team and were set constant to reproduce a spot size of 2 mm in terms of FWHM at isocenter in vacuum during the process of beam modeling. In the tuning, we achieved a maximum deviation of less than 7% at the highest energy in the Bragg peak width and a difference in the Range80 at the lowest energy of less than 0.5% for the medium-sized Bragg peak chamber.

We could use the beam model, tuned at four different energies, for a comparison of the selected different physics builder *QGSP\_BIC\_HP* (BIC), *Shielding* (QMD) and *QGSP\_INCLXX* (INCL++). The results show that the nuclear model BIC had the best match overall with the measurements, INCL++ was the fastest and QMD was the slowest but also the most reliable which is desirable in the clinical environment. The agreement of the nuclear models BIC and QMD was similar but we found unphysical behavior in the IRPD using the BIC nuclear model so we decided for the builder '*Shielding\_EMZ*' (QMD).

The results of this physics builder sensitivity study are in accordance with previous studies. [Luehr12] [Boehlen10] Based on our results and the agreement with selected literature we used '*Shielding\_EMZ*' (QMD) as the physics builder of our choice for the simulations in Chapter 5. For the purpose of reliably scoring the fluence and therefore the energy spectra, an energy spectrum actor was developed in GATE/Geant4, based on the track length approach. Particle energy spectra were simulated at MA, using GATE version 8.2 in combination with Geant4 10.03.p03 and a dedicated beam model including a full geometrical description of the nozzle elements. 58 energies were simulated covering the full therapeutical energy range available for Carbon ion beams at MA. The spectra were simulated and later extracted in a 50 cm deep water phantom with a resolution of 1mm, storing the data in a binary file with a specific file structure. Different methods to compare the parti-

cle energy spectra generated from different MC codes, FLUKA and GATE/Geant4 were applied.

Fragment build up evaluation revealed, that the build up curves were similar and showed the predicted behavior, a steep build up of secondaries in the first centimeters in water. The amount of protons was predicted higher in the MA-GATE spectra with a maximum difference of up to 10%, while the secondary production of helium ions was predicted lower in the MA-GATE spectra by about 8%, close to the Bragg peak position in water.

The fluence averaged energies calculated for both spectra confirmed heavier particles show higher fluence-average energies than lighter particles before the Bragg peak, followed by a steep decrease of energy after the Bragg peak for the heavier particles. For the 320 MeV/u Carbon ion beam, proton and Helium ion energies, were predicted about 10-15% higher for the MA-GATE spectra, whereas Boron ion energies were 10-15 % higher for the RS-FLUKA spectra before the Bragg peak depth in water. Lithium and Beryllium are matching within 5% differences before the Bragg peak. After the Bragg peak the fluence averaged energies fit within total differences of 5% with local disagreements.

The comparison of the IRPD for the recomputation with the spectra and the IRPD scored with the dose actor has shown that our simulation methods were consistent within an absolute difference of 0.01 cm and a relative deviation of 0.3% for a 120 MeV/u Carbon ion beam and with an absolute difference of 0.02 cm and a relative deviation of 0.01% for a 400 MeV/u Carbon ion beam. Within a direct comparison of the MA-Gate and the RSL-FLUKA spectra, the fluence agreed well for the main contribution, the primary Carbon ions. However, the fluence at low energies below

1 MeV/u was considerably lower in GATE for all secondary particles and mainly for the proton and Helium fluence components.

The impact on the RBE weighted dose, by the differences in fluence, fluence averaged energies and range observed, is expected to be low but needs to be quantified and therefore an evaluation was carried out which can be found in Chapter 6. The dose contribution of low energy particles in the spread-out Bragg peak (SOBP) is low, but the impact on RBE-weighted dose needs to be quantified as the RBE is non-linearly increasing with decreasing energy.

A comparison was made on different target geometries, boxes and layers in water evaluating the RBE-weighted dose. In addition different clinical head and neck cases were investigated.

Single energy layer results revealed that the compared RBE-weighted dose generated by the two different beam models the MA-GATE and RSL-FLUKA models differ about less than 3% in the entrance region till the Bragg peak, whereas during the Bragg peak fall off region the deviation increases up to 5% and in the fragmentation tail differences of up to 15% were found.

For the boxes in water three regions were investigated. The deviations found in the plateau region were less than 0.5%, in the target region less than 1% and in the fragmentation tail less than 5%. The results from the fragmentation tails were tolerable because the fragmentation tail is a low dose region, with a small absolute but a high relative dose deviation.

In the five clinical cases we investigated the dose distributions showed differences of up to 3% restricted to local spots. The target volume dose deviations were found to be up to 2%, the maximum dose difference found in the organs at risk in the clinical plans was 5.9%, although this value and other higher deviations were found when the expected (prescribed) dose for organs at risk was far above the observed dose. In total no relevant clinical differences were found neither in the target geometries in water nor in the clinical cases in the delivered dose produced by the beam models 'RSL-FLUKA' and 'MA-GATE'. Consequently, Geant4/GATE may be used to independently validate Carbon ion beams for commissioning of a Carbon ion beam model and the generation of the particle energy spectra required for the LEM I model and further the RBE-weighted dose computation.

# Bibliography

- [Carlino17] Carlino, A. (2017). Implementation of advanced methodologies in the commissioning of a light ion beam therapy facility (Doctoral dissertation, PhD thesis, Department of Physics and Chemistry University of Palermo, Italy).
- [PIMMS] Proton-Ion Medical Machine Study (PIMMS), Badano, L ; Benedikt, Michael ; Bryant, P J ; Crescenti, M ; Holy, P ; Maier, A T ; Pullia, M ; Rossi, S ; Knaus, P - CERN-PS-2000-007-DR, 2000.
- [Pedroni95] Pedroni E. et al. The 200-mev proton therapy project at the Paul Scherrer Institute: Conceptual design and practical realization. *Med. Phys.*, 22:37–53, 1995.
- [Haberer93] Haberer T. et al. Magnetic scanning system for heavy ion therapy. *Nucl. Instrum. Methods Phys. Res. A*, 330:296–305, 1993.
- [Durante10] Durante, M., and Loefer, J. S. (2010). Charged particles in radiation oncology. *Nature reviews Clinical oncology*, 7(1), 37.
- [Giordanengo13] Giordanengo, S., Donetti, M., Garella, M.A., Marchetto, F., Alampi, G., Ansarinejad, A., Monaco, V., Mucchi, M., Pecka, I.A., Peroni, C. and Sacchi, R. (2013). Design and characterization of the beam monitor detectors of the Italian National Center of Oncological Hadron-therapy (CNAO). *Nuclear Instruments and Methods in Physics Research Section A: Accelerators, Spectrometers, Detectors and Associated Equipment*, 698, 202-207.
- [Giordanengo15] Giordanengo, S., Garella, M.A., Marchetto, F., Bourhaleb, F., Ciocca, M., Mirandola, A., Monaco, V., Hosseini, M.A., Peroni, C., Sacchi, R. and Cirio, R. (2015). The CNAO dose delivery system for modulated scanning ion beam radiotherapy. *Medical Physics*, 42(1), 263-275.
- [RSMAN] RaySearch Laboratories AB., RSL-D-RS-7.0-REF-EN-1.0-2017-12-08 RAYSTATION 7 REFERENCE MANUAL;2017, Stockholm, Sweden
- [InaniwaKanematsu15] Inaniwa, T. Kanematsu, N. A trichrome beam model for biological dose calculation in scanned Carbon-ion radiotherapy treatment planning. *Phys. Med. Biol.* 60,437-451(2015).
- [Sanchez-Parcerisa12] Sánchez Parcerisa, Daniel, Ph.D.-Thesis, Experimental and computational investigation of water-to-air stopping power ratio for ion chamber dosimetry in Carbon ion radiotherapy, Universität Heidelberg, 2012.
- [Elia19] A. Elia, Characterization of the GATE Monte Carlo platform for non-isocentric treatments and patient specific treatment plan verification at MedAustron, Vienna, Austria, 2019. PhD Thesis, Institut national des sciences appliquées de Lyon (Lyon) (établissement opérateur d'inscription) et de CREATIS - Centre de Recherche et d'Application en Traitement de l'Image pour la Santé, UMR5220 (Lyon, Rhône) (laboratoire).
- [Pompos16] Arnold Pompos, PhD, Marco Durante, PhD, and Hak Choy, MD, Heavy Ions in Cancer Therapy, 2016.
- [WHO18] World Cancer Key Facts 2018. World Health Organization. (2018). **Cancer Key Facts**.
- [GBD15] GBD 2015 Risk Factors Collaborators. Global, regional, and national comparative risk assessment of 79 behavioural, environmental and occupational, and metabolic risks or clusters of risks, 1990-2015: a systematic analysis for the Global Burden of Disease Study 2015. *Lancet*. 2016 Oct; 388 (10053):1659-1724.
- [IARC14] Lyon: International Agency for Research on Cancer; **World Cancer Report 2014**.
- [KSA18] Krebserkrankungen in Österreich, 2018, **Krebserkrankungsstatistik**.

- [WCRF18] Bray F, Ferlay J, Soerjomataram I, Siegel RL, Torre LA, Jemal A. Global Cancer Statistics 2018: GLOBOCAN estimates of incidence and mortality worldwide for 36 cancers in 185 countries. **Global cancer data**.
- [Wilson46] Radiological Use of Fast Protons, Robert R. Wilson, 1946.
- [PTCOG18] **PTCOG website**, Particle Therapy Co-Operative Group An organisation for those interested in proton, light ion and heavy charged particle radiotherapy
- [Kamada15] Kamada T, Tsujii H, Blakely EA, et al. Carbon ion radiotherapy in Japan. *Lancet Oncol.* 2015;16(2):e93-e100.
- [Schardt10] Schardt et al. ,Heavy-ion tumor therapy: Physical and radiobiological benefits, 2019
- [ICRU70] ICRU (1970). Task group dose as a function of let: Linear energy transfer: report 16. Technical report, International Commission on Radiation Units and Measurements, Washington.
- [ICRU76] International Commission of Radiation Units. International Commission on Radiation Units and Measurements: Stopping Power and ranges for protons and alpha particles. Report 24. 1976
- [ICRU78] Prescribing, recording, and reporting proton-beam therapy, International Commission on Radiation Units and Measurements. Bethesda, Bethesda, MD : ICRU, 2007. - 210 p., (ICRU Report ; 78), J. ICRU 7, 2 (2007).
- [ICRU85] ICRU report 85: fundamental quantities and units for ionizing radiation.
- [ICRU94] ICRU Reports J. W. Müller V. E. Lewis D. Smith J. G. V. Taylor G. Winkler *Journal of the International Commission on Radiation Units and Measurements*, Volume os27, Issue 1, 1 November 1994, Pages 76–79, <https://doi.org/10.1093/jicru/os27.1.76> Published: 27 April 2016
- [ICRU2000] ICRU 2000. ICRU Report 63: Nuclear Data for Neutron and Proton Radiotherapy and for Radiation Protection.
- [ICRU00] ICRU 2000. ICRU Report 63: Nuclear Data for Neutron and Proton Radiotherapy and for Radiation Protection.
- [ICRU05] ICRU 2005. ICRU Report 73: Stopping of ions heavier than helium.
- [Bethe30] H. Bethe, Zur Theorie des Durchgangs schneller Korpuskularstrahlen durch Materie, 1930
- [Bethe53] Bethe HA 1953. Molière's Theory of Multiple Scattering. *Physical Review*, 89, (6) 1256-1266.
- [Bloch33] F. Bloch, Zur Bremsung rasch bewegter Teilchen beim Durchgang durch Materie, 1933
- [Ziegler99] J. F. Ziegler, The Stopping of Energetic Light Ions in Elemental Matter, 1999
- [Gottschalk93] Gottschalk B et al. 1993. Multiple Coulomb scattering of 160 MeV protons. *Nuclear Instruments and Methods in Physics Research Section B: Beam Interactions with Materials and Atoms*, 74, (4) 467-490.
- [Gottschalk04] Gottschalk B 2004. Passive Beam Spreading in Proton Radiation Therapy
- [Gottschalk15] Gottschalk B, Cascio EW, Daartz J, Wagner MS., On the nuclear halo of a proton pencil beam stopping in water, *Phys Med Biol.* 2015 Jul 21;60(14):5627-54. doi: 10.1088/0031-9155/60/14/5627. Epub 2015 Jul 6.
- [Barkas63] Barkas HW 1963. *Nuclear Research Emulsions*. New York, Academic.
- [Janni82] Janni JF 1982. Energy loss, range, path length, time-of-flight, straggling, multiple scattering, and nuclear interaction probability: In two parts. Part 1. For 63 compounds Part 2. For elements Z=1-92. *Atomic Data and Nuclear Data Tables*, 27, (2-3) 147-339.
- [Sigmund09] Sigmund P, Schinner A, Paul H 2009. Errata and Addenda for ICRU Report 73, Stopping of Ions Heavier than Helium. *Journal of the ICRU*, 5, (1).
- [Rossi11] S Rossi. The status of cnao. *The European Physical Journal Plus*, 126(8):1–39, 2011.
- [Rossi52] Rossi B 1952. *High-energy particles* Englewood Cliffs, NJ, Prentice-Hall.
- [Bortfeld97] Bortfeld T 1997. An analytical approximation of the Bragg curve for therapeutic proton beams. *Med. Phys.*, 24, (12) 2024-2033.
- [Moliere47] Molière G 1947. Theorie der Streuung schneller geladener Teilchen. I. Einzelstreuung am abgeschirmten Coulomb-Feld. II. Mehrfach und Vielfachstreuung. *Z. Naturforsch. A*, 2, 133-145.
- [Moliere48] Molière G 1948. Theorie der Streuung schneller geladenen Teilchen II Mehrfach und Vielfachstreuung. *Z. Naturforsch. A*, 3, 78-97.



- [Fano54] Fano U 1954. Inelastic Collisions and the Molière Theory of Multiple Scattering. *Physical Review*, 93, (1) 117-120.
- [Lynch91] Lynch GR Dahl OI 1991. Approximations to multiple Coulomb scattering. *Nuclear Instruments and Methods in Physics Research Section B: Beam Interactions with Materials and Atoms*, 58, (1) 6-10.
- [Highland75] Highland VL 1975. Some practical remarks on multiple scattering. *Nuclear Instruments and Methods*, 129, (2) 497-499.
- [Serber47] R. Serber *Phys. Rev.* 72, 1114 – Published 1 December 1947, *Nuclear Reactions at High Energies*
- [Haettner06] Haettner E, IwasRe H, Schardt D. 2006 Experimental fragmentation studies with 12C therapy beams. *Radiat Prot Dosimetry.*;122(1-4):485-7.
- [Nitta06] Niita K et al. 2006. PHITS: A particle and heavy ion transport code system. *Radiation Measurements*, 41, (9-10) 1080-1090.
- [GunzertMarx08] Gunzert-Marx K et al. 2008. Secondary beam fragments produced by 200 MeV/u 12C ions in water and their dose contributions in Carbon ion radiotherapy. *New Journal of Physics*, 10, (7) 075003.
- [Boehlen10] Böhlen TT, Cerutti F, Dosanjh M, Ferrari A, Gudowska I, Mairani A, Quesada JM. 2010 Benchmarking nuclear models of FLUKA and GEANT4 for Carbon ion therapy. *Phys Med Biol.* Oct 7;55(19):5833-47.
- [Kraft00] G Kraft. *Tumor Therapy with Heavy Charged Particles. Progress in Particle and Nuclear Physics* , 45:473–544, 2000.
- [Paganetti16] Paganetti, H. (Ed.). (2016). *Proton therapy physics*. CRC press.
- [Scholz97] Scholz M et al. 1997. Computation of cell survival in heavy ion beams for therapy. The model and its approximation. *Radiat. Environ. Biophys.* , 36, (1) 59-66.
- [Elsaesser10] Elsaesser T et al. 2010. Quantification of the Relative Biological Effectiveness for Ion Beam Radiotherapy: Direct Experimental Comparison of Proton and Carbon Ion Beams and a Novel Approach for Treatment Planning. *International journal of radiation oncology, biology, physics*, 78, (4) 1177-1183.
- [Kanai97] Kanai T et al. 1997. Irradiation of mixed beam and design of spread-out Bragg peak for heavy-ion radiotherapy. *Radiat.Res.*, 147, (1) 78-85.
- [Colliaux09] Colliaux, A. (2009). *Implication de loxygène et des anti-oxydants dans le processus de radiolyse de leau induit par lirradiation aux ions de haute énergie : simulations numériques pour la radiobiologie*. PhD thesis, Université Claude Bernard Lyon 1.
- [KatzSharma74] Katz, R. and Sharma, S. C. (1974). Heavy particles in therapy: an application of track theory. *Physics in Medicine and Biology*, 19(4):413.
- [Waligorski86] Waligorski, M., Hamm, R., and Katz, R. (1986). The radial distribution of dose around the path of a heavy ion in liquid water. *International Journal of Radiation Applications and Instrumentation. Part D. Nuclear Tracks and Radiation Measurements*, 11(6):309 – 319.
- [ScholzKraft96] Scholz, M. and Kraft, G. (1996). Track structure and the calculation of biological effects of heavy charged particles. *Advances in Space Research*, 18(1-2):5 – 14.
- [ElsaesserScholz07] Elsaesser, T. and Scholz, M. (2007). Cluster effects within the local effect model. *Radiat Res.*, 167(3):319–329.
- [Kase08] Kase, Y., Kanai, T., Matsufuji, N., Furusawa, Y., Elsaesser, T., et al. (2008). Biophysical calculation of cell survival probabilities using amorphous track structure models for heavyion irradiation. *Physics in Medicine and Biology*, 53(1):37.
- [KieferStraaten86] Kiefer, J. and Straaten, H. (1986). A model of ion track structure based on classical collision dynamics (radiobiology application). *Physics in Medicine and Biology*, 31(11):1201.
- [ChatterjeeSchaefer76] Chatterjee, A. and Schaefer, H. J. (1976). Microdosimetric structure of heavy ion tracks in tissue. *Radiat Environ Biophys*, 13(3):215–227.
- [Sakama05] Sakama, M., Kanai, T., Kase, Y., Komori, M., Fukumura, A., et al. (2005). Responses of a diamond detector to high-let charged particles. *Phys Med Biol*, 50(10):2275–2289.
- [Beuve09] Beuve, M., Colliaux, A., Dabli, D., Dauvergne, D., Gervais, B., et al. (2009). Statistical effects of dose deposition in track-structure modelling of radiobiology efficiency. *Nuclear Instruments and Methods in Physics Research Section B: Beam Interactions with Materials*



- and Atoms, 267(6):983 – 988. Proceedings of the Seventh International Symposium on Swift Heavy Ions in Matter.
- [PapiezBattista94] L Papiez and J J Battista, Radiance and particle fluence, *Physics in Medicine Biology*, Volume 39, Number 6, 1994.
- [Uzawa09] Uzawa A et al. 2009. Comparison of Biological Effectiveness of Carbon-Ion Beams in Japan and Germany. *International journal of radiation oncology, biology, physics*, 73, (5) 1545-1551.
- [Chu06] Chu WT 2006. Overview of Light-Ion Beam Therapy. ICRU-IAEA Meeting, 16th Jun 2006.
- [Scholz03] Scholz M 2003. Effects of Ion Radiation on Cells and Tissues. *Radiation Effects on Polymers for Biological Use. Advances in Polymer Science*, 162, 95-155.
- [Chanrion16] Marie-Anne Chanrion. Study and development of physical models to evaluate biological effects of ion therapy: the study of local control of prostate cancer. *Medical Physics [physics.med-ph]*. Université Claude Bernard - Lyon I, 2014. English. NNT : 2014LYO10304. tel-01297837
- [IAEA2008] IAEA Annual Report for 2008.
- [Boehlen12] T. Böhlen, Ph. D. Thesis: Monte Carlo particle transport codes for ion beam therapy treatment planning, Stockholm University, Department of Physics, 2012.
- [CarabeFernandez07] Carabe-Fernandez, A. (2007). A theoretical investigation of the radiobiological rationale for high-LET radiotherapy. PhD thesis, University of London Imperial College of Science, Technology and Medicine Department of Medicine Division of Surgery, Oncology, Reproductive Biology and Anaesthetics (SORA).
- [KellererRossi72] Kellerer, A. M. and Rossi, H. H. (1972). The theory of dual radiation action. *Current Topics in Radiation Research Quarterly*, 8(2):85–158.
- [Yizheng17] A modified microdosimetric kinetic model for relative biological effectiveness calculation Yizheng Chen, Junli Li, Chunyan Li, Rui Qiu and Zhen Wu., Published 14 December 2017, Institute of Physics and Engineering in Medicine
- [Kanai99] Kanai, T., Endo, M., Minohara, S., Miyahara, N., Koyama-ito, H., et al. (1999). Biophysical characteristics of himac clinical irradiation system for heavy-ion radiation therapy. *Int J Radiat Oncol Biol Phys*, 44(1):201–210.
- [Inawa10] Inaniwa, T., Furukawa, T., Kase, Y., Matsufuji, N., Toshito, T., et al. (2010). Treatment planning for a scanned Carbon beam with a modified microdosimetric kinetic model. *Phys Med Biol*, 55(22):6721–6737.
- [Kundr05] Kundrát, P., Lokaj´icek, M., and Hromc´ikov´a, H. (2005). Probabilistic two-stage model of cell inactivation by ionizing particles. *Phys Med Biol*, 50(7):1433–1447.
- [KraemerScholz00] Krämer M and Scholz M 2000 Treatment planning for heavy-ion radiotherapy: calculation and optimization of biologically effective dose *Phys. Med. Biol.* 45 3319–30
- [Kraemer06] Krämer, M. and Scholz, M. (2006). Rapid calculation of biological effects in ion radiotherapy. *Phys Med Biol*, 51(8):1959–1970.
- [Elsaesser12] Elsaesser, T. (2012). *Ion Beam Therapy: Fundamentals, Technology, Clinical Applications*, chapter Modeling Heavy Ion Radiation Effects, pages 117–133. *Biological and Medical Physics, Biomedical Engineering*. Springer.
- [Friedrich13] Friedrich, T., Scholz, U., Elsaesser, T., Durante, M., and Scholz, M. (2013). Systematic analysis of RBE and related quantities using a database of cell survival experiments with ion beam irradiation. *J Radiat Res*, 54(3):494–514.
- [Gruen12] Grün, R., Friedrich, T., Elsaesser, T., Krämer, M., Zink, K., et al. (2012). Impact of enhancements in the local effect model (lem) on the predicted RBE-weighted target dose distribution in Carbon ion therapy. *Phys Med Biol*, 57(22):7261–7274.
- [Gillmann14] Gillmann, C., Jaekel, O., Schlamp, I., and Karger, C. P. (2014). Temporal lobe reactions after Carbon ion radiation therapy: comparison of relative biological effectiveness-weighted tolerance doses predicted by local effect models i and iv. *Int J Radiat Oncol Biol Phys*, 88(5):1136–1141.
- [Ferrari05] Ferrari, A., Sala, P. R., Fasso, A., and Ranft, J. (2005). FLUKA: A multiparticle transport code (Program version 2005) (No. INFN-TC-05-11).

- [Boehlen14] Böhlen, T.T., Cerutti, F., Chin, M.P.W., Fasso, A., Ferrari, A., Ortega, P.G., Mairani, A., Sala, P.R., Smirnov, G. and Vlachoudis, V. (2014). The FLUKA code: developments and challenges for high energy and medical applications. *Nuclear data sheets*, 120, 211-214.
- [Agostinelli03] Agostinelli, S., Allison, J., Amako, K.A., Apostolakis, J., Araujo, H., Arce, P., Asai, M., Axen, D., Banerjee, S., Barrand, G.2. and Behner, F. (2003). GEANT4|a simulation toolkit. *Nuclear instruments and methods in physics research section A: Accelerators, Spectrometers, Detectors and Associated Equipment*, 506(3), 250-303.
- [Allison06] Allison, J., Amako, K., Apostolakis, J.E.A., Araujo, H.A.A.H., Dubois, P.A., Asai, M.A.A.M., Barrand, G.A.B.G., Capra, R.A.C.R., Chauvie, S.A.C.S., Chytracek, R.A.C.R. and Cirrone, G.A.P. (2006). Geant4 developments and applications. *IEEE Transactions on nuclear science*, 53(1), 270-278.
- [Waters02] Waters, L. S. (2002). MCNPX user's manual. Los Alamos National Laboratory.
- [Pelowitz11] Pelowitz, D.B., Durkee, J.W., Elson, J.S., Fensin, M.L., Hendricks, J.S., James, M.R., Johns, R.C., Mc Kinney, F.W., Mashnik, S.G., Waters, L.S. and Wilcox, T.A. (2011). MCNPX 2.7 E extensions (No. LA-UR-11-01502; LA-UR-11-1502). Los Alamos National Laboratory (LANL).
- [Iwase02] Iwase, H., Niita, K., and Nakamura, T. (2002). Development of general-purpose particle and heavy ion transport Monte Carlo code. *Journal of Nuclear Science and Technology*, 39(11), 1142-1151.
- [Paganetti08] Paganetti, H., Jiang, H., Parodi, K., Slopsema, R., and Engelsman, M. (2008). Clinical implementation of full Monte Carlo dose calculation in proton beam therapy. *Physics in Medicine Biology*, 53(17), 4825.
- [Parodi12] Parodi K, Mairani A, Brons S, Hasch BG, Sommerer F, Naumann J, Jäkel O, Haberer T, Debus J. 2012 Monte Carlo simulations to support start-up and treatment planning of scanned proton and Carbon ion therapy at a synchrotron-based facility. *Phys Med Biol*. Jun 21;57(12):3759-84.
- [Grevillot11] Grevillot, L. (2011). Monte Carlo simulation of active scanning proton therapy system with Gate/Geant4: Towards a better patient dose quality assurance (Doctoral dissertation, INSA de Lyon).
- [Sarrut14] Sarrut, D., Bardies, M., Bousson, N., Freud, N., Jan, S., Letang, J.M., Loudos, G., Maigne, L., Marcatili, S., Mauxion, T. and Papadimitroulas, P. (2014). A review of the use and potential of the GATE Monte Carlo simulation code for radiation therapy and dosimetry applications. *Medical physics*, 41(6Part1).
- [Chetty07] Chetty, I. J., Curran, B., Cygler, J. E., DeMarco, J. J., Ezzell, G., Faddegon, B. A., Kawrakow, I., Keall, P. J., Liu, H., Ma, C.-M. C., Rogers, D. W. O., Seuntjens, J., Sheikh-Bagheri, D., Siebers, J. V., 2007. Report of the AAPM Task Group No. 105: Issues associated with clinical implementation of Monte Carlo-based photon and electron external beam treatment planning. *Med. Phys.* 34 (12), 4818–4853. 15, 48
- [Rogers06] Rogers, D. W. O., 2006. Fifty years of Monte Carlo simulations for medical physics. *Phys. Med. Biol.* 51 (13), R287. 15
- [Parodi07] Parodi, K., Paganetti, H., Shih, H. A., Michaud, S., Loeffler, J. S., DeLaney, T. F., Liebsch, N. J., Munzenrider, J. E., Fischman, A. J., Knopf, A., Bortfeld, T., 2007b. Patient study of in vivo verification of beam delivery and range, using positron emission tomography and computed tomography imaging after proton therapy. *Int. J. Radiat. Oncol.* 68 (3), 920–934. 15, 41, 51
- [FippelSoukop04] Fippel, M., Soukup, M., 2004. A Monte Carlo dose calculation algorithm for proton therapy. *Med. Phys.* 31 (8), 2263–2273. 16
- [Tourovsky05] Tourovsky, A., Lomax, A. J., Schneider, U., Pedroni, E., 2005. Monte Carlo dose calculations for spot scanned proton therapy. *Phys. Med. Biol.* 50 (5), 971. 16, 17
- [Hotta10] Hotta, K., Kohno, R., Takada, Y., Hara, Y., Tansho, R., Himukai, T., Kameoka, S., Matsuura, T., Nishio, T., Ogino, T., 2010. Improved dose-calculation accuracy in proton treatment planning using a simplified Monte Carlo method verified with three-dimensional measurements in an anthropomorphic phantom. *Phys. Med. Biol.* 55 (12), 3545. 16
- [Li05] Li, J. S., Shahine, B., Fourkal, E., Ma, C.-M., 2005. A particle track-repeating algorithm for proton beam dose calculation. *Phys. Med. Biol.* 50 (5), 1001. 16

- [Yepes10] Yepes, P. P., Mirkovic, D., Taddei, P. J., 2010. A GPU implementation of a track-repeating algorithm for proton radiotherapy dose calculations. *Phys. Med. Biol.* 55 (23), 7107–16
- [GEANT4] 2019. Geant4 Physics Reference Manual. Available at: **Geant4 Reference Manual**. 22
- [Ferrari02] Ferrari, A., Sala, P. R., 2002. Nuclear reactions in Monte Carlo codes. *Radiat. Prot. Dosim.* 99 (1-4), 29–38. 22, 23, 26, 27
- [Allison16] J. Allison et al. Recent developments in geant4. *Nuclear Instruments and Methods in Physics Research Section A: Accelerators, Spectrometers, Detectors and Associated Equipment*, 835:186–225, nov 2016. URL: <https://doi.org/10.1016/j.nima.2016.06.125>, doi:10.1016/j.nima.2016.06.125.
- [Apostolakis09] J. Apostolakis et al. . Geometry and physics of the geant4 toolkit for high and medium energy applications. *Radiation Physics and Chemistry*, 78(10):859–873, oct 2009. URL: <https://doi.org/10.1016/j.radphyschem.2009.04.026>, doi:10.1016/j.radphyschem.2009.04.026.
- [Messel70] H. Messel and D. Crawford. *Electron-Photon shower distribution*. Pergamon Press, 1970.
- [Nelson85] W.R. Nelson, H. Hirayama, and D.W.O. Rogers. EGS4 code system. SLAC, Dec 1985. SLAC-265, UC-32.
- [Butcher60] J.C. Butcher and H. Messel. *Nucl. Phys.*, 20(15):, 1960.
- [Koi08] Koi T 2008 New native QMD code in Geant4 IEEE Nuclear Science Symposium Conf. Record. 2008 (NSS '08)
- [Folger04] G. Folger, V. N. Ivanchenko, and J. P. Wellisch, The Binary Cascade Nucleon nuclear reactions, *Eur. Phys. J. A* 21,407-417 (2004).
- [Tripathi97] R. K. Tripathi, F. A. Cucinotta and J. W. Wilson, Universal Parameterization of Absorption Cross Sections, NASA Technical Paper TP-3621 (1997).
- [Tripathi99] R. K. Tripathi, F. A. Cucinotta and J. W. Wilson, Universal Parameterization of Absorption Cross Sections, NASA Technical Paper TP-209726 (1999)
- [Shen89] W.-q. Shen, B. Wang, J. Feng, W.-l. Zhan, Y.-t. Zhu and E.-p. Feng, Total reaction cross section for heavy-ion collisions and its relation to the neutron excess degree of freedom, *Nuclear Physics. A* 491 130-146 (1989)
- [Fang00] Fang D Q et al, 2000, Measurements of total reaction cross sections for some light nuclei at intermediate energies *Phys. Rev. C* 61 064311.
- [Zhang02] Zhang H Y et al 2002 Measurement of reaction cross section for proton-rich nuclei ( $A < 30$ ) at intermediate energies *Nucl. Phys. A* 707 303–24.
- [Takechi09] Takechi et al 2009 Reaction cross sections at intermediate energies and Fermi-motion effect *Phys. Rev.C* 79 061601.
- [Kox84] Kox S, Gamp A, Cherkaoui R, Cole A J, Longequque N, Menet J, Perrin C and Viano J B 1984 Direct Measurements of heavy-ion total reaction cross sections at 30 and 83 MeV/nucleon *Nucl. Phys. A* 420 162–72
- [Kox87] S. Kox, A. Gamp, C. Perrin, J. Arvieux, R. Bertholet, J. F. Bruandet, M. Buenerd, R. Cherkaoui, A. J. Cole, Y. El-Masri, N. Longequeue, J. Menet, F. Merchez, and J. B. Viano Trends of total reaction cross sections for heavy ion collisions in the intermediate energy range, *Phys. Rev. C* 35 1678-1691 (1987).
- [Sihver93] L. Sihver, C. H. Tsao, R. Silberberg, T. Kanai, and A. F. Barghouty, Total reaction and partial cross section calculations in proton-nucleus ( $Z_t 26$ ) and nucleus-nucleus reactions ( $Z_p$  and  $Z_t 26$ ), *Phys. Rev. C* 47 1225-1236 (1993).
- [Ivanchenko11] V. Ivanchenko et al. Recent improvements in geant4 electromagnetic physics models and interfaces. *Progress in NUCLEAR SCIENCE and TECHNOLOGY*, 2:898–903, oct 2011. URL: <http://www.aesj.or.jp/publication/pnst002/data/898-903.pdf>.
- [GateUserGuide] **GATE user guide**, 2019.
- [Carlino17] Carlino, A. (2017). Implementation of advanced methodologies in the commissioning of a light ion beam therapy facility (Doctoral dissertation, PhD thesis, Department of Physics and Chemistry University of Palermo, Italy).
- [Kanai83] Three-dimensional beam scanning for proton therapy, Kanai,KiyomitsuKawachi,Hideo,Matsuzawa,Tatsuaki, Division of Physics, National In-

- stitute of Radiological Sciences, 9-1, Anagawa 4-chome, Chiba-shi, Japan TetsuoInada  
Institute of Basic Medical Sciences, The University of Tsukuba, Sakura-mura, Ibaraki,  
300-31 Japan, 1983.
- [Pedroni95] Pedroni E. et al. The 200-mev proton therapy project at the Paul Scherrer Institute:  
Conceptual design and practical realization. *Med. Phys.*, 22:37–53, 1995.
- [Haberer93] Haberer T. et al. Magnetic scanning system for heavy ion therapy. *Nucl. In-  
strum.Methods Phys. Res. A*, 330:296–305, 1993.
- [Durante10] Durante, M., and Loefer, J. S. (2010). Charged particles in radiation oncology. *Nature  
reviews Clinical oncology*, 7(1), 37.
- [Giordanengo13] Giordanengo, S., Donetti, M., Garella, M.A., Marchetto, F., Alampi,  
G., Ansarinejad, A., Monaco, V., Mucchi, M., Pecka, I.A., Peroni, C. and Sacchi, R. (2013).  
Design and characterization of the beam monitor detectors of the Italian National Center of  
Oncological Hadron-therapy (CNAO). *Nuclear Instruments and Methods in Physics Research  
Section A: Accelerators, Spectrometers, Detectors and Associated Equipment*, 698, 202-207.
- [Giordanengo15] Giordanengo, S., Garella, M.A., Marchetto, F., Bourhaleb, F., Ciocca, M., Mi-  
randola, A., Monaco, V., Hosseini, M.A., Peroni, C., Sacchi, R. and Cirio, R. (2015). The  
CNAO dose delivery system for modulated scanning ion beam radiotherapy. *Medical Physics*,  
42(1), 263-275.
- [RSMAN] RaySearch Laboratories AB., RSL-D-RS-7.0-REF-EN-1.0-2017-12-08 RAYSTATION 7  
REFERENCE MANUAL;2017, Stockholm, Sweden
- [InaniwaKanematsu15] Inaniwa, T. Kanematsu, N. A trichrome beam model for biological dose  
calculation in scanned Carbon-ion radiotherapy treatment planning. *Phys. Med. Biol.* 60,437-  
451(2015).
- [Carlino18] A. Carlino<sup>1</sup>, T. Bohlen<sup>1;2</sup>, S. Vatnitsky<sup>1</sup>, L. Grevillot<sup>1</sup>, J. Osorio<sup>1</sup>, R. Dreindl<sup>1</sup>, H.  
Palmans<sup>1;3</sup>, M. Stock<sup>1</sup>, G. Kragl<sup>1</sup>, Commissioning of Pencil Beam and Monte Carlo dose  
engines for non-isocentric treatments in scanned proton beam therapy, journal 2018.
- [Grevillot18] Grevillot, L., Stock, M., Palmans, H., Osorio Moreno, J., Letellier, V., Dreindl,  
R., Elia, A., Fuchs, H., Carlino, A., and Vatnitsky, S. (2018). Implementation of dosimetry  
equipment and phantoms at the MedAustron light ion beam therapy facility. *Medical physics*,  
45(1):352369.
- [BeamLineModeling17] Grevillot, L. (2017). *BeamLineModeling Modeling the beam.*
- [Luehr12] Lühr A, Hansen DC, Teiwes R, Sobolevsky N, Jäkel O, Bassler N. 2012 The impact  
of modeling nuclear fragmentation on delivered dose and radiobiology in ion therapy. *Phys  
Med Biol.* 2012 Aug 21;57(16):5169-85. doi: 10.1088/0031-9155/57/16/5169. Epub Jul 27.  
PubMed PMID: 22842768.
- [Carlino17] Carlino, A. (2017). Implementation of advanced methodologies in the commissioning  
of a light ion beam therapy facility (Doctoral dissertation, PhD thesis, Department of Physics  
and Chemistry University of Palermo, Italy).
- [Boehlen10] Böhlen TT, Cerutti F, Dosanjh M, Ferrari A, Gudowska I, Mairani A, Quesada JM.  
2010 Benchmarking nuclear models of FLUKA and GEANT4 for Carbon ion therapy. *Phys  
Med Biol.* Oct 7;55(19):5833-47.
- [Bolst17] Validation of Geant4 fragmentation for Heavy Ion Therapy, Bolst, David; Cirrone,  
Giuseppe A; Cuttone, Giacomo; Folger, Gunter; Incerti, Sebastien; Ivanchenko, Vladimir  
N; Koi, Tatsumi; Mancusi, Davide; Pandola, Luciano; Romano, Francesco; Rosenfeld, Ana-  
toly B; Guatelli, Susanna, *Nuclear Instruments and Methods in Physics Research Section  
A: Accelerators, Spectrometers, Detectors and Associated Equipment*, ISSN: 0168-9002, Vol:  
869, Page: 68-75,2017.
- [Soukup05] Soukup, M., Fippel, M., and Alber, M. (2005). A pencil beam algorithm for inten-  
sity modulated proton therapy derived from Monte Carlo simulations. *Physics in Medicine  
Biology*, 50(21), 5089.
- [Grassberger14] Grassberger, Daartz, Dowdell, Ruggieri, Sharp, Paganetti ,Quantification of pro-  
ton dose calculation accuracy in the lung, *Int J Radiat Oncol Biol Phys.* 2014 Jun 1;89(2):424-  
30. doi: 10.1016/j.ijrobp.2014.02.023. Epub 2014 Apr 11.
- [Grassberger14] Grassberger, Daartz, Dowdell, Ruggieri, Sharp, Paganetti ,Quantification of pro-  
ton dose calculation accuracy in the lung, *Int J Radiat Oncol Biol Phys.* 2014 Jun 1;89(2):424-  
30. doi: 10.1016/j.ijrobp.2014.02.023. Epub 2014 Apr 11.



- [Frachiolla15] Fracchiolla F, Lorentini S, Widesott L, Schwarz M., Characterization and validation of a Monte Carlo code for independent dose calculation in proton therapy treatments with pencil beam scanning, *Phys Med Biol.* 2015 Nov 7;60(21):8601-19. doi: 10.1088/0031-9155/60/21/8601. Epub 2015 Oct 26.
- [Pedroni05] E Pedroni, S Scheib, T Böhringer, A Coray, M Grossmann, S Lin and A Lomax, Characterization and validation of a Monte Carlo code for independent dose calculation in proton therapy treatments with pencil beam scanning, Published 19 January 2005 • 2005 IOP Publishing Ltd.
- [Sawakuchi10] Gabriel O. Sawakuchi Dragan Mirkovic Luis A. Perles Narayan Sahoo X. Ron Zhu George Ciangaru Kazumichi Suzuki Michael T. Gillin Radhe Mohan Uwe Titt, An MCNPX Monte Carlo model of a discrete spot scanning proton beam therapy nozzle, First published: 26 August 2010 <https://doi.org/10.1118/1.3476458>.
- [Sawakuchi10a] Gabriel O. Sawakuchi Dragan Mirkovic Luis A. Perles Narayan Sahoo X. Ron Zhu George Ciangaru Kazumichi Suzuki Michael T. Gillin Radhe Mohan Uwe Titt, An MCNPX Monte Carlo model of a discrete spot scanning proton beam therapy nozzle, First published: 26 August 2010 <https://doi.org/10.1118/1.3476458>.
- [Sawakuchi10b] G Sawakuchi N Sahoo P Gasparian M Rodriguez L Archambault U Titt E Yukihara, TH-C-BRB-02: Determination of Average LET of Therapeutic Proton Beams Using A12O3:C Optically Stimulated Luminescence (OSL) Detectors, First published: 02 June 2010 <https://doi.org/10.1118/1.3469486>.
- [Elia19] A. Elia, Characterization of the GATE Monte Carlo platform for non-isocentric treatments and patient specific treatment plan verification at MedAustron, Vienna, Austria, 2019. PhD Thesis, Institut national des sciences appliquées de Lyon (Lyon) (établissement opérateur d'inscription) et de CREATIS - Centre de Recherche et d'Application en Traitement de l'Image pour la Santé, UMR5220 (Lyon, Rhône) (laboratoire).
- [Jan11] Jan, S., Benoit, D., Becheva, E., Carlier, T., Cassol, F., Descourt, P., Frisson, T., Grevillot, L., Guigues, L., Maigne, L. and Morel, C. (2011). GATE V6: a major enhancement of the GATE simulation platform enabling modelling of CT and radiotherapy. *Physics in Medicine Biology*, 56(4), 881.
- [Luehr12] Lühr A, Hansen DC, Teiwes R, Sobolevsky N, Jäkel O, Bassler N. 2012 The impact of modeling nuclear fragmentation on delivered dose and radiobiology in ion therapy. *Phys Med Biol.* 2012 Aug 21;57(16):5169-85. doi: 10.1088/0031-9155/57/16/5169. Epub Jul 27. PubMed PMID: 22842768.
- [Matsufuji03] Naruhiro Matsufuji, Akifumi Fukumura, Masataka Komori, Tatsuaki Kanai and Toshiyuki Kohno, 2003, Influence of fragmentation reaction of relativistic heavy charged particles on heavy-ion radiotherapy doi:10.1088/0031-9155/48/11/309 *Phys.Med.Biol.*,48,1605.
- [Kox84] Kox S, Gamp A, Cherkaoui R, Cole A J, Longequeue N, Menet J, Perrin C and Viano J B 1984 Direct Measurements of heavy-ion total reaction cross sections at 30 and 83 MeV/nucleon *Nucl. Phys. A* 420 162–72
- [Kox87] S. Kox, A. Gamp, C. Perrin, J. Arvieux, R. Bertholet, J. F. Bruandet, M. Buenerd, R. Cherkaoui, A. J. Cole, Y. El-Masri, N. Longequeue, J. Menet, F. Merchez, and J. B. Viano Trends of total reaction cross sections for heavy ion collisions in the intermediate energy range, *Phys. Rev. C* 35 1678-1691 (1987).
- [Sihver93] L. Sihver, C. H. Tsao, R. Silberberg, T. Kanai, and A. F. Barghouty, Total reaction and partial cross section calculations in proton-nucleus (Zt26) and nucleus-nucleus reactions (Zp and Zt26), *Phys. Rev. C* 47 1225-1236 (1993).
- [Fang2000] Fang D Q et al, 2000, Measurements of total reaction cross sections for some light nuclei at intermediate energies *Phys. Rev. C* 61 064311.
- [Zhang02] Zhang H Y et al 2002 Measurement of reaction cross section for proton-rich nuclei (A<30) at intermediate energies *Nucl. Phys. A* 707 303–24.
- [Takechi09] TakechiMet al 2009 Reaction cross sections at intermediate energies and Fermi-motion effect *Phys. Rev.C* 79 061601.
- [Boehlen10] Böhlen TT, Cerutti F, Dosanjh M, Ferrari A, Gudowska I, Mairani A, Quesada JM. 2010 Benchmarking nuclear models of FLUKA and GEANT4 for Carbon ion therapy. *Phys Med Biol.* Oct 7;55(19):5833-47.
- [GateUserGuide] **GATE user guide**, 2019.

- [Parodi12] Parodi K, Mairani A, Brons S, Hasch BG, Sommerer F, Naumann J, Jäkel O, Haberer T, Debus J. 2012 Monte Carlo simulations to support start-up and treatment planning of scanned proton and Carbon ion therapy at a synchrotron-based facility. *Phys Med Biol.* Jun 21;57(12):3759-84.
- [Ferrari2005] Ferrari, A., Sala, P. R., Fasso, A., and Ranft, J. (2005). FLUKA: A multiparticle transport code (Program version 2005) (No. INFN-TC-05-11).
- [Resch19] Resch, Andreas Elia, Alessio Fuchs, Hermann Carlino, Antonio Palmans, Hugo Stock, Markus Georg, Dietmar Grevillot, Loïc. (2019). Evaluation of electromagnetic and nuclear scattering models in GATE /Geant4 for proton therapy. *Medical Physics.* 46. 10.1002/mp.13472.
- [ICRU90] ICRU Report 90, Key Data For Ionizing-Radiation Dosimetry: Measurement Standards And Applications,1990.
- [RSMAN] RaySearch Laboratories AB., RSL-D-RS-7.0-REF-EN-1.0-2017-12-08 RAYSTATION 7 REFERENCE MANUAL;2017, Stockholm, Sweden
- [KohlenstoffTherapieKonzeptMA19] Dr. Piero Fossati, Treatment approach for Carbon ions at MedAustron, 2019.
- [Fuchs19] Hermann Fuchs (2019) Automatized beam modeling in Light Ion Beam Therapy, MedAustron, paper accepted.
- [Niessen19] Tom Niessen (2019), Energy spectra scoring in FLUKA, RaySearch Laboratories, presentation.



# List of Figures

1.1	Biological effectiveness of different treatment modalities. [Pompos16]	3
2.1	Depth dose profiles of photons, protons and Carbon ions. [Haettner06]	5
2.2	Stopping power of $^{12}\text{C}$ ions and protons in water as a fraction of specific energy. On the top axis, the corresponding range in water for Carbon ions. [Schardt10]	6
2.3	Illustration of $R0 = d80$ [Bortfeld97]. Different measurements with three proton beams of the same energy and with different initial energy spreads. Top: fluence, Middle: differential fluence in energy, Bottom: dose distribution [Gottschalk04]	9
2.4	Relation of range and energy for protons and Carbon ions in water. Data taken from [ICRU94] and [Sigmund09] fit to $R_0 = \alpha * T^\beta$ with $\beta=1.65$ for Carbon ions and with $\beta=1.74$ for protons.	10
2.5	Nuclear fragmentation as a two step process. [Haettner06]	12
2.6	The image on the top shows a depth dose distribution of a 200 MeV/u Carbon ion beam. The black line represents the total dose, blue dashed and solid lines are primary ions and its fragments. (calculated with MC code PHITS [Nitta06]) The image on the bottom shows the Bragg peak build up and fall off. [GunzertMarx08]	13
2.7	Track structure of a 24 MeV Carbon ion beam. On the top, the track is recorded along 15000 nm. On the bottom, the first $\mu\text{m}$ is depicted. (figure adapted from [Colliaux09]).	15
2.8	Definition of the RBE demonstrated via cell survival curves. [Kraft00]	18
2.9	RBE weighted dose (red) and physical dose (black) distributions are shown for protons (left). [IAEA2008]	18
3.1	Layout of the MedAustron Ion Therapy center.	31
3.2	Illustration of the active beam scanning techniques.[Durante10]	33
3.3	Layout of the MedAustron treatment head. Adapted from [Carlino17].	34
4.1	The lateral dose distribution of a 62.4 MeV proton beam with the source being at three different positions. Phantom surface, nozzle exit and nozzle entrance were investigated. The comparison between nozzle entrance and nozzle exit allows the prediction of the dose produced by secondaries due to the nuclear inelastic scattering which the primary ions experience along their path in the nozzle. The graph was adopted from [Elia19].	38

- 
- 4.2 Experimental setup for the integrated radial profiles as a function of depth. (a) full setup for measurements with the biggest BPC chamber (radius = 73.5 mm) and the 3D water tank and (b) direct shot of the PTW BP 150 the setup for measurements with the Bragg peak chamber Bragg Peak 150. Adapted from [Carlino17]. 39
- 4.3 Visualization of the beam diameter and the different Bragg peak chambers used. ( $r = 73.5, 40.8, 19.8$  mm) [Grevillot18] 40
- 4.4 Two of the three different Bragg peak chambers used ( $r = 40.8, 19.8$  mm). [Carlino17] 41
- 4.5 Integrated radial profiles as a function of depth normalized to the entrance. Measured for the different chambers at three different energies (400, 327 and 262 MeV/n). The different chamber sizes are displayed as the yellow line which corresponds to the medium-sized chamber ( $r = 40.8$  mm) and the black line which corresponds to the small chamber ( $r = 19.8$  mm). 43
- 4.6 Bragg peak width and R80 comparison for the medium-sized Bragg peak chamber with the integrated radial profile as a function of depth at an energy of 121 MeV/u. The dashed-dotted green line shows the relative deviation of the blue dotted measured IRPD and the solid red simulated IRPD. 44
- 4.7 Plateau and tail tuning for the medium-sized Bragg peak chamber with the integrated radial profile as a function of depth at an energy of 121 MeV/u. The dashed-dotted green line shows the relative deviation of the blue dotted measured IRPD and the solid red simulated IRPD. 45
- 4.8 Comparison of the integrated radial profiles as a function of depth using different nuclear models in GATE/Geant4. The solid red line shows the result from the nuclear model BIC, the solid green shows the result from the INCL++ model, the solid blue line shows the result of the QMD model and black dots is the measured dose. The dashed lines represent the relative deviation of the different respective nuclear models compared to the measured data. 47
- 4.9 Comparison of the integrated radial profiles as a function of depth using different nuclear models in GATE/Geant4. Plot lines have the same properties as in Figure 4.8. The plot shows the full range of the IRPD. 47
- 5.1 Workflow of the TPS beam modeling procedure. 50
- 5.2 Different total nuclear cross sections for Carbon ion beams interacting with  $H$ ,  $C$  and  $O$  shown as predicted by FLUKA version 2008.3 and Geant4 version 9.3 compared with experimental data from [Kox84, Kox87, Sihver93, Fang2000, Zhang02, Takechi09]. Graph adapted from [Boehlen10]. 50
- 5.3 Illustration of the two different approach to score fluence. [Niessen19] 52

- 5.4 Particle energy spectra simulated with FLUKA (per primary particle and MeV/u) for a 300 MeV/u Carbon ion beam at depth a)5 cm b)17 cm (Bragg peak adjacent) c)25 cm. [RSMAN] 54
- 5.5 Fragment build-up (total number of particles per primary particle) simulated with FLUKA for a 300 MeV/u Carbon ion beam. [RSMAN] 55
- 5.6 GATE/Geant4 simulation setup for the scoring of the energy particle spectra. Visible are two blue geometries, the smaller one is the frame around the MA nozzle which is described in detail by different boxes and cylinders, the bigger one is the 'World' in air which restricts the simulation volume. The green cubic is a water phantom with the dimension of  $50 \times 50 \times 50 \text{ cm}^3$ . The cyan circles within the water phantom are our scoring geometries with a radius of 5 cm and a thickness of 1 mm, where the energy spectra were scored. 56
- 5.7 Particle energy spectra (per primary particle) for a 400 MeV/u Carbon ion beam 26 cm deep in the water phantom. Solid lines are computed with FLUKA (RSL) and dashed lines are computed with GATE/Geant4 (MA). 58
- 5.8 Particle energy spectra for a 400 MeV/u Carbon ion beam at 4 cm depth in the water phantom. Line and axis properties as above. 58
- 5.9 Particle energy spectra (per primary particle) for a 120 MeV/u Carbon ion beam (3 cm range in water) at 2 cm depth in the water phantom close to the Bragg peak region. Solid lines are computed with FLUKA (RSL) and dashed lines are computed with GATE/Geant4 (MA). 59
- 5.10 Particle energy spectra for a 120 MeV/u Carbon ion beam at 0 cm depth in water at the entrance of the water phantom. Line and axis properties as above. 59
- 5.11 Fragment fluence build up over depth for a 120 MeV/u Carbon ion beam. The dashed lines show the fragment build up connected to the MA GATE simulated spectra, while the solid lines represent the RS FLUKA simulated fragment fluence build up. 60
- 5.12 Fragment fluence build-up over depth for a 320 MeV/u Carbon ion beam. The dashed lines show the fragment build up connected to the MA GATE simulated spectra, while the solid lines represent the RS FLUKA simulated fragment fluence build up. 60
- 5.13 The fluence averaged energies for the different specific ions. Solid lines show the RS FLUKA mean energies, while dashed lines represent the MA GATE simulated mean energies. Simulations were made for a 120 MeV/u Carbon ion beam. 61
- 5.14 The fluence averaged energies for the different specific ions. Solid lines show the RS FLUKA mean energies, while dashed lines represent the MA GATE simulated mean energies. Simulations were made for a 320 MeV/u Carbon ion beam. 61
- 5.15 Integrated radial profiles as a function of depth for a 120 MeV/u Carbon ion beam. The yellow solid line shows the recomputed IRPDs. The green line shows the IRPDs simulated with the dose actor. 62

- 
- 5.16 IRPDs for a 400 MeV/u Carbon ion beam. The solid yellow line shows the recomputed IRPD. The green line shows the IRPD simulated with the dose actor. 62
- 5.17 IRPDs for a 400 MeV/u Carbon ion beam. The yellow solid line shows the recomputed IRPD. The green line shows the IRPD simulated with the dose actor. 63
- 6.1 Workflow chart of the RBE-weighted dose evaluation in RS. 65
- 6.2 Dose distributions of the three box- like targets. From the left to the right the box6, box8 and box10. (For visualization purposes, the actual image was scaled, therefore boxes dont appear quadratic) 67
- 6.3 Overview of the clinical plans showing a slice of the patients anatomy and dose distribution in the transversal plane. 69
- 6.4 RBE-weighted integrated radial profile as a function of depth to visualize the different regions investigated. 70
- 6.5 RBE-weighted integrated radial profile as a function of depth for the mono-energetic layer at 1440 MeV. 71
- 6.6 This Figure shows the RBE-weighted SOBPs for the different beam models. The dose from the MA GATE/Geant4 Spectra beam model is visible as the darker (dotted) line and the dose calculated with the RS FLUKA spectra beam model is displayed as the thin solid line. Relative deviation in % is shown as the blue dashed-dotted line. 72
- 6.7 Three different beamsets applied to the patient in order to guarantee the dose distribution needed for PTV1 and PTV2. 73
- 6.8 Left: Overview of the clinical patient plan number five, planned with the RSL-FLUKA clinical beam model and recomputed with the MA-GATE beam model; Right: Dose differences due to the different beam models "MA-GATE" vs RSL-FLUKA in the RBE-weighted dose distribution. In the right picture small differences are visible in the nose region of up to 3%. 74
- 6.9 Displayed are dose volume histograms of the OARs extracted from patient plan 5. In purple the brainstem, in blue the chiasm, in black the spinal cord, in red the opticus left and in flesh tone the opticus right is viewed. Doses from the MA-GATE beam model are viewed in a solid line while the RS-FLUKA beam model doses are displayed in crosses. 75
- 6.10 Displayed are dose volume histograms of the target volumes extracted from patient plan 5. In purple the GTV is viewed, cyan is the PTV1 and red is the PTV2. Doses from the MA-GATE beam model are viewed in a solid line while the RS-FLUKA beam model doses are displayed in crosses. 75

# List of Tables

1.1	Comparison of X-rays, protons and light ions. [Pompos16]	4
2.1	Percentage contribution to stopping power number L for protons in aluminium, of the different correction terms for the Bethe Bloch (eq. 2.1). [Ziegler99]	7
2.2	<b>The Physics Reference Manual</b> [GEANT4] provides detailed explanations of the physics implemented in the Geant4 toolkit.	29
4.1	Beam tuning settings.	44
4.2	Beam tuning results summary.	45
4.3	Computation times on one core. $10^4$ particles were simulated comparing the different physics builder. INCL++ was the fastest and QMD the slowest. Absolute time differences and relative differences compared to QMD are displayed.	46
5.1	Binary file structure of the fragment spectra file.	56
6.1	Summary of the different results obtained in the target boxes in water.	72
6.2	Summary of the clinical plan results for organs at risk. Each table shows the following: The minimum dose DRBE,99%, the median dose DRBE,50% and DRBE,1% for different targets PTV1, PTV2, PTV3, CTV1, CTV2, GTV. The relative deviations of the RBE-weighted doses were computed as $(\text{'RS-FLUKA dose'}) - (\text{'MA-GATE dose'}) / (\text{'RS-FLUKA dose'}) \times 100$ . (eq. 6.1)	76
6.3	Summary of the clinical plan results for organs at risk. Each table shows the following: The expected (prescribed) maximum dose, the nominal (observed) dose and the relative deviation of different organs: brainstem, spinal cord, chiasm, opticus left, opticus right, cochlea left, cochlea right, templobe left and the macula left. The relative deviations of the RBE-weighted doses were computed as $(\text{'RS-FLUKA dose'}) - (\text{'MA-GATE dose'}) / (\text{'RS-FLUKA dose'}) \times 100$ . (eq. 6.1)	77